Implementation of nitrogen cycle in the CLASSIC land model

Ali Asaadi and Vivek. K. Arora

Canadian Centre for Climate Modelling and Analysis, Environment Canada, University of Victoria, Victoria, B.C., V8W 2Y2, Canada

Abstract

A terrestrial nitrogen (N) cycle model is coupled to carbon (C) cycle in the framework of the Canadian Land Surface Scheme Including biogeochemical Cycles (CLASSIC). CLASSIC currently models physical and biogeochemical processes and simulates fluxes of water, energy, and CO_2 at the land-atmosphere boundary. Similar to most models, gross primary productivity in CLASSIC increases in response to increasing atmospheric CO_2 concentration. In the current model version, a downregulation parameterization emulates the effect of nutrient constraints and scales down potential photosynthesis rates, using a globally constant scalar, as a function of increasing CO_2. In the new model when nitrogen (N) and carbon (C) cycles are coupled, cycling of N through the coupled soil-vegetation system facilitates the simulation of leaf N amount and maximum carboxylation capacity (V_{cmax}) prognostically. An increase in atmospheric CO_2 decreases leaf N amount, and therefore V_{cmax}, allowing the simulation of photosynthesis downregulation as a function of N supply. All primary N cycle processes, that represent the coupled soil-vegetation system, are modelled explicitly. These include biological N fixation, treatment of externally specified N deposition and fertilization application, uptake of N by plants, transfer of N to litter via litterfall, mineralization, immobilization, nitrification, denitrification, ammonia volatilization, leaching, and the gaseous fluxes of NO, N_2O, and N_2. The interactions between terrestrial C and N cycles are evaluated by perturbing the coupled soil-vegetation system in CLASSIC with one forcing at a time over the 1850-2017 historical period. These forcings include the increase in atmospheric CO_2, change in climate, increase in N deposition, and increasing crop area and fertilizer input, over the historical period. Increase in atmospheric CO_2 increases the C:N ratio of vegetation; climate warming over the historical period increases N mineralization and leads to a decrease in vegetation C:N ratio; N deposition also decreases vegetation C:N ratio; and fertilizer input increases leaching, NH_3 volatilization, and gaseous losses of N_2, N_2O, and NO. These model responses are consistent with conceptual understanding of the coupled C and N cycles. The simulated terrestrial carbon sink over the 1959-2017 period, from the simulation with all forcings, is 2.0 Pg C/yr and compares reasonably well with the quasi observation-based estimate from the 2019 Global Carbon Project (2.1 Pg C/yr). The contribution of increasing CO_2, climate change, and N deposition to carbon uptake by land over the historical period (1850-2017) is calculated to be 84%, 2%, and 14%, respectively.

1. Introduction

The uptake of carbon (C) by land and ocean in response to the increase in anthropogenic fossil fuel emissions of CO_2 has served to slow down the growth rate of atmospheric CO_2 since the start of the industrial revolution. At present, about 55% of total carbon emitted into the atmosphere is taken up by land and ocean (Le Quéré et al., 2018; Friedlingstein et al., 2019). It is of great policy, societal, and scientific relevance whether land and ocean will continue to provide this ecosystem service. Over land, as long as photosynthesis is not water limited, the uptake of carbon in response to increasing anthropogenic CO_2 emissions is driven by two primary factors, 1) the CO_2 fertilization of the terrestrial biosphere, and 2) the increase in temperature, both of which are associated with increasing $[CO_2]$. The CO_2 fertilization effect increases photosynthesis rates for about 80% of the world's vegetation that uses the C_3 photosynthetic pathway and is currently limited by $[CO_2]$ (Still et al., 2003; Zhu et al., 2016). The remaining 20% of vegetation uses the C_4 photosynthetic pathway that is much less sensitive to $[CO_2]$. Warming increases carbon uptake by vegetation in mid-high latitude regions where growth is currently limited by low temperatures (Zeng et al., 2011).

Even when atmospheric CO_2 is not limiting for photosynthesis, and near surface air temperature is optimal, vegetation cannot photosynthesize at its maximum possible rate if available water and nutrients (most importantly nitrogen (N) and phosphorus (P)) constrain photosynthesis (Vitousek and Howarth, 1991; Reich et al., 2006b). In the absence of water and nutrients, photosynthesis simply cannot occur. N is a major component of chlorophyll (the compound through which plants photosynthesize) and amino acids (that are the building blocks of proteins). The constraint imposed by available water and nutrients implies that the carbon

53   uptake by land over the historical period in response to increasing $[CO_2]$ is lower than what it

54   would have been if water and nutrients were not limiting. This lower than maximum theoretically

55   possible rate of increase of photosynthesis in response to increasing atmospheric CO_2 is referred

56   to as downregulation (Faria et al., 1996; Sanz-Sáez et al., 2010). Typically, however, the term

57   downregulation of photosynthesis is used only in the context of nutrients and not water.

58   Downregulation is defined as a decrease in photosynthetic capacity of plants grown at elevated

59   CO_2 in comparison to plants grown at baseline CO_2 (McGuire et al., 1995). However, despite the

60   decrease in photosynthetic capacity, the photosynthesis rate for plants grown at elevated CO_2 is

61   still higher than the rate for plants grown and measured at baseline CO_2 because of higher

62   background CO_2.

63   Earth system models (ESMs) that explicitly represent coupling of the global carbon cycle

64   and physical climate system processes are the only tools available at present that, in a physically

65   consistent way, are able to project how land and ocean carbon cycles will respond to future

66   changes in $[CO_2]$. Such models are routinely compared to one another under the auspices of the

67   Coupled Model Intercomparison Project (CMIP) every 6-7 years. The most recent and sixth phase

68   of CMIP (CMIP6) is currently underway (Eyring et al., 2016). Interactions between carbon cycle

69   and climate in ESMs have been compared under the umbrella of the Coupled Climate-Carbon

70   Cycle Model Intercomparison Project (C[4]MIP) (Jones et al., 2016) which is an approved MIP of

71   the CMIP. Comparison of land and ocean carbon uptake in C[4]MIP studies (Friedlingstein et al.,

72   2006; Arora et al., 2013, 2020) indicate that the inter-model uncertainty in future land carbon

73   uptake across ESMs is more than three times than the uncertainty for the ocean carbon uptake.

74   The reason for widely varying estimates of future land carbon uptake is that our understanding

75 of biological processes that determine land carbon uptake is much less advanced than the

76 physical processes which primarily determine carbon uptake over the ocean. In the current

77 generation of terrestrial ecosystem models, other than leaf level photosynthesis for which a

78 theoretical framework exists, almost all of the other biological processes are represented on the

79 basis of empirical observations and parameterized in one way or another. In addition, not all

80 models include nutrient cycles. In the absence of an explicit representation of nutrient

81 constraints on photosynthesis, land models in ESMs parameterize downregulation of

82 photosynthesis in other ways that reduce the rate of increase of photosynthesis to values below

83 its theoretically maximum possible rate, as [CO_2] increases (e.g., Arora et al., 2009). Comparison

84 of models across 5th and 6th phase of CMIP shows that the fraction of models with land N cycle is

85 increasing (Arora et al., 2013, 2020).

86   The nutrient constraints on photosynthesis are well recognized (Vitousek and Howarth,

87 1991; Arneth et al., 2010). Terrestrial carbon cycle models neglect of nutrient limitation on

88 photosynthesis has been questioned from an ecological perspective (Reich et al., 2006a) and it

89 has been argued that without nutrient constraints these models will overestimate future land

90 carbon uptake (Hungate et al., 2003). Since in the real world photosynthesis downregulation does

91 indeed occur due to nutrient constraints, it may be argued that more confidence can be placed

92 in future projections of models that explicitly model the interactions between the terrestrial C

93 and N cycles rather than parameterize it in some other way.

94   Here, we present the implementation of N cycle in the Canadian Land Surface Scheme

95 Including biogeochemical Cycles (CLASSIC) model, which serves as the land component in the

96 family of Canadian Earth System Models (Arora et al., 2009, 2011; Swart et al., 2019). Section 2

97   briefly describes existing physical and carbon cycle components and processes of the CLASSIC

98   model. The conceptual basis of the new N cycle model and its parameterizations are described

99   in Section 3. Section 4 outlines the methodology and data sets that we have used to perform

100   various simulations over the 1850-2017 historical period to assess the realism of the coupled C

101   and N cycles in CLASSIC in response to various forcings. Results from these simulations over the

102   historical period are presented in Section 5 and finally discussion and conclusions are presented

103   in Section 6.

104   **2. The CLASSIC land model**

105   **2.1 The physical and carbon biogeochemical processes**

106   The CLASSIC model is the successor to, and based on, the coupled Canadian Land Surface

107   Scheme (CLASS; Verseghy, 1991; Verseghy et al., 1993) and Canadian Terrestrial Ecosystem

108   Model (CTEM; Arora and Boer, 2005; Melton and Arora, 2016). CLASS and CTEM model physical

109   and biogeochemical processes in CLASSIC, respectively. Both CLASS and CTEM have a long history

110   of development as described in Melton et al. (2019) who also provide an overview of the CLASSIC

111   land model and describe its new technical developments that launched CLASSIC as a community

112   model. CLASSIC simulates land-atmosphere fluxes of water, energy, momentum, CO_2, and CH_4.

113   The CLASSIC model can be run at a point scale, e.g. using meteorological and geophysical data

114   from a FluxNet site, or over a spatial domain, that may be global or regional, using gridded data.

115   We briefly summarize the primary physical and carbon biogeochemical processes of CLASSIC here

116   that are relevant in the context of implementation of the N cycle in the model.

117   **2.1.1 Physical processes**

118   The physical processes of CLASSIC which simulate fluxes of water, energy and momentum,

119   are calculated over vegetated, snow, and bare fractions on a model grid at a sub-daily time step

120   of 30 minutes. The vegetation is described in terms of four plant functional types (PFTs):

121   needleleaf trees, broadleaf trees, crops, and grasses. In the current study, the fractional coverage

122   of these four PFTs are specified over the historical period. The structural attributes of vegetation

123   are described by leaf area index (LAI), vegetation height, canopy mass, and rooting distribution

124   through the soil layers and these are all simulated dynamically by the biogeochemical module of

125   CLASSIC. In the model version used here, 20 ground layers starting with 10 layers of 0.1 m

126   thickness are used. The thickness of layers gradually increases to 30 m for a total ground depth

127   of over 61 m. The depth to bedrock varies geographically and is specified based on a soil depth

128   data set. Liquid and frozen soil moisture contents, and soil temperature, are determined

129   prognostically for permeable soil layers. CLASSIC also prognostically models the temperature,

130   mass, albedo, and density of a single layer snow pack (when the climate permits snow to exist).

131   Interception and throughfall of rain and snow by the canopy, and the subsequent unloading of

132   snow, are also modelled. The energy and water balance over the land surface, and the transfer

133   of heat and moisture through soil, affect the temperature and soil moisture content of soil layers

134   all of which consequently affect the carbon and nitrogen cycle processes.

135

136   **2.1.2 Biogeochemical processes**

137   The biogeochemical processes in CLASSIC are based on CTEM, and described in detail in

138   the appendix of Melton and Arora (2016). The biogeochemical component of CLASSIC simulates

139   the land-atmosphere exchange of CO_2 and while doing so simulates vegetation as a dynamic

140   component. The biogeochemical module of CLASSIC uses information about net radiation, and

141   liquid and frozen soil moisture contents of all the soil layers along with air temperature to

142   simulate photosynthesis and prognostically calculates amount of carbon in the model's three live

143   (leaves, stem, and root) and two dead (litter and soil) carbon pools for each PFT. The C amount

144   in these pools is represented as amount of C per unit land area (kg C/m^2).The litter and soil carbon

145   pools are not tracked for each soil layer. Litter is assumed to be near surface and an exponential

146   distribution for soil carbon is assumed with values decreasing with soil depth. Photosynthesis in

147   CLASSIC is modelled at the same sub-daily time as the physical processes. The remainder of the

148   biogeochemical processes are modelled at a daily time step. These include: 1) autotrophic and

149   heterotrophic respirations from all the live and dead carbon pools, respectively, 2) allocation of

150   photosynthate from leaves to stem and roots, 3) leaf phenology, 4) turnover of live vegetation

151   components that generates litter, 5) mortality, 6) land use change (LUC), 7) fire (Arora and

152   Melton, 2018), and 8) competition between PFTs for space (not switched on in this study).

153   Figure A1 in the appendix shows the existing structure of CLASSIC's carbon pools along

154   with the addition of non-structural carbohydrate pools for each of the model's live vegetation

155   components. The non-structural pools are not yet represented in the current operational version

156   of CLASSIC (Melton et al., 2019). The addition of non-structural carbohydrate pools is explained

157   in Asaadi et al. (2018) and helps improve leaf phenology for cold deciduous tree PFTs. The N cycle

158   model presented here is built on the research version of CLASSIC that consists of non-structural

159   and structural carbon pools for the leaves (L), stem (S), and root (R) components and the two

160   dead carbon pools in litter or detritus (D) and soil or humus (H) (Figure A1). We briefly describe

161 these carbon pools and fluxes between them, since N cycle pools and fluxes are closely tied to

162 carbon pools and fluxes. The gross primary productivity (GPP) flux enters the leaves from the

163 atmosphere. This non-structural photosynthate is allocated between leaves, stem, and roots. The

164 non-structural carbon then moves into the structural carbohydrates pool. Once this conversion

165 occurs structural carbon cannot be converted back to non-structural labile carbon. The model

166 attempts to maintain a minimum fraction of non-structural to total carbon in each component of

167 about 0.05 (Asaadi et al., 2018). Non-structural carbon is moved from stem and root components

168 to leaves, at the time of leaf onset for deciduous PFTs, and this is termed reallocation. The

169 movement of non-structural carbon is indicated by red arrows. Maintenance and growth

170 respiration (indicated by subscript m and g in Figure A1), which together constitute autotrophic

171 respiration, occur from the non-structural components of the three live vegetation components.

172 Litterfall from the structural and non-structural components of the vegetation components

173 contributes to the litter pool. Leaf litterfall is generated due to normal turnover of leaves as well

174 as cold and drought stresses, and reduction in day length. Stem and root litter is generated due

175 to their turnover based on their specified life spans. Heterotrophic respiration occurs from the

176 litter and soil carbon pools depending on soil moisture and temperature, and humified litter is

177 moved from litter to the soil carbon pool.

178   All these terrestrial ecosystem processes and the amount of carbon in the live and dead

179 carbon pools are modelled explicitly for nine PFTs that map directly onto the four base PFTs used

180 in the physics module of CLASSIC. Needleleaf trees are divided into their deciduous and

181 evergreen phenotypes, broadleaf trees are divided into cold deciduous, drought deciduous, and

182 evergreen phenotypes, and crops and grasses are divided based on their photosynthetic

183 pathways into C_3 and C_4 versions. The sub-division of PFTs is required for modelling

184 biogeochemical processes. For instance, simulating leaf phenology requires the distinction

185 between evergreen and deciduous phenotypes of needleleaf and broadleaf trees. However, once

186 LAI is known, a physical process (such as the interception of rain and snow by canopy leaves) does

187 not need to know the underlying evergreen or deciduous nature of leaves.

188   The prognostically determined biomasses in leaves, stem, and roots are used to calculate

189 structural vegetation attributes that are required by the physics module. Leaf biomass is used to

190 calculate LAI using PFT-dependent specific leaf area. Stem biomass is used to calculate vegetation

191 height for tree and crop PFTs, and LAI is used to calculate vegetation height for grasses. Finally,

192 root biomass is used to calculate rooting depth and distribution which determines the fraction of

193 roots in each soil layer. Only total root biomass is tracked; fine and coarse root biomasses are not

194 separately tracked. Fraction of fine roots is calculated as a function of total root biomass, as

195 shown later.

196   The approach for calculating photosynthesis in CLASSIC is based on the standard Farquhar

197 et al. (1980) model for C_3 photosynthetic pathway, and Collatz et al. (1992) for the C_4

198 photosynthetic pathway and presented in detail in Arora (2003). The model calculates gross

199 photosynthesis rate that is co-limited by the photosynthetic enzyme Rubisco, by the amount of

200 available light, and by the capacity to transport photosynthetic products for C_3 plants or the CO_2-

201 limited capacity for C_4 plants. In the real world, the maximum Rubsico limited rate (V_{cmax}) depends

202 on the leaf N amount since photosynthetic capacity and leaf N are strongly correlated (Evans,

203 1989; Field and Mooney, 1986; Garnier et al., 1999). Leaf N amount may be represented per unit

204 leaf area (gN/m^2), per unit ground area (gN/m^2), or per unit leaf mass (gN/gC or %) (Loomis, 1997;

205   Li et al., 2018). In the current operational version of CLASSIC, the N cycle is not represented and

206   the PFT-dependent values of V_{cmax} are therefore specified based on Kattge et al. (2009) who

207   compile V_{cmax} values using observation-based data from more than 700 measurements. Along

208   with available light, and the capacity to transport photosynthetic products, the GPP in the model

209   is determined by specified PFT-dependent values of V_{cmax}.

210   In the current CLASSIC version a parameterization of photosynthesis downregulation is included

211   which, in the absence of the N cycle, implicitly attempts to simulate the effects of nutrient

212   constraints. This parameterization, based on approaches which express GPP as a logarithmic

213   function of [CO_2] (Cao et al., 2001; Alexandrov and Oikawa, 2002), is explained in detail in Arora

214   et al. (2009) and briefly summarized here. To parameterize photosynthesis downregulation with

215   increasing [CO_2] the unconstrained or potential GPP (for each time step and each PFT in a grid

216   cell) is multiplied by the global scalar $\xi(c)$

217    $$G = \xi(c)\ G_p \qquad\qquad\qquad (1)$$

218    $$\xi(c) = \frac{1+\gamma_d \ln(c/c_0)}{1+\gamma_p \ln(c/c_0)} \qquad\qquad\qquad (2)$$

219   where c is [CO_2] at time t and its initial value is c_0, the parameter γ_p indicates the "potential" rate

220   of increase of GPP with [CO_2] (indicated by the subscript p), the parameter γ_d represents the

221   downregulated rate of increase of GPP with [CO_2] (indicated by the subscript d). When $\gamma_d < \gamma_p$

222   the modelled gross primary productivity (G) increases in response to [CO_2] at a rate determined

223   by the value of γ_d. In the absence of the N cycle, the term $\xi(c)$ thus emulates down-regulation

224   of photosynthesis as CO_2 increases. For example, values of γ_d=0.35 and γ_p=0.90, yield a value of

225    $\xi(c)$ = 0.87 (indicating a 13% downregulation) for c=390 ppm (corresponding to year 2010) and

226   c_0=285 ppm.

227   Note that while the original model version does not include N cycle, it is capable of

228   simulating realistic geographical distribution of GPP that partly comes from the specification of

229   observation-based V_{cmax} values (which implicitly takes into account C and N interactions in a non-

230   dynamic way) but more so the fact that the geographical distribution of GPP (and therefore net

231   primary productivity, NPP), to the first order, depends on climate. The specified V_{cmax} values for

232   the 9 PFTs in CLASSIC vary by about 2 times, from about 35 to 75 μ-mol CO_2 m^{-2} s^{-1}. The simulated

233   GPP in the model, however, varies from zero in the Sahara desert to about 3000 gC m^{-2} $year^{-1}$ in

234   the Amazonian rainforest indicating the overarching control of climate in determining the

235   geographical distribution of GPP. This is further illustrated by the Miami NPP model, for instance,

236   which is able to simulate the geographical distribution of NPP using only mean annual

237   temperature and precipitation (Leith, 1975) since both the C and N cycles are governed primarily

238   by climate. The current version of CLASSIC is also able to reasonably simulate the terrestrial C

239   sink over the second half of the 20th century and early 21st century. CLASSIC (with its former

240   CLASS-CTEM name) has regularly contributed to the annual Trends in Net Land–Atmosphere

241   Carbon Exchange (TRENDY) model intercomparison since 2016 which contributes results to the

242   Global Carbon Project's annual assessments – the most recent one being Friedlingstein et al.

243   (2019). What is then the purpose of coupling C and N cycles?

244

245   **3. Implementation of the N cycle in CLASSIC**

246   The primary objective of implementation of the N cycle is to model V_{cmax} as a function of

247   leaf N amount so as to make the use of multiplier $\xi(c)$ obsolete in the model, and allow to project

248   future carbon uptake that is constrained by available N. Modelling of leaf N as a prognostic

249   variable, however, requires modelling the full N cycle over land. N enters the soil in the inorganic

250   mineral form through biological fixation of N, fertilizer application, and atmospheric N deposition

251   in the form of ammonium and nitrate. N cycling through plants implies uptake of inorganic

252   mineral N by plants, its return to soil through litter generation in the organic form, and its

253   conversion back to mineral form during decomposition of organic matter in litter and soil. Finally,

254   N leaves the coupled soil-vegetation system through leaching in runoff and through various

255   gaseous forms to the atmosphere. This section describes how these processes are implemented

256   and parameterized in the CLASSIC modelling framework. While the first order interactions

257   between C and N cycles are described well by the current climate, their temporal dynamics over

258   time require to explicitly model these processes.

259   Globally, terrestrial N cycle processes are even less constrained than the C cycle

260   processes. As a result, the model structure and parameterizations are based on conceptual

261   understanding and mostly empirical observations of N cycle related biological processes. We

262   attempt to achieve balance between a parsimonious and simple model structure and the ability

263   to represent the primary feedbacks and interactions between different model components.

264   **3.1 Model structure, and N pools and fluxes**

265   N is associated with each of the model's three live vegetation components and the two

266   dead carbon pools (shown in Figure A1). In addition, separate mineral pools of ammonium (NH_4^+)

267   and nitrate (NO_3^-) are considered. Similar to the C pools, the N pools are represented as N amount

268   per unit land area. Given the lower absolute amounts of N than C, over land, we represent them

269   in units of grams as opposed to kilograms (gN/m^2). Figure 1 shows the C and N pools together in

270   one graphic along with the fluxes of N and C between various pools. The structural and non-

271   structural N pools in root are written as $N_{R,S}$ and $N_{R,NS}$, respectively, and similarly for stem ($N_{S,S}$

272   and $N_{S,NS}$) and leaves ($N_{L,S}$ and $N_{L,NS}$), and together the structural and non-structural pools make

273   up the total N pools in leaf ($N_L = N_{L,S} + N_{L,NS}$), root ($N_R = N_{R,S} + N_{R,NS}$), and stem ($N_S = N_{S,S} +$

274    $N_{S,NS}$) components. The fluxes between the pools in Figure 1 characterize the prognostic nature

275   of the pools as defined by the rate change equations summarized in section A1 in the appendix.

276   The model structure allows the C:N ratio of the live leaves ($C:N_L = C_L/N_L$), stem ($C:N_S =$

277   C_S/N_S), and root ($C:N_R = C_R/N_R$) components, and the dead litter (or debris) pool ($C:N_D =$

278   C_D/N_D) to evolve prognostically. The C:N ratio of soil organic matter ($C:N_H = C_H/N_H$), however,

279   is assumed to be constant at 13 following Wania et al. (2012) (see also references therein). The

280   implications of this assumption are discussed later.

281   The individual terms of the rate change equations of the 10 prognostic N pools (equations

282   A1 through A8, and equations A10 and A11 in the appendix), corresponding to Figure 1, are

283   specified or parameterized as explained in the following sections. These parameterizations are

284   divided into three groups and related to 1) N inputs, 2) N cycling in vegetation and soil, and 3) N

285   cycling in mineral pools and N outputs.

286

287   **3.2 N inputs**

3.2.1 Biological N fixation

288

289   Biological N fixation (BNF, B_{NH4}) is caused by both free living bacteria in the soil and by

290 bacteria symbiotically living within nodules of host plants' roots. Here, the bacteria convert free

291 nitrogen from the atmosphere to ammonium, which is used by the host plants. Like any other

292 microbial activity, BNF is limited both by drier soil moisture conditions and cold temperatures.

293 Cleveland et al. (1999) attempt to capture this by parameterizing BNF as a function of actual

294 evapotranspiration (AET). AET is a function primarily of soil moisture (through precipitation and

295 soil water balance) and available energy. In places where vegetation exists, AET is also affected

296 by vegetation characteristics including LAI and rooting depth. Here, we parameterize BNF (B_{NH4},

297 gN m^{-2} day^{-1}) as a function of modelled soil moisture and temperature to depth of 0.5 m

298 (following the use of similar depth by Xu-Ri and Prentice (2008)) which yields a very similar

299 geographical distribution of BNF as the Cleveland et al. (1999) approach as seen later in Section

300 4.

301
$$B_{NH4} = \left(\sum_c \alpha_c f_c + \sum_n \alpha_n f_n \right) f(T_{0.5}) f(\theta_{0.5})$$
$$f(T_{0.5}) = 2^{(T_{0.5}-25)/10}$$
$$f(\theta_{0.5}) = \min\left(0, \max\left(1, \frac{\theta_{0.5}-\theta_w}{\theta_{fc}-\theta_w} \right) \right)$$
(3)

302 where α_c and α_n (gN m^{-2} day^{-1}) are BNF coefficients for crop (c) and non-crop or natural (n) PFTs,

303 which are area weighted using the fractional coverages f_c and f_n of crop and non-crop PFTs that

304 are present in a grid cell, $f(T)$ is the dependence on soil temperature based on a Q$_{10}$ formulation

305 and $f(\theta)$ is the dependence on soil moisture which varies between 0 and 1. θ_{fc} and θ_w are the

306 soil moisture at field capacity and wilting points, respectively. $T_{0.5}$ (°C) and $\theta_{0.5}$ (m^3 m^{-3}) in

307 equation (3) are averaged over the 0.5 m soil depth over which BNF is assumed to occur. We do

308   not make the distinction between symbiotic and non-symbiotic BNF since this requires explicit

309   knowledge of geographical distribution of N fixing PFTs which are not represented separately in

310   our base set of nine PFTs. A higher value of α_c is used compared to α_n to account for the use of

311   N fixing plants over agricultural areas. Biological nitrogen fixation has been an essential

312   component of many farming systems for considerable periods, with evidence for the agricultural

313   use of legumes dating back more than 4,000 years (O'Hara, 1998). A higher α_c than α_n is also

314   consistent with Fowler et al. (2013) who report BNF of 58 and 60 Tg N yr^{-1} for natural and

315   agricultural ecosystems for present day. Since the area of natural ecosystems is about five times

316   the current cropland area, this implies BNF rate per unit land area is higher for crop ecosystems

317   than for natural ecosystems. Values of α_c than α_n and other model parameters are summarized

318   in Table A1.

319   Similar to Cleveland et al. (1999), our approach does not lead to a significant change in

320   BNF with increasing atmospheric CO_2, other than through changes in soil moisture and

321   temperature. At least two meta-analyses, however, suggest that an increase in atmospheric CO_2

322   does lead to an increase in BNF through increased symbiotic activity associated with an increase

323   in both nodule mass and number (McGuire et al., 1995; Liang et al., 2016). Models have

324   attempted to capture this by simulating BNF as a function of NPP (Thornton et al., 2007; Wania

325   et al., 2012). The caveat with this approach and the implications of our BNF approach are

326   discussed in Section 6.

327   **3.2.2 Atmospheric N deposition**

328   Atmospheric N deposition is externally specified. The model reads in spatially- and

329   temporally-varying annual deposition rates from a file. Deposition is assumed to occur at the

330   same rate throughout the year so the same daily rate (gN m^{-2} day^{-1}) is used for all days of a given

331   year. If separate information for ammonium (NH_4^+) and nitrate (NO_3^-) deposition rates is available

332   then it is used otherwise deposition is assumed to be split equally between NH_4^+ and NO_3^-

333   (indicated as P_{NH4} and P_{NO3} in equations A1 and A2).

334   **3.2.3 Fertilizer application**

335   Geographically and temporally varying annual fertilizer application rates (F_{NH4}) are also

336   specified externally and read in. Fertilizer application occurs over the C$_3$ and C$_4$ crop fractions of

337   grid cells. Agricultural management practices are difficult to model since they vary widely

338   between countries and even from farmer to farmer. For simplicity, we assume fertilizer is applied

339   at the same daily fertilizer application rate (gN m^{-2} day^{-1}) throughout the year in the tropics

340   (between 30°S and 30°N), given the possibility of multiple crop rotations in a given year. Between

341   the 30° and 90° latitudes in both northern and southern hemispheres, we assume that fertilizer

342   application starts on the spring equinox and ends on the fall equinox. The annual fertilizer

343   application rate is thus distributed over around 180 days. This provides somewhat more realism,

344   than using the same treatment as in tropical regions, since extra-tropical agricultural areas

345   typically do not experience multiple crop rotations in a given year. The prior knowledge of start

346   and end days for fertilizer application makes it easier to figure out how much fertilizer is to be

347   applied each day and helps ensure that the annual amount read from the externally specified file

348   is consistently applied.

349

3.3 N cycling in plants and soil

351   Plant roots take up mineral N from soil and then allocate it to leaves and stem to maintain

352   an optimal C:N ratio of each component. Both active and passive plant uptakes of N (from both

353   the NH_4^+ and NO_3^- pools; explained in Sections 3.3.2 and 3.3.3) are explicitly modelled. The active

354   N uptake is modelled as a function of fine root biomass, and passive N uptake depends on the

355   transpiration flux. The modelled plant N uptake also depends on its N demand. Higher N demand

356   leads to higher mineral N uptake from soil as explained below. Litterfall from vegetation

357   contributes to the litter pool and decomposition of litter transfers humified litter to the soil

358   organic matter pool. Decomposition of litter and soil organic matter returns mineralized N back

359   to the NH_4^+ pool, closing the soil-vegetation N cycle loop.

3.3.1 Plant N demand

361   Plant N demand is calculated based on the fraction of NPP allocated to leaves, stem, and

362   root components and their specified minimum PFT-dependent C:N ratios, similar to other models

363   (Xu-Ri and Prentice, 2008; Jiang et al., 2019). The assumption is that plants always want to

364   achieve their desired minimum C:N ratios if enough N is available.

$$\Delta_{WP} = \Delta_L + \Delta_R + \Delta_S$$

365

$$\Delta_i = \frac{\max\left(0, NPP \cdot a_{i,C}\right)}{C:N_{i,\min}}, \quad i = L, S, R \tag{4}$$

366   where the whole plant N demand (Δ_{WP}) is the sum of N demand for the leaves (Δ_L), stem (Δ_S),

367   and root (Δ_R) components, $a_{i,C}$, $i = L, S, R$ is the fraction of NPP (i.e., carbon as indicated by

368   letter C in the subscript, gC m^{-2} day^{-1}) allocated to leaf, stem, and root components, and

369 $C{:}N_{i,\text{min}}, i = L, S, R$ are their specified minimum C:N ratios (see Table A1 for these and all other

370 model parameters). A caveat with this approach when applied at the daily time step, for

371 biogeochemical processes in our model, is that during periods of time when NPP is negative due

372 to adverse climatic conditions (e.g., during winter or drought seasons), the calculated demand is

373 negative. If positive NPP implies there is demand for N, negative NPP cannot be taken to imply

374 that N must be lost from vegetation. As a result, from a plant's perspective, N demand is assumed

375 to be zero during periods of negative NPP. N demand is also set to zero when all leaves have been

376 shed (i.e., when GPP is zero). At the global scale, this leads to about 15% higher annual N demand

377 than would be the case if negative NPP values were taken into consideration.

378

379 **3.3.2 Passive N uptake**

380 N demand is weighed against passive and active N uptake. Passive N uptake depends on

381 the concentration of mineral N in the soil and the water taken up by the plants through their

382 roots as a result of transpiration. We assume that plants have no control over N that comes into

383 the plant through this pathway. This is consistent with existing empirical evidence that too much

384 N in soil will cause N toxicity (Goyal and Huffaker, 1984), although we do not model N toxicity in

385 our framework. If the N demand for the current time step cannot be met by passive N uptake

386 then a plant compensates for the deficit (i.e., the remaining demand) through active N uptake.

387 The NH_4^+ concentration in the soil moisture within the rooting zone, referred to as $[NH_4]$

388 (gN gH_2O^{-1}), is calculated as

389
$$[NH_4] = \frac{N_{\text{NH4}}}{\sum_{i=1}^{i \le r_I} 10^6 \, \theta_i \, z_i} \tag{5}$$

390   where N_{NH4} is ammonium pool size (gN m^{-2}), θ_i is the volumetric soil moisture content for soil

391   layer i (m^3 m^{-3}), z_i is the thickness of soil layer i (m), r_l is the soil layer in which the 99% rooting

392   depth lies as dynamically simulated by the biogeochemical module of CLASSIC following Arora

393   and Boer (2003). The 10^6 term converts units of the denominator term to gH$_2$O m^{-2}. NO$_3^-$

394   concentration ([NO$_3$], gN gH$_2$O^{-1}) in the rooting zone is found in a similar fashion. The

395   transpiration flux q_t (kg H$_2$O m^{-2} s^{-1}) (calculated in the physics module of CLASSIC) is multiplied

396   by [NH$_4$] and [NO$_3$] (gN gH$_2$O^{-1}) to obtain passive uptake of NH$_4^+$ and NO$_3^-$ (gN m^{-2} day^{-1}) as

$$
\begin{aligned}
U_{p,NH4} &= 86400 \times 10^3 \, \beta \, q_t [\text{NH}_4] \\
U_{p,NO3} &= 86400 \times 10^3 \, \beta \, q_t [\text{NO}_3]
\end{aligned}
\tag{6}
$$

398   where the multiplier 86400×10^3 converts q_t to units of gH$_2$O m^{-2} day^{-1}, and β (see Table A1) is

399   the dimensionless mineral N distribution coefficient with a value less than 1 that accounts for the

400   fact that NH$_4^+$ and NO$_3^-$ available in the soil are not well mixed in the soil moisture solution, and

401   not completely accessible to roots, to be taken up by plants.

3.3.3 Active N uptake

403   The active plant N uptake is parameterized as a function of fine root biomass and the size

404   of NH$_4^+$ and NO$_3^-$ pools in a manner similar to Gerber et al. (2010) and Wania et al. (2012). The

405   distribution of fine roots across the soil layers is ignored. CLASSIC does not explicitly model fine

406   root biomass. We therefore calculate the fraction of fine root biomass using an empirical

407   relationship that is very similar to the relationship developed by Kurz et al. (1996) (their equation

408   5) but also works below total root biomass of 0.33 Kg C m^{-2} (the Kurz et al. (1996) relationship

409   yields a fraction of fine root more than 1.0 below this threshold). The fraction of fine root biomass

410   (f_r) is given by

411
$$f_r = 1 - \frac{C_R}{C_R + 0.6}$$
(7)

412   where C_R is the root biomass (KgC m^{-2}) simulated by the biogeochemical module of CLASSIC.

413   Equation (7) yields fine root fraction approaching 1.0 as C_R approaches 0, so at very low root

414   biomass values all roots are considered fine roots. For grasses the fraction of fine root biomass is

415   set to 1. The maximum or potential active N uptake for NH$_4^+$ and NO$_3^-$ is given by

416
$$U_{a,pot,\mathrm{NH4}} = \frac{\varepsilon\, f_r\, C_R\, \mathrm{N_{NH4}}}{k_{p,\frac{1}{2}}\, r_d + \mathrm{N_{NH4}} + \mathrm{N_{NO3}}}$$
$$U_{a,pot,\mathrm{NO3}} = \frac{\varepsilon\, f_r\, C_R\, \mathrm{N_{NO3}}}{k_{p,\frac{1}{2}}\, r_d + \mathrm{N_{NH4}} + \mathrm{N_{NO3}}}$$
(8)

417   where ε (see Table A1) is the efficiency of fine roots to take up N per unit fine root mass per day

418   (gN gC^{-1} day^{-1}), $k_{p,\frac{1}{2}}$ (see Table A1) is the half saturation constant (gN m^{-3}), r_d is the 99% rooting

419   depth (m), and $\mathrm{N_{NH4}}$ and $\mathrm{N_{NO3}}$ are the ammonium and nitrate pool sizes (gN m^{-2}) as mentioned

420   earlier. Depending on the geographical location and the time of the year, if passive uptake alone

421   can satisfy plant N demand the actual active N uptake of NH$_4^+$ ($U_{a,actual,\mathrm{NH4}}$) and NO$_3^-$

422   ($U_{a,actual,\mathrm{NO3}}$) is set to zero. Conversely, during other times both passive and potential active N

423   uptakes may not be able to satisfy the demand and in this case actual active N uptake is equal to

424   its potential rate. At times other than these, the actual active uptake is lower than its potential

425   value. This adjustment of actual active uptake is illustrated in equation (9).

$$\text{if } \left(\Delta_{WP} \leq U_{p,NH4} + U_{p,NO3}\right)$$
$$U_{a,actual,\text{NH4}} = 0$$
$$U_{a,actual,\text{NO3}} = 0$$

$$\text{if } \left(\Delta_{WP} > U_{p,NH4} + U_{p,NO3}\right) \wedge \left(\Delta_{WP} < U_{p,NH4} + U_{p,NO3} + U_{a,pot,\text{NH4}} + U_{a,pot,\text{NH4}}\right)$$

426
$$U_{a,actual,\text{NH4}} = \left(\Delta_{WP} - U_{p,NH4} - U_{p,NO3}\right)\frac{U_{a,pot,\text{NH4}}}{U_{a,pot,\text{NH4}} + U_{a,pot,\text{NH4}}}$$ (9)
$$U_{a,actual,\text{NO3}} = \left(\Delta_{WP} - U_{p,NH4} - U_{p,NO3}\right)\frac{U_{a,pot,\text{NO3}}}{U_{a,pot,\text{NH4}} + U_{a,pot,\text{NH4}}}$$

$$\text{if } \left(\Delta_{WP} \geq U_{p,NH4} + U_{p,NO3} + U_{a,pot,\text{NH4}} + U_{a,pot,\text{NO3}}\right)$$
$$U_{a,actual,\text{NH4}} = U_{a,pot,\text{NH4}}$$
$$U_{a,actual,\text{NO3}} = U_{a,pot,\text{NO3}}$$

427   Finally, the total N uptake (U), uptake of NH_4^+ (U_{NH4}) and NO_3^- (U_{NO3}), are calculated as

428
$$U = U_{p,NH4} + U_{p,NO3} + U_{a,actual,\text{NH4}} + U_{a,actual,\text{NO3}}$$
$$U_{NH4} = U_{p,NH4} + U_{a,actual,\text{NH4}}$$ (10)
$$U_{NO3} = U_{p,NO3} + U_{a,actual,\text{NO3}}$$

429

430   **3.3.4 Litterfall**

431   Nitrogen litterfall from the vegetation components is directly tied to the carbon litterfall

432   calculated by the phenology module of CLASSIC through their current C:N ratios.

433
$$LF_i = \frac{(1-r_L)\, LF_{i,C}}{C:N_i}, i = L, S, R$$ (11)

434   where $LF_{i,C}$ is the carbon litterfall rate (gC day^{-1}) for component i, calculated by the phenology

435   module of CLASSIC, and division by its current C:N ratio yields the nitrogen litterfall rate, r_L (see

436   Table A1) is the leaf resorption coefficient that simulates the resorption of N from leaves of

437   deciduous tree PFTs before they are shed and $r_i = 0, i = R, S$. Litter from each vegetation

438   component is proportioned between structural and non-structural components according to

439   their pool sizes.

440   **3.3.5 Allocation and reallocation**

441   Plant N uptake by roots is allocated to leaves and stem to satisfy their N demand. When

442   plant N demand is greater than zero, total N uptake (U) is divided between leaves, stem, and root

443   components in proportion to their demands such that the allocation fractions for N ($a_i, i =$

444   L, S, R) are calculated as

445

$$
\begin{aligned}
a_i &= \frac{\Delta_i}{\Delta_{WP}} \;, i = L, S, R \\
A_{R2L} &= a_L \, (U_{NH4} + U_{NO3}) \\
A_{R2S} &= a_S \, (U_{NH4} + U_{NO3})
\end{aligned}
\tag{12}
$$

446   where A_{R2L} and A_{R2S} are the amounts of N allocated from root to leaves and stem components,

447   respectively, as shown in equations (A5) and (A7). During periods of negative NPP due to adverse

448   climatic conditions (e.g., during winter or drought seasons) the plant N demand is set to zero but

449   passive N uptake, associated with transpiration, may still be occurring if the leaves are still on.

450   Even though there is no N demand, passive N uptake still needs to be partitioned among the

451   vegetation components. During periods of negative NPP allocation fractions for N are, therefore,

452   calculated in proportion to the minimum PFT-dependent C:N ratios of the leaves, stem, and root

453   components as follows.

454

$$
a_i = \frac{1/C{:}N_{i,\min}}{1/C{:}N_{L,\min} + 1/C{:}N_{S,\min} + 1/C{:}N_{R,\min}} \;, i = L, S, R
\tag{13}
$$

455   For grasses, which do not have a stem component, equations (12) and (13) are modified

456   accordingly by removing the terms associated with the stem component.

457   Three additional rules override these general allocation rule specifically for deciduous

458   tree PFTs (or deciduous PFTs in general). First, no N allocation is made to leaves once leaf fall is

459   initiated for deciduous tree PFTs and plant N uptake is proportioned between stem and root

460   components based on their demands in a manner similar to equation (12). Second, for deciduous

461   tree PFTs, a fraction of leaf N is resorbed from leaves back into stem and root as follows

$$
\begin{aligned}
R_{L2R} &= r_L\, LF_L\, \frac{N_{R,NS}}{N_{R,NS}+N_{S,NS}} \\
R_{L2S} &= r_L\, LF_L\, \frac{N_{S,NS}}{N_{R,NS}+N_{S,NS}}
\end{aligned}
$$

462   (14)

463

464   where r_L is the leaf resorption coefficient, as mentioned earlier, and LF_L is the leaf litter fall rate.

465   Third, and similar to resorption, at the time of leaf onset for deciduous tree PFTs, N is reallocated

466   to leaves (in conjunction with reallocated carbon as explained in Asaadi et al. (2018)) from stem

467   and root components.

$$
\begin{aligned}
R_{R2L} &= \frac{R_{R2L,C}}{C:N_L}\; \frac{N_{R,NS}}{N_{R,NS}+N_{S,NS}} \\
R_{S2L} &= \frac{R_{S2L,C}}{C:N_L}\; \frac{N_{S,NS}}{N_{R,NS}+N_{S,NS}}
\end{aligned}
$$

468   (15)

469   where $R_{R2L,C}$ and $R_{S2L,C}$ represent reallocation of carbon from non-structural stem and root

470   components to leaves and division by $C:N_L$ converts the flux into N units. This reallocated N, at

471   the time of leaf onset, is proportioned between non-structural pools of stem and root according

472   to their sizes.

473   **3.3.6 N mineralization, immobilization, and humification**

474   Decomposition of litter ($R_{h,D}$) and soil organic matter ($R_{h,H}$) releases C to the atmosphere

475   and this flux is calculated by the heterotrophic respiration module of CLASSIC. The litter and soil

476   carbon decomposition rates used here are the same as in the standard model version (Melton

477   and Arora, 2016; their Table A3). The amount of N mineralized is calculated straightforwardly by

478   division with the current C:N ratios of the respective pools and contributes to the NH_4^+ pool.

479
$$M_{D,NH4} = \frac{R_{h,D}}{C:N_D}$$
$$M_{H,NH4} = \frac{R_{h,H}}{C:N_H}$$
(16)

480   An implication of mineralization contributing to the NH_4^+ pool, in addition to BNF and fertilizer

481   inputs that also contribute solely to the NH_4^+ pool, is that the simulated NH_4^+ pool is typically

482   larger than the NO_3^- pool. The exception is the dry and arid regions where the lack of

483   denitrification, as discussed below in Section 3.4.2., leads to a build-up of the NO_3^- pool.

484   Immobilization of mineral N from the NH_4^+ and NO_3^- pools into the soil organic matter

485   pool is meant to keep the soil organic matter C:N ratio ($C:N_H$) at its specified value of 13 for all

486   PFTs in a manner similar to Wania et al. (2012) and Zhang et al. (2018). A value of 13 is within the

487   range of observation-based estimates which vary from about 8 to 25 (Zinke et al., 1998; Tipping

488   et al., 2016). Although $C:N_H$ varies geographically, the driving factors behind this variability

489   remain unclear. It is even more difficult to establish if increasing atmospheric CO_2 is changing

490    $C:N_H$ given the large heterogeneity in soil organic C and N densities, and the difficulty in

491   measuring small trends for such large global pools. We therefore make the assumption that the

492    $C:N_H$ does not change with time. An implication of this assumption is that as GPP increases with

493   increasing atmospheric CO_2 rises, and plant litter becomes enriched in C with increasing C:N ratio

494   of litter, more and more N is locked up in the soil organic matter pool because its C:N ratio is

495   fixed. As a result, mineral N pools of NH_4^+ and NO_3^- decrease in size and plant N amount

496   subsequently follows. This is consistent with studies of plants grown in elevated CO_2

497   environment. For example, Cotrufo et al. (1998) summarize results from 75 studies and find an

498   average 14% reduction in N concentration (gN/gC) for above-ground tissues. Wang et al. (2019)

499   find increased C concentration by 0.8–1.2% and a reduction in N concentration by 7.4–10.7% for

500   rice and winter wheat crop rotation system under elevated CO_2. Another implication of using

501   specified fixed $C:N_H$ is that it does not matter if plant N uptake or immobilization is given

502   preferred access to the mineral N pool since in the long term, by design, N will accumulate in the

503   soil organic matter in response to atmospheric CO_2 increase.

504   Immobilization from both the NH_4^+ and NO_3^- pools (gN m^{-2} day^{-1}) is calculated in

505   proportion to their pool sizes, employing the fixed $C:N_H$ ratio as

$$O_{NH4} = \max\left(0, \left(\frac{C_H}{C:N_H} - N_H\right)\frac{N_{NH4}}{N_{NH4}+N_{NO3}}\right) k_O$$

$$O_{NO3} = \max\left(0, \left(\frac{C_H}{C:N_H} - N_H\right)\frac{N_{NO3}}{N_{NH4}+N_{NO3}}\right) k_O$$

506   (17)

507   where k_O is rate constant with a value of 1.0 day^{-1}. Finally, the carbon flux of humified litter from

508   the litter to the soil organic matter pool ($H_{C,D2H}$) is also associated with a corresponding N flux

509   that depends on the C:N ratio of the litter pool.

$$H_{N,D2H} = \frac{H_{C,D2H}}{C:N_D}$$

510   (18)

511   **3.4 N cycling in mineral pools and N outputs**

512   This section presents the parameterizations of nitrification (which results in transfer of N

513   from the NH_4^+ to the NO_3^- pool) and the associated gaseous fluxes of N_2O and NO (referred to as

514   nitrifier denitrification), gaseous fluxes of N_2O, NO, and N_2 associated with denitrification,

515   volatilization of NH_4^+ into NH_3, and leaching of NO_3^- in runoff.

516   **3.4.1 Nitrification**

517   Nitrification, the oxidative process converting ammonium to nitrate, is driven by microbial

518   activity and as such constrained both by high and low soil moisture (Porporato et al., 2003). At

519   high soil moisture content there is little aeration of soil and this constrains aerobic microbial

520   activity, while at low soil moisture content microbial activity is constrained by moisture

521   limitation. In CLASSIC, the heterotrophic respiration from soil carbon is constrained similarly but

522   rather than using soil moisture the parameterization is based on soil matric potential (Arora,

523   2003; Melton et al., 2015). Here, we use the exact same parameterization. In addition to soil

524   moisture, nitrification (gN m^{-2} day^{-1}) is modelled as a function of soil temperature and the size

525   of the NH_4^+ pool as follows

526    $$I_{NO3} = \eta \, f_I(T_{0.5}) f_I(\psi) \, N_{NH4}$$ (19)

527   where η is the nitrification coefficient (day^{-1}, see Table A1), $f_I(\psi)$ is the dimensionless soil

528   moisture scalar that varies between 0 and 1 and depends on soil matric potential (ψ), $f_I(T_{0.5})$ is

529   the dimensionless soil temperature scalar that depends on soil temperature ($T_{0.5}$) averaged over

530   the top 0.5 m soil depth over which nitrification is assumed to occur (following Xu-Ri and Prentice,

531   2008), and N_{NH4} is the ammonium pool size (gN m^{-2}), as mentioned earlier. Both $f_I(T_{0.5})$ and

532    $f_I(\psi)$ are parameterized following Arora (2003) and Melton et al. (2015). $f_I(T_{0.5})$ is a Q_{10} type

533   function with a temperature dependent Q_{10}

534
$$f_I(T_{0.5}) = Q_{10,I}^{(T_{0.5}-20)/10}, Q_{10,I} = 1.44 + 0.56\left(\tanh\left(0.075(46 - T_{0.5})\right)\right) \tag{20}$$

535   The reference temperature for nitrification is set to 20 °C following Lin et al. (2000). $f_I(\psi)$ is

536   parameterized as a step function of soil matric potential (ψ) as

537
$$f_I(\psi) = \begin{cases} 0.5 & \text{if } \psi \leq \psi_{sat} \\ 1 - 0.5\frac{\log(0.4)-\log(\psi)}{\log(0.4)-\log(\psi_{sat})} & \text{if } 0.4 > \psi \geq \psi_{sat} \\ 1 & \text{if } 0.6 \geq \psi \geq 0.4 \\ 1 - 0.8\frac{\log(\psi)-\log(0.6)}{\log(100)-\log(0.6)} & \text{if } 100 > \psi > 0.6 \\ 0.2 & \text{if } \psi > 100 \end{cases} \tag{21}$$

538   where the soil matric potential (ψ) is found, following Clapp and Hornberger (1978), as a function

539   of soil moisture (θ)

540
$$\psi(\theta) = \psi_{sat}\left(\frac{\theta}{\theta_{sat}}\right)^{-B}. \tag{22}$$

541   Saturated matric potential (ψ_{sat}), soil moisture at saturation (i.e., porosity) (θ_{sat}), and the

542   parameter B are calculated as functions of percent sand and clay in soil following Clapp and

543   Hornberger (1978) as shown in Melton et al. (2015). The soil moisture scalar $f_I(\psi)$ is calculated

544   individually for each soil layer and then averaged over the soil depth of 0.5 m over which

545   nitrification is assumed to occur.

546   Gaseous fluxes of NO (I_{NO}) and N$_2$O (I_{N2O}) associated with nitrification, and generated

547   through nitrifier denitrification, are assumed to be directly proportional to the nitrification flux

548   (I_{NO3}) as

549
$$I_{NO} = \eta_{NO} \; I_{NO3}$$
$$I_{N2O} = \eta_{N2O} \; I_{NO3}.$$
(23)

550   where η_{NO} and η_{N2O} are dimensionless fractions (see Table A1) which determine what fractions

551   of nitrification flux are emitted as NO and N_2O.

552   **3.4.2 Denitrification**

553   Denitrification is the stepwise microbiological reduction of nitrate to NO, N_2O, and ultimately to

554   N_2 in complete denitrification. Unlike nitrification, however, denitrification is primarily an

555   anaerobic process (Tomasek et al., 2017) and therefore occurs when soil is saturated. As a result,

556   we use a different soil moisture scalar than for nitrification. Similar to nitrification, denitrification

557   is modelled as a function of soil moisture, soil temperature and the size of the NO_3^- pool as follows

558   to calculate the gaseous fluxes of NO, N_2O, and N_2.

559
$$E_{NO} \;\; = \mu_{NO} \;\; f_E(T_{0.5}) \; f_E(\theta) \; N_{NO3}$$
$$E_{N2O} = \mu_{N2O} \; f_E(T_{0.5}) \; f_E(\theta) \; N_{NO3}$$
$$E_{N2} \;\; = \mu_{N2} \;\; f_E(T_{0.5}) \; f_E(\theta) \; N_{NO3}$$
(24)

560   where μ_{NO}, μ_{N2O}, and μ_{N2} are coefficients (day^{-1}, see Table A1) that determine daily rates of

561   emissions of NO, N_2O, and N_2. The temperature scalar $f_E(T_{0.5})$ is exactly the same as the one for

562   nitrification ($f_I(T_{0.5})$) since denitrification is also assumed to occur over the same 0.5 m soil

563   depth. The soil moisture scalar $f_E(\theta)$ is given by

564
$$f_E(\theta) = 1 - \tanh\left(2.5 \left(\frac{1-w(\theta)}{1-w_d}\right)^2\right)$$
$$w(\theta) = \max\left(0, \min\left(1, \frac{\theta-\theta_w}{\theta_f-\theta_w}\right)\right)$$
(25)

565   where w is the soil wetness that varies between 0 and 1 as soil moisture varies between wilting

566   point (θ_w) and field capacity (θ_f), and w_d (see Table A1) is the threshold soil wetness for

567   denitrification below which very little denitrification occurs. Since arid regions are characterized

568   by low soil wetness values, typically below w_d, this leads to build up of the NO_3^- pool in arid

569   regions.

570   **3.4.3 NO_3^- leaching**

571   Leaching is the loss of water-soluble ions through runoff. In contrast to positively charged

572   NH_4^+ ions (i.e. cations), the NO_3^- ions do not bond to soil particles because of the limited exchange

573   capacity of soil for negatively charged ions (i.e., anions). As a result, leaching of N in the form of

574   NO_3^- ions is a common water quality problem, particularly over cropland regions. The leaching

575   flux (L_{NO3}, gN m^{-2} day^{-1}) is parameterized to be directly proportional to baseflow (b_t, Kg m^{-2} s$^-$

576   ^{1}) calculated by the physics module of CLASSIC and the size of the NO_3^- pool (N_{NO3}, gN m^{-2}).

577   Baseflow is the runoff rate from the bottommost soil layer.

$$L_{NO3} = 86400 \; \varphi \; b_t \; N_{NO3} \tag{26}$$

579   where the multiplier 86400 converts units to per day, and φ is the leaching coefficient (m^2 Kg^{-1},

580   see Table A1) that can be thought of as the soil particle surface area (m^2) that 1 Kg of water (or

581   about 0.001 m^3) can effectively wash to leach the nutrients.

582   **3.4.4 NH₃ volatilization**

583   NH₃ volatilization (V_{NH3}, gN m⁻² day⁻¹) is parametrized as a function of pool size of NH₄⁺,

584   soil temperature, soil pH, aerodynamic and boundary layer resistances, and atmospheric NH₃

585   concentration in a manner similar to Riddick et al. (2016) as

$$V_{NH4} = \vartheta \; 86400 \; \frac{1}{r_a + r_b} \left(\chi - [\text{NH}_{3,a}] \right) \qquad (27)$$

587   where ϑ is the dimensionless NH₃ volatilization coefficient (see Table A1) which is set to less than

588   1 to account for the fact that a fraction of ammonia released from the soil is captured by

589   vegetation, r_a (s m⁻¹) is the aerodynamic resistance calculated by the physics module of CLASSIC,

590   χ is the ammonia (NH₃) concentration at the interface of the top soil layer and the atmosphere

591   (g m⁻³), $[\text{NH}_{3,a}]$ is the atmospheric NH₃ concentration specified at 0.3×10⁻⁶ g m⁻³ following

592   Riddick et al. (2016), 86400 converts flux units from gN m⁻² s⁻¹ to gN m⁻² day⁻¹, and r_b (s m⁻¹) is

593   the boundary layer resistance calculated following Thom (1975) as

$$r_b = 6.2 \, u_*^{-0.67} \qquad (28)$$

595   where u_* (m/s) is the friction velocity provided by the physics module of CLASSIC. The ammonia

596   (NH₃) concentration at surface (χ), in a manner similar to Riddick et al. (2016), is calculated as

$$\chi = 0.26 \frac{N_{NH4}}{1 + K_H + K_H [H^+]/K_{NH4}} \qquad (29)$$

598   where the coefficient 0.26 is the fraction of ammonium in the top 10 cm soil layer assuming

599   exponential distribution of ammonium along the soil depth (given by $3e^{-3z}$, where z is the soil

600   depth), K_H (dimensionless) is the Henry's law constant for NH₃, K_{NH4} (mol L⁻¹) is the dissociation

601   equilibrium constant for aqueous NH₃, and H^+ (mol L⁻¹) is the concentration of hydrogen ion

602   that depends on the soil pH ($H^+ = 10^{-pH}$). K_H and K_{NH4} are modelled as functions of soil

603   temperature of the top 10 cm soil layer ($T_{0.1}$) following Riddick et al. (2016) as

$$K_H = 4.59 \, T_{0.1} \exp\left(4092 \left(\frac{1}{T_{0.1}} - \frac{1}{T_{ref,v}}\right)\right)$$

604   (30)

$$K_{NH4} = 5.67 \times 10^{-10} \exp\left(-6286 \left(\frac{1}{T_{0.1}} - \frac{1}{T_{ref,v}}\right)\right)$$

605   where $T_{ref,v}$ is the reference temperature of 298.15 K.

606

607   **3.5 Coupling of C and N cycles**

608   As mentioned earlier, the primary objective of coupling of C and N cycles is to be able to

609   simulate V_{cmax} as a function of leaf N amount (N_L, gN/m² land) for each PFT. This coupling is

610   represented through the following relationship

$$V_{cmax} = \Lambda \left(\frac{\Gamma_1 N_L}{3} + \Gamma_2\right)$$

611   (31)

612   where Γ_1 (39 μmol CO_2 gN⁻¹ s⁻¹) and Γ_2 (8.5 μmol CO_2 m⁻² s⁻¹) are global constants, except for

613   the broadleaf evergreen tree PFT for which a lower value of Γ_1 (15.3 μmol CO_2 gN⁻¹ s⁻¹) is used

614   as discussed below, and the number 3 represents an average LAI over vegetated areas (m²

615   leaves/m² land). Λ (≤ 1) is a scalar that reduces calculated V_{cmax} when C:N ratio of any plant

616   component ($C{:}N_i, i = L, S, R$) exceeds its specified maximum value ($C{:}N_{i,\max}, i = L, S, R$) (see

617   Table A1).

$$\Lambda = \exp\left(-\omega \, k_\Lambda\right)$$
$$\omega = e_L b_L + e_S b_S + e_R b_R$$

618   (32)

$$e_i = \max\left(0, C{:}N_i - C{:}N_{i,\max}\right)$$
$$b_i = \frac{1/C{:}N_{i,\max}}{1/C{:}N_{L,\max} + 1/C{:}N_{S,\max} + 1/C{:}N_{R,\max}}, i = L, S, R \qquad (33)$$

619

620 where k_Λ is a dimensionless parameter (see Table A1) and ω is dimensionless term that

621 represents excess C:N ratios above specified maximum thresholds ($e_i, i = L, S, R$) weighted by

622 $b_i, i = L, S, R$. When plant components do not exceed their specified maximum C:N ratio

623 thresholds, e_i is zero and Λ is one. When plants components exceed their specified maximum

624 C:N ratio thresholds, Λ starts reducing below one. This decreases V$_{cmax}$ and thus photosynthetic

625 uptake which limits the rate of increase of C:N ratio of plant components, depending on the value

626 of k_Λ.

627   The linear relationship between photosynthetic capacity and N_L (Evans, 1989; Field and

628 Mooney, 1986; Garnier et al., 1999) (used in equation 31) and between photosynthetic capacity

629 and leaf chlorophyll amount (Croft et al., 2017) is empirically observed. We have avoided using

630 PFT-dependent values of Γ_1 and Γ_2 for easy optimization of these parameter values but also

631 because such an optimization can potentially hide other model deficiencies. More importantly,

632 using PFT-independent values of Γ_1 and Γ_2 yields a more elegant framework whose successful

633 evaluation will provide confidence in the overall model structure.

634   As shown later in the results section, using Γ_1 and Γ_2 as global constants yields GPP values

635 that are higher in the tropical region than an observation-based estimate. This is not surprising

636 since tropical and mid-latitude regions are known to be limited by P (Vitousek, 1984; Aragão et

637 al., 2009; Vitousek et al., 2010; Du et al., 2020) and our framework currently doesn't model P

638 cycle explicitly. An implication of productivity that is limited by P is that changes in N_L are less

639   important. In the absence of explicit treatment of the P cycle, we therefore simply use a lower

640   value of Γ_1 for the broadleaf evergreen tree PFT which, in our modelling framework, exclusively

641   represents a tropical PFT. Although, a simple way to express P limitation, this approach yields the

642   best comparison with observation-based GPP, as shown later, because the effect of P limitation

643   is most pronounced in the high productivity tropical regions.

644   The second pathway of coupling between the C and N cycles occurs through

645   mineralization of litter and soil organic matter. During periods of higher temperature,

646   heterotrophic C respiration fluxes increase from the litter and soil organic matter pools and this

647   in turn implies an increased mineralization flux (via equation 16) leading to more mineral N

648   available for plants to uptake.

649   **4.0 Methodology**

650   **4.1 Model simulations and input data sets**

651   We perform CLASSIC model simulations with the N cycle for the pre-industrial period

652   followed by several simulations for the historical 1851-2017 period to evaluate the model's

653   response to different forcings, as summarized below. The simulation for the pre-industrial period

654   uses forcings that correspond to year 1850 and the model is run for thousands of years until its

655   C and N pools come into equilibrium. Global thresholds of net atmosphere-land C flux of 0.05

656   Pg/yr and net atmosphere-land N flux of 0.5 Tg N/yr are used to ensure the model pools have

657   reached equilibrium. The pre-industrial simulation, therefore, yields the initial conditions from

658   which the historical simulations for the period 1851-2017 are launched. To spin the mineral N

659   pools to their initial values, the plant N uptake and other organic processes were turned off while

660 the model used specified values of V_{cmax} and only the inorganic part of N cycle was operative.

661 Once the inorganic mineral soil N pools reached near equilibrium, the organic processes were

662 turned on. The model also uses an accelerated spin up procedure for the slow pools of soil organic

663 matter and mineral N. The input and output terms are multiplied by a factor greater than one

664 and this magnifies the change in pool size and therefore accelerates the spin up. Once the model

665 pools reach near equilibrium, the factor is set back to one.

666   To evaluate the model's response to various forcings over the historical period we

667 perform several simulations turning on one forcing at a time as summarized in Table 1. The

668 objective of these simulations is to see if the model response to individual forcings is consistent

669 with expectations. For example, in the CO2-only simulation only atmospheric CO_2 concentration

670 increases over the historical period, while all other forcings stay at their 1850 levels. In the N-

671 DEP-only simulation only N deposition increases over the historical period, and similarly for other

672 runs in Table 1. A "FULL" simulations with all forcings turned on is then also performed which we

673 compare to the original model without a N cycle which uses the photosynthesis downregulation

674 parameterization (termed "ORIGINAL" in Table 1). Finally, a separate pre-industrial simulation is

675 also performed that uses the same Γ_1 and Γ_2 globally (FULL-no-implicit-P-limitation). This

676 simulation is used to illustrate the effect of neglecting P limitation for the broadleaf evergreen

677 tree PFT in the tropics.

678   For the historical period, the model is driven with time-varying forcings that include CO_2

679 concentration, population density (used by the fire module of the model for calculating

680 anthropogenic fire ignition and suppression), land cover, and meteorological data. In addition,

681 for the N cycle module, the model requires time-varying atmospheric N deposition and fertilizer

682   data. The atmospheric CO_2 and meteorological data (CRU-JRA) are same as those used for the

683   TRENDY model intercomparison project for terrestrial ecosystem models for year 2018 (Le Quéré

684   et al., 2018). The CRU-JRA meteorological data is based on 6-hourly Japanese Reanalysis (JRA).

685   However, since reanalysis data typically do match observations they are adjusted for monthly

686   values based on the Climate Research Unit (CRU) data. This yields a blended product with sub-

687   daily temporal resolution that comes from the reanalysis and monthly means/sums that match

688   the CRU data to yield a meteorological product that can be used by models that require sub-daily

689   or daily meteorological forcing. These data are available for the period 1901-2017. Since no

690   meteorological data are available for the 1850-1900 period, we use 1901-1925 meteorological

691   data repeatedly for this duration and also for the pre-industrial spin up. The assumption is that

692   since there is no significant trend in the CRU-JRA data over this period, these data can be reliably

693   used to spin up the model to equilibrium. The land cover data used to force the model are based

694   on a geographical reconstruction of the historical land cover driven by the increase in crop area

695   following Arora and Boer (2010) but using the crop area data prepared for the Global Carbon

696   Project (GCP) 2018 following Hurtt et al. (2020). Since land cover is prescribed, the competition

697   between PFTs for space for the simulations reported here is switched off. The population data

698   for the period 1850-2017 are based on Klein Goldewijk et al. (2017) and obtained from

699   ftp://ftp.pbl.nl/../hyde/hyde3.2/baseline/zip/. The time-independent forcings consist of soil

700   texture and permeable depth data.

701   Time-varying atmospheric N deposition and fertilizer data used over the historical period

702   are also specified as per the TRENDY protocol. The fertilizer data are based on the N_2O model

703   intercomparison project (NMIP) (Tian et al., 2018) and available for the period 1860-2014. For

704   the period before 1860, 1860 fertilizer application rates are used. For the period after 2014,

705   fertilizer application rates for 2014 are used. Atmospheric N deposition data are from input4MIPs

706   (https://esgf-node.llnl.gov/search/input4mips/) and are the same as used by models

707   participating in CMIP6 for the historical period (1850-2014). For years 2015-2017 the N

708   deposition data corresponding to those from representative concentration pathway (RCP) 8.5

709   scenario are used. Figure 2 shows the time series of global annual values of externally specified

710   fertilizer input, and deposition of ammonium and nitrate, based on the TRENDY protocol, for the

711   six primary simulations. Geographical distribution of these inputs are also shown for the last 20

712   years from the FULL simulation corresponding to the 1998-2017 period. In Figure 2 (panels a, c

713   and e) ammonium and nitrate deposition, and fertilizer input stay at their pre-industrial level for

714   simulations in which these forcings do not increase over the historical period. As mentioned

715   earlier, N deposition is split evenly into ammonium and nitrate. The values in parenthesis in

716   Figure 2a legend, and in subsequent time series plots, show average values over the 1850s, the

717   last 20 years (1998-2017) of the simulations, and the change between these two periods. The

718   present day values of fertilizer input and N deposition are consistent with other estimates

719   available in the literature (Table 2). The fertilizer input rate in the simulation with all forcings

720   except land use change (FULL-no-LUC, blue line), that is with no increase in crop area over its

721   1850 value, is 50 Tg N yr^{-1} compared to 91 Tg N yr^{-1} in the FULL simulation, averaged over the

722   1998-2017 period. The additional 41 Tg N yr^{-1} of fertilizer input occurs in the FULL simulation due

723   to the increase in crop area but also due to the increasing fertilizer application rates over the

724   historical period. Geographical distribution of the fertilizer application rates in Figure 2b shows

725   that they are concentrated in regions with crop area and with values as high as 16 gN m^{-2} yr^{-1}

726   especially in eastern China. The N deposition rates (Figure 2d, 2f) are more evenly distributed

727   geographicaly than the fertilizer applications rates, as would be expected, since emissions are

728   transported downstream from their point sources. Areas with high emissions like the eastern

729   United States, India, eastern China, and Europe, however, still stand out as areas that receive

730   higher N deposition.

731   **4.2 Evaluation data sources**

732   We compare globally-summed annual values of N pools and fluxes with observations and

733   other models, and where available their geographical distribution and seasonality. In general,

734   however, much less observation-based data are available to evaluate simulated terrestrial N

735   cycle components than for C cycle components. As a result, N pools and fluxes are primarily

736   compared to results from both observation-based studies and other modelling studies

737   (Bouwman et al., 2013; Fowler et al., 2013; Galloway et al., 2004; Vitousek et al., 2013; Zaehle,

738   2013). Since the primary purpose of the N cycle in our framework is to constrain the C cycle, we

739   also compare globally-summed annual values of GPP and net atmosphere-land CO_2 flux, and their

740   zonal distribution with available observation-based and other estimates. The observation-based

741   estimate of GPP is from Beer et al. (2010), who apply diagnostic models to extrapolate ground-

742   based carbon flux tower observations from about 250 stations to the global scale. Observation-

743   based net atmosphere-land CO_2 flux is from Global Carbon Project's 2019 assessment

744   (Friedlingstein et al., 2019).

745   **5.0 Results**

746   **5.1 N inputs – biological N fixation**

747   Figure 3 (panels a, c, e) shows the time series of annual values BNF and its natural and

748   anthropogenic components from the six primary simulations summarized in Table 1. BNF stays

749   at its pre-industrial value of around 80 Tg N yr^{-1} in the CO2-only and N-DEP-only simulations. In

750   the CLIM-only (indicated by magenta coloured line) and the FULL-no-LUC (blue line) simulations

751   the change in climate, associated with increases in temperature and precipitation over the 1901-

752   2017 period (see Figure A2 in the appendix), increases BNF to about 85 Tg N yr^{-1}. In our

753   formulation (equation 3) BNF is positively impacted by increases in temperature and

754   precipitation. In the LUC+FERT-only simulation (dark green line) the increase in crop area

755   contributes to an increase in global BNF with a value around 110 Tg N yr^{-1} for the present day,

756   since a higher BNF per unit crop area is assumed than for natural vegetation. Finally, in the FULL

757   simulation (red line) the 1998-2017 average value is around 117 Tg N yr^{-1} due both to changes in

758   climate over the historical period and the increase in crop area. Our present day value of global

759   BNF is broadly consistent with other modelling and data-based studies as summarized is Table 2.

760   Panels c and e in Figure 3 show the decomposition of the total terrestrial BNF into its natural

761   (over non-crop PFTs) and anthropogenic (over C_3 and C_4 crop PFTs) components. The increase in

762   crop area over the historical period decreases natural BNF from its pre-industrial value of 59 to

763   54 Tg N yr^{-1} for the present day as seen for the LUC+FERT-only simulation (green line) in Figure

764   3c, while anthropogenic BNF over agricultural area increases from 21 to 56 Tg N yr^{-1} (Figure 3e).

765   Figure 3c and 3e show that the increase in BNF (Figure 3a) in the FULL simulation is caused

766   primarily by an increase in crop area. Our present day values of natural and anthropogenic BNF

767   are also broadly consistent with other modelling and data-based studies as summarized in Table

768   2.

769   Figure 3 (panels b, d, and f) shows the geographical distribution of simulated BNF and its

770   natural and anthropogenic components. The geographical distribution of BNF (Figure 3a) looks

771   very similar to the current distribution of vegetation (not shown) with warm and wet regions

772   showing higher values than cold and dry regions since BNF is parameterized as a function of soil

773   temperature and soil moisture. Anthropogenic BNF only occurs in regions where crop area exists

774   according to the specified land cover and it exhibits higher values than natural BNF in some

775   regions because of its higher value per unit area (see section 3.2.1).

776   At the global scale, and for the present day, natural BNF (59 Tg N yr^{-1}) is overwhelmed by

777   anthropogenic sources: anthropogenic BNF (60 Tg N yr^{-1}), fertilizer input (91.7 Tg N yr^{-1}), and

778   atmospheric N deposition increase since the pre-industrial era (~45 Tg N yr^{-1}). Currently humanity

779   fixes more N than the natural processes (Vitousek, 1994).

780   **5.2 C and N pools, fluxes response to historical changes in forcings**

781   To understand the model response to changes in various forcings over the historical

782   period we first look at the evolution of global values of primary C and N pools, and fluxes, shown

783   in Figures 4 through 8. Figure 4a shows the time evolution of global annual GPP values, the

784   primary flux of C into the land surface, for the six primary simulations, the ORIGINAL simulation

785   performed with the model version with no N cycle, and the ORIG-UNCONST simulation with no

786   photosynthesis downregulation (see Table 1). The unconstrained increase in GPP (35.6 Pg C yr^{-1}

787   over the historical period) in the ORIG-UNCONST simulation (dark cyan line) is governed by the

788   standard photosynthesis model equations following Farquhar et al. (1980) and Collatz et al.

789   (1992) for C_3 and C_4 plants, respectively. Downregulation of photosynthesis in the ORIGINAL

790   simulation (purple line) is modelled on the basis of equation (1), while in the FULL simulation (red

791   line) photosynthesis downregulation results from a decrease in V_{cmax} values (Figure 5d) due to a

792   decrease in leaf N amount (Figure 5b). We will compare the FULL and ORIGINAL simulations in

793   more detail later. The simulations with individual forcings, discussed below, provide insight into

794   the combined response of GPP to all forcings in the FULL simulation.

795   **5.2.1 Response to increasing CO_2**

796   The response of C and N cycles to increasing CO_2 in the CO2-only simulation (orange lines

797   in Figure 4) is the most straightforward to interpret. A CO_2 increase causes GPP to increase by 7.5

798   Pg C yr^{-1} above its pre-industrial value (Figure 4a), which in turn causes vegetation (Figure 4b),

799   leaf (Figure 4c), and soil (Figure 4d) carbon mass to increase as well. The vegetation and leaf N

800   amounts (orange line, Figures 5a and 5b), in contrast, decrease in response to increasing CO_2.

801   This is because N gets locked up in the soil organic matter pool (Figure 5c) in response to an

802   increase in the soil C mass (due to the increasing GPP), litter inputs which are now rich in C (due

803   to CO_2 fertilization) but poor in N (since N inputs are still at their pre-industrial level), and the fact

804   that the C:N ratio of the soil organic matter is fixed at 13. This response to elevated CO_2 which

805   leads to increased C and decreased N in vegetation is consistent with meta-analysis of 75 field

806   experiments of elevated CO_2 (Cotrufo et al., 1998). A decrease in N in leaves (orange line, Figure

807   5b) leads to a concomitant decrease in maximum carboxylation capacity (V_{cmax}) (orange line,

808   Figure 5d) and as a result GPP increases at a much slower rate in the CO2-only simulation than in

809   the ORIG-UNCONST simulation (Figure 4a). Due to the N accumulation in the soil organic matter

810   pool, the NH_4^+ and NO_3^- (Figures 5e and 5f) pools also decrease in size in the CO2-only simulation.

811   Figure 6 shows the time series of N demand, plant N uptake and its split between passive

812   and active N uptakes. The plant N demand in the CO2-only simulation (Figure 6a, orange line)

813   increases from its pre-industrial value of 1512 Tg N/yr to 1639 Tg N/yr for the present day since

814   the increasing C input from increasing GPP requires higher N input to maintain preferred

815   minimum C:N ratio of plant tissues. However, since mineral N pools decrease in size over the

816   historical period in this simulation (Figures 5e and 5f), the total plant N uptake (Figure 6b)

817   reduces. Passive plant N uptake is directly proportional to pool sizes of NH_4^+ and NO_3^- and

818   therefore it reduces in response to increasing CO_2. Active plant N uptake, which compensates for

819   insufficient passive N uptake compared to the N demand, also eventually starts to decline as it

820   also depends on mineral N pool sizes. The eventual result of increased C supply and reduced N

821   supply is an increase in the C:N ratio of all plant components and litter (Figure 7). The

822   preindustrial total N uptake of around 960 Tg N/yr (Figure 6b) is lower than the preindustrial N

823   demand (1512 Tg N/yr, Figure 6a) despite the sum of global NH_4 and NO_3 pool sizes being around

824   4000 Tg N (Figures 5e and 5f). This is because of the mismatch between where the pools are high

825   and where the vegetation actually grows and the fact that plant N uptake is limited by its rate.

826   As a result, in our model, even in the preindustrial era vegetation is N limited.

827   Figure 8 shows the net mineralization flux (the net transfer of mineralized N from litter

828   and humus pools to the mineral N pools as a result of the decomposition of organic matter),

829   nitrification (N flux from NH_4^+ to the NO_3^- pool), and the gaseous and leaching losses from the

830   mineral pools. The net mineralization flux reduces in the CO2-only simulation (Figure 8a, orange

831   line) as N gets locked up in the soil organic matter. A reduction in the NH_4^+ pool size in response

832   to increasing CO_2 also yields a reduction in the nitrification flux over the historical period (Figure

833   8b, orange line) since nitrification depends on the NH_4^+ pool size (equation 19). Finally, leaching

834   from the NO_3^- pool (Figure 8c), NH_3 volatilization (Figure 8d), and the gaseous losses associated

835   with nitrification from the NH_4^+ pool (Figure 8e) and denitrification from the NO_3^- pool (Figure 8f)

836   all reduce in response to reduction in pool sizes of NH_4+ and NO_3- in the CO2-only simulation.

837   **5.2.2 Response to changing climate**

838   The perturbation due to climate change alone over the historical period in the CLIM-only

839   simulation (magenta coloured lines in Figures 4 to 8) is smaller than that due to increasing CO_2.

840   In Figure 4a, changes in climate over the historical period increase GPP slightly by 3.60 Pg C yr^{-1}

841   which in turn slightly increases vegetation (including leaf) C mass (Figure 4b,c). The litter and soil

842   carbon mass (Figure 4d), however, decrease slightly due to increased decomposition rates

843   associated with increasing temperature (see Figure A2b). Both the increase in BNF due to

844   increasing temperature (magenta line in Figure 2a), and the reduction in litter and soil N mass

845   (Figure 5c) due to increasing decomposition and higher net N mineralization (Figure 8a, magenta

846   line), make more N available. This results in a slight increase in vegetation and leaf N mass

847   (Figures 5a and 5b) and the NH_4^+ (Figure 5e) pool which is the primary mineral pool in soils under

848   vegetated regions. The global NO_3^- pool, in contrast, decreases in the CLIM-only simulation

849   (Figure 5f) with the reduction primarily occurring in arid regions where the NO_3^- amounts are very

850   large (see Figure 9 that shows the geographical distribution of the primary C and N pools). The

851   geographical distribution of NH_4^+ (Figure 9a) generally follows the geographical distribution of

852   BNF, but with higher values in areas where cropland exists and where N deposition is high. The

853   geographical distribution of NO_3^- (Figure 9b) generally shows lower values than NH_4^+ except in

854   the desert regions where lack of denitrification leads to a large buildup of the NO_3^- pool (as

855   explained earlier in section 3.4.2). Although Figure 9 shows the geographical distribution of

856   mineral N pools from the FULL simulation, the geographical distribution of pools are broadly

857   similar between different simulations with obvious differences such as lack of hot spots of N

858   deposition and fertilizer input in simulations in which these forcings stay at their pre-industrial

859   levels. Figure 9 also shows the simulated geographical distribution of C and N pools in the

860   vegetation and soil organic matter. The increase in GPP due to changing climate increases the N

861   demand (Figure 6a, magenta line) but unlike the CO2-only simulation, the plant N uptake

862   increases since the NH_4^+ and NO_3^- pools increase in size over the vegetated area in response to

863   increased mineralization (Figure 8a, magenta line) and increased BNF (Figure 3a, magenta line).

864   The increase in plant N uptake comes from the increase in passive plant N uptake (Figure 6c)

865   while the active plant N uptake reduces (Figure 6d). Active and passive plant N uptakes are

866   inversely correlated. This is by design since active plant N uptake increases when passive plant N

867   uptake reduces and vice-versa, although eventually both depend on the size of available mineral

868   N pools. Enhancement of plant N uptake due to changes in climate, despite increases in GPP

869   associated with a small increase in V_{cmax} (Figure 5d), leads to a small reduction in the C:N ratio of

870   all plant tissues (Figure 7). The litter C:N, in contrast, shows a small increase since not all N makes

871   its way to the litter as a specified fraction of 0.54 (Table A1) leaf N is resorbed from deciduous

872   trees leaves prior to leaf fall (Figure 7e). Although the leaf C:N ratio decreases in the CLIM only

873   simulation, in response to increased BNF and increased mineralization, this decrease is not large

874   enough to overcome the effect of resorption and as a result the C:N litter increases.

875   Finally, the small increase in pool sizes of NH_4^+ and NO_3^- leads to a small increase in

876   leaching, volatilization, and gaseous losses associated with nitrification and denitrification (Figure

877   8).

878   **5.2.3 Response to N deposition**

879   The simulated response of GPP to changes in N deposition (brown line) over the historical

880   period is smaller than that for CO_2 and climate (Figure 4a). The small increase in GPP of 2.0 Pg C

881   yr^{-1} leads to commensurately small increases in vegetation (Figure 4b) and litter plus soil (Figure

882   4d) C mass. Vegetation and leaf N mass (Figure 5a,b) also increase in response to N deposition

883   and so do mineral pools of NH_4^+ and NO_3^- (Figure 5e,f). The increase in GPP in the simulation with

884   N deposition results from an increase in V_{cmax} rates (Figure 5d) associated with an increase in leaf

885   N amount (Figure 5b). N demand increases marginally and so does plant N uptake in response to

886   N deposition (Figure 6). As would be intuitively expected, the C:N ratio of the whole plant, its

887   components of leaves, stem, and root, and litter decreases slightly in response to N deposition

888   (Figure 7). Net N mineralization, nitrification, leaching, volatilization, and gaseous losses

889   associated with nitrification and denitrification all increase in response to N deposition (Figure

890   8).

891   **5.2.4 Response to LUC and fertilizer input**

892   The simulated response to LUC, which reflects an increase in crop area, and increased

893   fertilizer deposition rates over the historical period is shown by dark green lines in Figures 4

894   through 8. The increase in fertilizer input is a much bigger perturbation to the N cycle system

895   than N deposition. Figure 2 shows that at the global scale the fertilizer inputs increase from 0 to

896   ~92 Tg N/yr over the historical period, while the combined NH_4^+ and NO_3^- N deposition rate

897   increases from around 20 to 65 Tg N/yr. In addition, because of higher per unit area BNF rates

898   over crop area than natural vegetation, the increase in crop area in this simulation leads to an

899   increase in anthropogenic BNF from about 20 to 56 Tg N/yr over the historical period. All together

900   increasing crop area and fertilizer inputs imply an additional ~130 Tg N/yr being input into the

901   terrestrial N cycle at the present day since the pre-industrial period, compared to an increase of

902   only 45 Tg N/yr for the N deposition forcing.

903   The global increase in fertilizer input over the historical period leads to higher NH_4^+ and

904   NO_3^- pools (Figures 5e and 5f). Although both fertilizer and BNF contribute to the NH_4^+ pool, the

905   NO_3^- pool also increases through the nitrification flux (Figure 8b). An increase in crop area over

906   the historical period results in deforestation of natural vegetation that reduces vegetation

907   biomass (Figure 4b). However, soil carbon mass also decreases (Figure 4d) despite higher litter

908   inputs. This is because a higher soil decomposition rate is assumed over cropland areas to

909   simulate soil carbon loss as empirical measurements of soil carbon show over deforested areas

910   which are converted to croplands (Wei et al., 2014). Fertilizer application only occurs over crop

911   areas which increases the V_{cmax} rates for crops and, as expected, this yields an increase in globally-

912   averaged V_{cmax} (Figure 5d). A corresponding large increase in leaf N amount (Figure 5b) is,

913   however, not seen because vegetation (and therefore leaf) N (Figure 5a,b) is also lost through

914   deforestation. In addition, V_{cmax} is essentially a flux (expressed per unit leaf area) that is averaged

915   over the whole year while leaf and vegetation N pools are sampled at the end of each year and

916   all crops in the northern hemisphere above 30° N are harvested before the year end. Vegetation

917   N mass, in fact, decreases in conjunction with vegetation C mass (Figure 4b). Plant N demand

918   reduces (Figure 6a) and plant N uptake increases (Figure 6b) driven by crop PFTs in response to

919   fertilizer input, as would be intuitively expected. The increase in plant N uptake comes from the

920   increase in passive N uptake, in response to increases in pool sizes of NH_4^+ and NO_3^- over crop

921   areas, while active plant N uptake decreases since passive uptake can more than keep up with

922   the demand over cropland area. While the C:N ratio of vegetation biomass decreases over

923   cropland area in response to fertilizer input (not shown) this is not seen in the globally-averaged

924   C:N ratio of vegetation (Figure 7a) and its components because C and N are also lost through

925   deforestation and the fact that crop biomass is harvested. The C:N of the global litter pool,

926   however, decreases in response to litter from crops which gets rich in N as fertilizer application

927   rates increase. Finally, in Figure 8, global net N mineralization, nitrification, leaching,

928   volatilization, and gaseous losses associated with nitrification and denitrification all increase by

929   a large amount in response to an increase in fertilizer input.

930   **5.2.5 Response to all forcings**

931   We can now evaluate and understand the simulated response of the FULL simulation to

932   all forcings (red line in Figures 4 through 8). The increase in GPP in the FULL simulation (14.5 Pg

933   C/yr) in Figure 4a over the historical period is driven by GPP increase associated with increase in

934   CO_2 (7.5 Pg C/yr), changing climate (3.6 Pg C/yr), and N deposition (2.0 Pg C/yr). The increases

935   associated with these individual forcings add up to 13.1 Pg C/yr indicating that synergistic effects

936   between forcings contribute to the additional 1.4 Pg C/yr increase in GPP. The changes in

937   vegetation and soil plus litter carbon mass (Figures 4b and 4d) in the FULL simulation are similarly

938   driven by these three factors but, in addition, LUC contributes to decreases in vegetation and soil

939   carbon mass as natural vegetation is deforested to accommodate for increases in crop area.

940   Vegetation and leaf N mass (Figures 5a and 5b) decrease in the FULL simulation driven primarily

941   by the response to increasing CO_2 (orange line compared to the red line) while changes in litter

942   and soil N mass are affected variably by all forcings (Figure 5c). Changes in V_{cmax} (Figure 5d) are

943   similarly affected by all forcings: increasing CO_2 leads to a decrease in globally-averaged V_{cmax}

944   values while changes in climate, N deposition, and fertilizer inputs lead to increases in V_{cmax}

945   values with the net result being a small decrease over the historical period. The increase in global

946   NH_4^+ mass in the FULL simulation is driven primarily by the increase in fertilizer input (Figure 5e,

947   red versus green line) while the changes in NO_3^- mass are primarily the result of changes in

948   climate (Figure 5f, magenta line) which causes a decrease in NO_3^- mass from about 1940 to 1970

949   and N deposition and fertilizer input (Figure 5f, green and brown lines) which contribute to the

950   increase in NO_3^- mass later on in the historical period. The increase in N demand (Figure 6a) over

951   the historical period is also driven primarily by the increase in atmospheric CO_2. Plant N uptake

952   (Figure 6b) decreases in response to increasing CO_2 but increases in response to changes in

953   climate, N deposition, and fertilizer inputs such that the net change over the historical is a small

954   decrease. The increase in the C:N ratio of vegetation and its components (leaves, stem, and root)

955   is driven primarily by an increase in atmospheric CO_2 (Figure 7a, red versus orange line). Litter

956   C:N in the FULL simulation, in contrast, does not change substantially over the historical period

957   in a globally-averaged sense as the increase in the C:N ratio of litter associated with an increase

958   in atmospheric CO_2 is mostly compensated by the decrease associated with an increase in N

959   deposition and fertilizer application. The simulated change in global net N mineralization (Figure

960   8a) in the FULL simulation, over the historical period, is small since the decrease in net N

961   mineralization due to increasing CO_2 (orange line) is compensated by the increase caused by

962   changes in climate, N deposition, and fertilizer inputs (magenta, brown, and green lines

963   respectively). The remaining fluxes of nitrification, NO_3^- leaching, NH_3 volatilization, and gaseous

964   losses associated with nitrification and denitrification in the FULL simulation (Figure 8) are all

965   strongly influenced by fertilizer input (green line compared to red line).

966   Table 2 compares simulated values of all primary N pools and fluxes from the FULL

967   simulation with other modelling and quasi observation-based studies. Simulated values are

968   averaged over the 1998-2017 period. Where available, time-periods for other modelling and

969   quasi observation-based studies to which estimates correspond are also noted. For the most part

970   simulated pools and fluxes lie within the range of existing studies with the exception of N_2 and

971   NO emissions that are somewhat higher.

972   **5.2.6 Response to all forcings except LUC**

973   The FULL-no-LUC simulation includes all forcings except LUC (blue line in Figures 4

974   through 8) and corroborates several of the points mentioned above. In this simulation crop area

975   stays at its 1850 value. Figure 2b (blue line) shows increasing global fertilizer input in this

976   simulation despite crop area staying at its 1850 value since fertilizer application rates per unit

977   area increase over the historical period. In the absence of the LUC, vegetation C mass (Figure 4b)

978   and soil plus litter C (Figure 4d) and N (Figure 5c) are higher in the FULL-no-LUC compared to the

979   FULL simulation. N demand (Figure 6a) is slightly higher in FULL-no LUC than in FULL simulation

980   because there is more standing vegetation biomass that is responding to increasing CO_2. The

981   increase in volatilization, leaching, and gaseous losses associated with nitrification and

982   denitrification (Figures 8c-8f) are all primarily caused by increased fertilizer input over the

983   specified 1850 crop area. The increase in N losses associated with these processes, over the

984   historical period, is much lower in the FULL-no-LUC simulation than in the FULL simulation since

985   crop area stays at its 1850 values.

986   **5.3 Comparison of FULL and ORIGINAL simulations**

987   We now compare the results from the FULL simulation that includes the N cycle with that

988   from the ORIGINAL simulation that does not include the N cycle. Both simulations are driven with

989   all forcings over the historical period. Figure 4a shows that the global GPP values in the FULL (red

990   line) and ORIGINAL (purple line) simulations are quite similar although the rate of increase of GPP

991   in the FULL simulation is slightly higher than in the ORIGINAL simulation. As a result, simulated

992   global vegetation biomass is somewhat higher in the FULL simulation (Figure 4b). The simulated

993   global litter and soil carbon mass (Figure 4d) is, however, lower in the FULL simulation (1073 Pg

994   C) compared to the ORIGINAL simulation (1142 Pg C) and this decrease mainly comes from a

995   decrease at higher latitudes (not shown) due to a decrease in GPP (Figure 10a). The lower GPP in

996   the FULL simulation, combined with the slow decomposition at cold high latitudes, results in a

997   lower equilibrium for litter and soil carbon compared with the ORIGINAL simulation. Litter mass

998   contributes about 80 Pg C to the total dead carbon mass. Overall both estimates of 1073 Pg C

999   and 1142 Pg C are somewhat lower than the bulk density corrected estimate of 1230 Pg C based

1000   on the Harmonized World Soil Database (HWSD) v.1.2 (Köchy et al., 2015). One reason for this is

1001   that CLASSIC does not yet represent permafrost related soil C processes.

1002   Figure 10a shows that the zonal distribution of GPP from the FULL and ORIGINAL

1003   simulations, for the 1998-2017 period, compares reasonably well to the observation-based

1004 estimate from Beer et al. (2010). The FULL simulation has slightly lower productivity at high-

1005 latitudes than the ORIGINAL simulation, as mentioned above. Overall, however, the inclusion of

1006 the N cycle does not change the zonal distribution of GPP in the model substantially, which is

1007 determined primarily by the geographical distribution of climate. Figure 10b compares the zonal

1008 distribution of GPP from the pre-industrial simulation (corresponding to 1850s) from the FULL

1009 and FULL-with-no-implicit-P-limitation simulations to illustrate the high GPP in the tropics where

1010 P and not N limitation affects GPP and the reason for choosing a lower value of Γ_1 in equation

1011 (31) for the broadleaf evergreen tree PFT.

1012   The global GPP in the ORIGINAL and FULL simulations averaged over the period 1998-

1013 2017 (120.0 and 120.4 PgC/yr, respectively) are around 15% lower compared to that in the ORIG-

1014 UNCONST simulation (142 PgC/yr), as shown in Figure 4a, yielding a global downregulation factor

1015 of about 0.85. Figure 10c shows how downregulation works in the ORIGINAL and FULL

1016 simulations in a zonally-averaged sense. Ratios of annual GPP averaged over the 1998-2017

1017 period from the ORIGINAL versus ORIG-UNCONST simulations, and FULL versus ORIG-UNCONST

1018 simulations were first calculated for each grid cell and then zonally-averaged over the land grid

1019 cells. Ratios can be misleading especially for grid cells with low values, for example, in the desert

1020 regions. In addition, these ratios also depend on the specified V_{cmax} values in the ORIG-UNCONST

1021 simulation. In Figure 10c, the purple line for the ORIGINAL simulation exhibits values around 0.8

1022 consistent with the global downregulation of around 0.85 and the fact that the same scalar

1023 downregulation multipler is used everywhere on the globe (equation 1). The red line for the FULL

1024 simulation, however, indicates a pattern of higher downregulation at high-latitudes. The peaks

1025 in red line, especially the one around 23°N (Sahara desert), are due to higher values in selected

1026   grid cells in dry and arid regions where the build-up of NO_3^- in the soil (due to reduced

1027   denitrification) increases V_{cmax} and thus GPP in the run with N cycle leading to higher ratios

1028   although the absolute GPP values still remain low.

1029   Figure 11a compares globally-summed net atmosphere-land CO_2 flux from the FULL,

1030   FULL-no-LUC, and ORIGINAL simulations with quasi observation-based estimates from the 2019

1031   Global Carbon Project (Friedlingstein et al., 2019). There are two kinds of estimates in Figure 11a

1032   from Friedlingstein et al. (2019): the first is the net atmosphere-land CO_2 flux for the decades

1033   spanning the 1960s to the 2000s which are shown as rectangular boxes with their corresponding

1034   mean values and ranges, and the second is the terrestrial sink from 1959 to 2018 (dark yellow

1035   line). Positive values indicate a sink of carbon over land and negative values a source. The

1036   difference between the net atmosphere-land CO_2 flux and the terrestrial sink is that the

1037   terrestrial sink minus the LUC emissions yields the net atmosphere-land CO_2 flux. The

1038   atmosphere-land CO_2 flux from the FULL-no-LUC simulation (blue line) is directly comparable to

1039   the terrestrial sink since 1959, since the FULL-no-LUC simulation includes no LUC, and shows that

1040   the simulated terrestrial sink compares fairly well to the estimates from Friedlingstein et al.

1041   (2019). Averaged over the period 1959-2017, the modelled and Global Carbon Project values are

1042   2.0 and 2.1 Pg C/yr, respectively. The net atmosphere-land CO_2 flux from the FULL simulation

1043   mostly lies within the uncertainty range for the five decades considered, although it is on the

1044   higher side compared to estimates from Friedlingstein et al. (2019). The reason for this is that

1045   LUC emissions in CLASSIC are much lower than observation-based estimates, as discussed below

1046   in context of Figure 11c. CLASSIC simulates LUC emissions only in response to changes in crop

1047   area whereas changes in pasture area and wood harvesting also contribute to LUC emissions. The

1048   net-atmosphere land CO_2 flux from the ORIGINAL simulation compares better with the estimates

1049   from Friedlingstein et al. (2019), than the FULL simulation, because the photosynthesis down-

1050   regulation parameter in the ORIGINAL simulation has been adjusted despite discrepancies in

1051   simulated LUC processes.

1052   Figure 11b compares the zonal distribution of simulated net atmosphere-land CO_2 flux

1053   from the FULL and ORIGINAL simulations with the model-mean and range from the terrestrial

1054   ecosystem models that participated in the 2019 TRENDY model intercomparison and contributed

1055   results to 2019 Global Carbon Project (Friedlingstein et al., 2019). The carbon sink simulated by

1056   CLASSIC in the northern hemisphere is broadly comparable to the model-mean estimate from

1057   the TRENDY models. However, in the tropics CLASSIC simulates a much stronger sink than the

1058   model-mean, likely because of its lower LUC emissions.

1059   **5.4 Contribution of forcings to land C sink and sources**

1060   Figure 11c shows cumulative net atmosphere-land CO_2 flux for the 1850-2017 period from

1061   the six primary simulations with N cycle. These simulations facilitate the attribution of carbon

1062   uptake and release over the historical period to various forcings. The cumulative terrestrial sink

1063   in the FULL-no-LUC simulation for the period 1850-2017 is simulated to be ~153 Pg C and this

1064   compares reasonably well with the estimate of 185 ± 50 Pg C for the period 1850-2014 from Le

1065   Quéré et al. (2018). Increase in CO_2 (~115 Pg C), change in climate (~3 Pg C), and N deposition

1066   (~19 Pg C) all contribute to this terrestrial sink. These three contributions add up to 137 Pg C so

1067   the additional 16 Pg C is contributed by the synergistic effects between the three forcings.

1068   Quantified in this way, the contribution of increasing CO_2 (115 out of 137 Pg C), climate change

1069 (3 out of 137 Pg C), and N deposition (19 out of 137 Pg C) to carbon uptake by land over the

1070 historical period (1850-2017) is calculated to be 84%, 2%, and 14%, respectively. Cumulative LUC

1071 emissions simulated for the period 1850-2017 by CLASSIC can be estimated using a negative

1072 cumulative net-atmosphere-land CO_2 flux of ~66 Pg C from the LUC+FERT-only simulation or by

1073 the differencing the FULL and FULL-no-LUC simulations (~71 Pg C). While LUC emissions are highly

1074 uncertain, both of these estimates are much lower than the 195 ± 75 Pg C estimate from Le Quéré

1075 et al. (2018).

1076 **6.0 Discussion and conclusions**

1077   The interactions between terrestrial C and N cycles are complex and our understanding

1078 of these interactions, and their representation in models, is based on empirical observations of

1079 various terrestrial ecosystem processes. In this paper, we have evaluated the response of these

1080 interactions by perturbing the coupled C and N cycle processes in the CLASSIC model with one

1081 forcing at a time over the historical period: 1) increase in CO_2, 2) change in climate, 3) increase in

1082 N deposition, and 4) LUC with increasing fertilizer input. These simulations are easier to interpret

1083 and the model response can be evaluated against both our conceptual knowledge as well as

1084 empirical observation-based data. Our assumption is that, if the model response to individual

1085 forcings is realistic and consistent with expectations based on empirical observations then the

1086 response of the model to all forcings combined will also be realistic and easier to interpret,

1087 although we do expect and see synergistic effects between forcings.

1088   The simulated response of coupled C and N cycles in CLASSIC to increasing atmospheric

1089 CO_2 is an increase in the C:N ratio of vegetation components due to an increase in their C content

1090   but also a decrease in their N content. This model response is conceptually consistent with a

1091   meta-analysis of 75 field experiments of elevated CO_2 as reported in Cotrufo et al. (1998) who

1092   find an average reduction in tissue N concentration of 14%. Most studies analyzed in the Cotrufo

1093   et al. (1998) meta-analysis used ambient CO_2 of around 350 ppm and elevated CO_2 of around

1094   650-700 ppm. In comparison, the plant N concentration in CLASSIC reduces by ~26% in response

1095   to a gradual increase in atmospheric CO_2 from 285 ppm to 407 ppm (an increase of 122 ppm)

1096   over the 1850-2017 period (whole plant C:N ratio increases from 142.6 to 194.1 in the CO2-only

1097   simulation, Figure 7a). These two estimates cannot be compared directly - the majority (59%) of

1098   Free-Air Carbon dioxide Enrichment (FACE) experiments last less than 3 years (Jones et al., 2014)

1099   and the vegetation experiences a large CO_2 change of around 300-350 ppm while the duration of

1100   our historical simulation is 167 years and the gradual increase in CO_2 of 122 ppm over the

1101   historical period is much smaller.

1102   The response of our model to CO_2 increase over the historical period is also consistent

1103   with the meta-analysis of McGuire et al. (1995) who report an average decrease in leaf N

1104   concentration of 21% in response to elevated CO_2 based on 77 studies, which is the primary

1105   reason for downregulation of photosynthetic capacity. The simulated decrease in leaf N

1106   concentration in our study for the CO2-only experiment is around 27% (leaf C:N ratio increases

1107   from 42.8 to 58.6 in the CO2-only simulation, Figure 7b). Although, the same caveats that apply

1108   to the comparison with the Cotrufo et al. (1998) study also apply to this comparison. The

1109   decrease in whole plant and leaf N concentrations in our results is conceptually consistent with

1110   the meta-analyses of McGuire et al. (1995) and Cotrufo et al. (1998). The decrease in whole plant

1111   N concentration in our CO2-only and FULL simulations is the result of an increase in both tissue

1112   C amount and a decrease in N amount. The decrease in tissue N amount is, in fact, necessary in

1113   our modelling framework to induce the required downregulation of photosynthesis to simulate

1114   the land carbon sink realistically over the historical period.

1115   The meta-analysis of Liang et al. (2016) reports an increase in above and belowground

1116   plant N pools in response to elevated CO_2 associated with increase in BNF but since their results

1117   are based on pool sizes they cannot be compared directly to the N concentration based results

1118   from McGuire et al. (1995) and Cotrufo et al. (1998). Liang et al. (2016) also report results from

1119   short-term ($\leq$ 3 years) and long-term (between 3 to 15 years) studies separately (their Figure 3).

1120   They show that the increase in total plant and litter N pools become smaller for long-term studies.

1121   Regardless, the difference in time scales of empirical studies and the real world is a caveat that

1122   will always make it difficult to evaluate model results over long time scales.

1123   The response of C and N cycles to changes in climate in our model (in the CLIM-only

1124   simulation) is also conceptually realistic. Globally, GPP increases in response to climate that

1125   gradually gets warmer and wetter (see Figure A2) and as a result vegetation biomass increases.

1126   Soil carbon mass, however, decreases (despite increase in NPP inputs) since warmer

1127   temperatures also increase heterotrophic respiration (not shown). As a result of increased

1128   decomposition of soil organic matter, net N mineralization increases and together with increased

1129   BNF the overall C:N ratio of vegetation and leaves decreases, which leads to a V_{cmax} increase. The

1130   small increase in V_{cmax}, due to increased mineralization, thus also contributes to an increase in

1131   GPP over and above that due to a change in climate alone, and therefore compensates for the

1132   amount of carbon lost due to increased soil organic matter decomposition associated with

1133   warmer temperatures. This behaviour is consistent with land C cycle models showing a reduction

1134   in the absolute value of the strength of the carbon-climate feedback when they include coupling

1135   of C and N cycles (Arora et al., 2020).

1136   The modelled differences in PFT specific values of V_{cmax}, in our framework, come through

1137   differences in simulated values of leaf N amount (N_L) that depend on BNF (given that BNF is the

1138   primary natural source of N input into the coupled soil-vegetation system) but also differences

1139   in mineralization that are governed by climate. N_L values, however, also depend on leaf

1140   phenology, allocation of carbon and nitrogen, turnover rates, transpiration (which brings in N

1141   through passive uptake), and almost every aspect of plant biogeochemistry which affects a PFT's

1142   net primary productivity and therefore N demand. Modelled increases in GPP in response to N

1143   deposition come through an increase in leaf N amount and therefore V_{cmax} values.

1144   Finally, changes in land use associated with an increase in crop area, and the associated

1145   increase in fertilizer application rates lead to the largest increase in NO_3^- leaching, NH_3

1146   volatilization, and gaseous losses associated with nitrification and denitrification among all

1147   forcings. Overall, the model response to perturbation by all individual forcings is realistic,

1148   conceptually expected, and of the right sign (positive or negative) although it is difficult to

1149   evaluate the magnitude of these responses in the absence of directly comparable observation-

1150   based estimates.

1151   Despite the model responses to individual forcings that appear consistent with our

1152   conceptual understanding of coupled C and N cycles, our modelling framework misses an

1153   important feedback process that has been observed in the FACE and other experiments related

1154   to changes in natural BNF. FACE sites and other empirical studies report an increase in natural

1155   BNF rates at elevated CO_2 (McGuire et al., 1995; Liang et al., 2016) and a decrease in natural BNF

1156   rates when additional N is applied to soils (Salvagiotti et al., 2008; Ochoa-Hueso et al., 2013). On

1157   a broad scale this is intuitively expected but the biological processes behind changes in BNF rates

1158   remain largely unclear. A response can still be parameterized even if the underlying physical and

1159   biological processes are not well understood. For instance, Goll et al. (2012) parameterize BNF as

1160   an increasing and saturating function of NPP, $BNF = 1.8 \left(1.0 - exp(-0.003\,NPP)\right)$. This

1161   approach, however, does not account for the driver behind the increase in NPP - increasing

1162   atmospheric CO_2, change in environmental conditions (e.g., wetter and warmer conditions), or

1163   increased N deposition. Clearly, increasing BNF if the NPP increase is due to N deposition is

1164   inconsistent with empirical observations. Over the historical period an increase in atmospheric

1165 CO_2 has been associated with an increase in N deposition so to some extent changes in BNF due

1166   to both forcings will cancel each other. We realize the importance of changes in BNF, given it is

1167   the single largest natural flux of N into the coupled soil-vegetation system yet highly uncertain,

1168   and aim to address these issues in a future version of the model by exploring existing BNF

1169   formulations. Meyerholt et al. (2016), for example, demonstrate the uncertainty arising from the

1170   use of five different BNF parameterizations in the context of the O-CN model. They use

1171   formulations that parameterize BNF as a function of 1) evapotranspiration, 2) NPP, 3) leaf C:N

1172   ratio, that takes into account energy cost for N fixation (Fisher et al., 2010), 4) plant N demand,

1173   and 5) an optimality-based approach that follows Rastetter et al. (2001) in which BNF only occurs

1174   when the carbon cost of N fixation is lower than the carbon cost of root N uptake. The approach

1175   used in our study is closest to the one that is based on evapotranspiration but makes the

1176   distinction in BNF rates over natural and agricultural areas.

1177   The reduction of photosynthesis rates in response to N limitation is the most important

1178   linkage between C and N cycles and yet it too is parameterized differently across models. Given

1179   that leaf N amount and photosynthetic capacity are strongly correlated (Evans, 1989; Field and

1180   Mooney, 1986; Garnier et al., 1999), photosynthesis downregulation due to N limitation reduces

1181   photosynthetic capacity, and thus the GPP flux. Yet models reduce both NPP (Wiltshire et al.,

1182   2020) and V_{cmax} rates, and thus GPP, (Zaehle and Friend, 2010; Wania et al., 2012; von Bloh et al.,

1183   2018) in reponse to N limitation. V_{cmax} rates may themselves be parameterized as a function leaf

1184   N amount directly (von Bloh et al., 2018; Zaehle and Friend, 2010) or leaf C:N ratio (Wania et al.,

1185   2012). In this study, we have parameterized V_{cmax} rates as a function of leaf N amount (equation

1186   31) since the use of leaf C:N ratio leads to an incorrect seasonal variation of V_{cmax}. If an increase

1187   in leaf C:N ratio, as a result of increase in atmospheric CO_2, leads to a decrease in V_{cmax} rates over

1188   the historical period then it implies that V_{cmax} is inversely related to leaf C:N ratios. Since leaf C:N

1189   ratio peak during the growing season (Li et al., 2017) this also implies V_{cmax} rates are lower during

1190   the peak growing season than at its start and this is in contrast to observations that show an

1191   increase in V_{cmax} during the growing season (e.g., see Fig. 1a of Bauerle et al. (2012)).

1192   Our framework assumes a constant C:N ratio of 13 for soil organic matter ($C:N_H$), an

1193   assumption also made in other models (e.g., Wania et al., 2012; Zhang et al., 2018). This

1194   assumption is also broadly consistent with Zhao et al. (2019) who attempt to model C:N of soil

1195   organic matter, among other soil properties, as a function of mean annual temperature and

1196   precipitation using machine learning algorithms (their Figure 2h). It is difficult to currently

1197   establish if increasing atmospheric CO_2 is changing $C:N_H$ given the large heterogeneity in soil

1198   organic C and N densities, and the difficulty in measuring small trends for such large global pools.

1199 A choice of a somewhat different value for all PFTs or had we chosen specified constant PFT-

1200 dependent values of $C:N_H$ is of relatively less importance in this context since the model is spun

1201 to equilibrium for 1850 conditions anyway. It is the change in $C:N_H$ over time that is of

1202 importance. The assumption of constant $C:N_H$ is the key to yielding a decrease in vegetation N

1203 mass, and therefore leaf N mass and V_{cmax}, as CO_2 increases, in our framework. Without a

1204 decrease in V_{cmax} in our modelling framework, in response to elevated CO_2, we cannot achieve

1205 the downregulation noted by McGuire et al. (1995) in their meta-analysis, and the simulated

1206 carbon sink over the historical period would be greater than observed as noted above. It is

1207 possible that we are simulating the reduction in leaf N mass, in response to elevated CO_2, for a

1208 wrong reason in which case our model processes need to be revisited based on additional

1209 empirical data. If our assumption of constant or extremely slowly changing $C:N_H$ is indeed

1210 severely unrealistic, this necessitates a point of caution that a realistic land carbon sink can be

1211 simulated over the historical period with such an assumption.

1212 Related to this assumption is also the fact that we cannot make decomposition rates of

1213 soil organic matter a function of its C:N ratio since it is assumed to be a constant. It is well known

1214 that after climate, litter and soil organic matter decomposition rates are controlled by their C:N

1215 ratio (Manzoni et al., 2008). Litter decomposition rates can still be made a function of its C:N ratio

1216 and we aim to do this for a future model version.

1217 The work presented in this study of coupling C and N cycles in CLASSIC yields a framework

1218 that we can build upon to make model processes more realistic, test the effect of various model

1219 assumptions, parameterize existing processes in other ways, include additional processes, and

1220 evaluate model response at FluxNet sites to constrain model parameters.

Appendix

1221

1222

1223 **A1. Budget equations for N pools**

1224 The rates of change of N in the NH_4^+ and NO_3^- pools (in gN m^{-2}), N_{NH4} and N_{NO3},

1225 respectively, are given by

1227
$$\frac{d\,N_{NH4}}{dt} = B_{NH4} + F_{NH4} + P_{NH4} + M_{D,NH4} + M_{H,NH4}$$

1226
$$-U_{NH4} - (I_{NO3} + I_{N2O} + I_{NO}) - V_{NH3} - O_{NH4} \tag{A1}$$

1228
$$\frac{d\,N_{NO3}}{dt} = P_{NO3} + I_{NO3} - L_{NO3} - U_{NO3} - (E_{N2} + E_{N2O} + E_{NO}) - O_{NO3} \tag{A2}$$

1229 and all fluxes are represented in units of gN m^{-2} day^{-1}. B_{NH4} is the rate of biological N fixation

1230 which solely contributes to the NH_4^+ pool, F_{NH4} is the fertilizer input which is assumed to

1231 contribute only to the NH_4^+ pool, and P_{NH4} and P_{NO3} are atmospheric deposition rates that

1232 contribute to the NH_4^+ and NO_3^- pools, respectively. Biological N fixation, fertilizer input, and

1233 atmospheric deposition are the three routes through which N enters the coupled soil-vegetation

1234 system. $M_{D,NH4}$ and $M_{H,NH4}$ are the mineralization flux from the litter and soil organic matter

1235 pools, respectively, associated with their decomposition. We assume mineralization of humus

1236 and litter pools only contributes to the NH_4^+ pool. O_{NH4} and O_{NO3} indicate immobilization of N

1237 from the NH_4^+ and NO_3^- pools, respectively, to the humus N pool which implies microbes (that

1238 are not represented explicitly) are part of the humus pool. Combined together the terms

1239 $(M_{D,NH4} + M_{H,NH4} - O_{NH4} - O_{NO3})$ yield the net mineralization rate. V_{NH3} is the rate of

1240 ammonia (NH_3) volatilization and L_{NO3} is the leaching of N that occurs only from the NO_3^- pool.

1241 The positively charged ammonium ions are attracted to the negatively charged soil particles and

1242 as a result it is primarily the negatively charged nitrate ions that leach through the soil (Porporato

1243 et al., 2003; Xu-Ri and Prentice, 2008). U_{NH4} and U_{NO3} are uptakes of NH_4^+ and NO_3^- by plants,

1244 respectively. The nitrification flux from NH_4^+ to NO_3^- pool is represented by I_{NO3} which also results

1245 in the release of the nitrous oxide (N_2O), a greenhouse gas, and nitric oxide (NO) through nitrifier

1246 denitrification represented by the terms I_{N2O} and I_{NO}, respectively. Finally, E_{N2}, E_{N2O}, and E_{NO}

1247 are the gaseous losses of N_2 (nitrogen gas), N_2O, and NO from the NO_3^- pool associated with

1248 denitrification. N is thus lost through the soil-vegetation system via leaching in runoff and

1249 through gaseous losses of I_{N2O}, I_{NO}, E_{N2}, E_{N2O}, E_{NO}, and V_{NH3}.

1250   The structural and non-structural N pools in root are written as $N_{R,S}$ and $N_{R,NS}$,

1251 respectively, and similarly for stem ($N_{S,S}$ and $N_{S,NS}$) and leaves ($N_{L,S}$ and $N_{L,NS}$), and together the

1252 structural and non-structural pools make the total N pool in leaf ($N_L = N_{L,S} + N_{L,NS}$), root ($N_R =$

1253 $N_{R,S} + N_{R,NS}$), and stem ($N_S = N_{S,S} + N_{S,NS}$) components. The rate change equation for

1254 structural and non-structural N pools in root are given by

1255
$$\frac{d\,N_{R,NS}}{dt} = U_{NH4} + U_{NO3} + R_{L2R} - R_{R2L} - A_{R2L} - A_{R2S} - LF_{R,NS} - T_{R,NS2S} \qquad \text{(A3)}$$

1256
$$\frac{d\,N_{R,S}}{dt} = T_{R,NS2S} - LF_{R,S} \qquad \text{(A4)}$$

1257 Similar to the uptake of carbon by leaves and its subsequent allocation to root and stem

1258 components, N is taken up by roots and then allocated to leaves and stem. A_{R2L} and A_{R2S}

1259 represent the allocation of N from roots to leaves and stem, respectively. The terms R_{L2R} and

1260 R_{R2L} represent the reallocation of N between the non-structural components of root and leaves.

1261 R_{L2R} is the N reallocated from leaves to root representing resorption of a fraction of leaf N during

1262   leaf fall for deciduous tree PFTs. R_{R2L} indicates reallocation of N from roots to leaves (termed

1263   reallocation in Figure 2) at the time of leaf-out for deciduous tree PFTs. At times other than leaf-

1264   out and leaf-fall and for other PFTs these two terms are zero. $T_{R,NS2S}$ is the one way transfer of

1265   N from the non-structural to the structural root pool, and similar to the carbon pools, once N is

1266   converted to its structural form it cannot be converted back to its non-structural form. Finally,

1267   the litterfall due to turnover of roots occurs from both the structural ($LF_{R,S}$) and non-structural

1268   ($LF_{R,NS}$) N pools.

1269   The rate change equations for non-structural and structural components of leaves are

1270   written as

1271
$$\frac{d\,N_{L,NS}}{dt} = A_{R2L} - R_{L2R} - R_{L2S} + R_{R2L} + R_{S2L} - LF_{L,NS} - T_{L,NS2S} \tag{A5}$$

1272
$$\frac{d\,N_{L,S}}{dt} = T_{L,NS2S} - LF_{L,S} \tag{A6}$$

1273   where $T_{L,NS2S}$ is the one way transfer of N from the non-structural leaf component to its

1274   structural N pool and R_{S2L} indicates reallocation of N from stem to leaves (similar to R_{R2L}) at the

1275   time of leaf out for deciduous tree PFTs. Litterfall occurs from both the structural ($LF_{L,S}$) and non-

1276   structural ($LF_{L,NS}$) N pools of leaves, and all other terms have been previously defined.

1277   Finally, the rate change equations for non-structural and structural components of stem

1278   are written as

1279
$$\frac{d\,N_{S,NS}}{dt} = A_{R2S} + R_{L2S} - R_{S2L} - LF_{S,NS} - T_{S,NS2S} \tag{A7}$$

1280
$$\frac{d\,N_{S,S}}{dt} = T_{S,NS2S} - LF_{S,S} \tag{A8}$$

1281 where $LF_{S,NS}$ and $LF_{S,S}$ represent stem litter from the non-structural and structural components,

1282 $T_{S,NS2S}$ is the one way transfer of N from the non-structural stem component to its structural N

1283 pool. All other terms have been previously defined.

1284   Adding equations (6) through (11) yields rate of change of N in the entire vegetation pool

1285 (N_V) as

$$\frac{d\,N_V}{dt} = \frac{d\,N_{R,NS}}{dt} + \frac{d\,N_{R,S}}{dt} + \frac{d\,N_{L,NS}}{dt} + \frac{d\,N_{L,S}}{dt} + \frac{d\,N_{S,NS}}{dt} + \frac{d\,N_{S,S}}{dt} = \frac{d\,N_R}{dt} + \frac{d\,N_L}{dt} + \frac{d\,N_S}{dt}$$

1286   (A9)

$$\begin{aligned}\frac{d\,N_V}{dt} &= U_{NH4} + U_{NO3} - LF_{R,NS} - LF_{R,S} - LF_{L,NS} - LF_{L,S} - LF_{S,NS} - LF_{S,S}\\ &= U_{NH4} + U_{NO3} - LF_R \qquad\qquad - LF_L \qquad\qquad - LF_S\end{aligned}$$

1287 which indicates how the dynamically varying vegetation N pool is governed by mineral N uptake

1288 from the NH_4^+ and NO_3^- pools and litterfall from the structural and non-structural components of

1289 the leaves, stem, and root pools. LF_R is the total N litter generation from the root pool and sum

1290 of litter generation from its structural and non-structural components ($LF_R = LF_{R,S} + LF_{R,NS}$),

1291 and similarly for the leaves (LF_L) and the stem (LF_S) pools.

1292   The rate change equations for the organic N pools in the litter (N_D) and soil (N_H) pools

1293 are written as follows.

1294 $$\frac{d\,N_D}{dt} = LF_R + LF_L + LF_S - H_{N,D2H} - M_{D,NH4} \qquad\qquad (A10)$$

1295 $$\frac{d\,N_H}{dt} = H_{N,D2H} + O_{NH4} + O_{NO3} - M_{H,NH4} \qquad\qquad (A11)$$

1296 where $H_{N,D2H}$ is the transfer of humidified organic matter from litter to the soil organic matter

1297 pool, and all other terms have been previously defined.

1298

1299

Acknowledgments

1301 We are grateful and thank Joe Melton and Paul Bartlett for their comments on an earlier version
1302 of this manuscript. We are grateful to one anonymous reviewer, and David Wårlind, for their
1303 reviewer comments which greatly improved this manuscript. We also gratefully acknowledge
1304 Sönke Zaehle, the handling editor for this paper, for his time and effort.

1305

Code/Data availability

1307 Model code for the operational CLASSIC model can be obtained from
1308 https://gitlab.com/cccma/classic. Changes made to the operational version to include N cycle
1309 and the results shown here can be obtained from the second author.

1310

Author contributions

1312 A.A. implemented the N cycle in the CLASSIC code, put together all the N cycle related input
1313 data, and performed all the simulations. V.A. and A.A. wrote the manuscript.

1314

Competing interests

1316 There are no competing interests.

1317

1318

1319
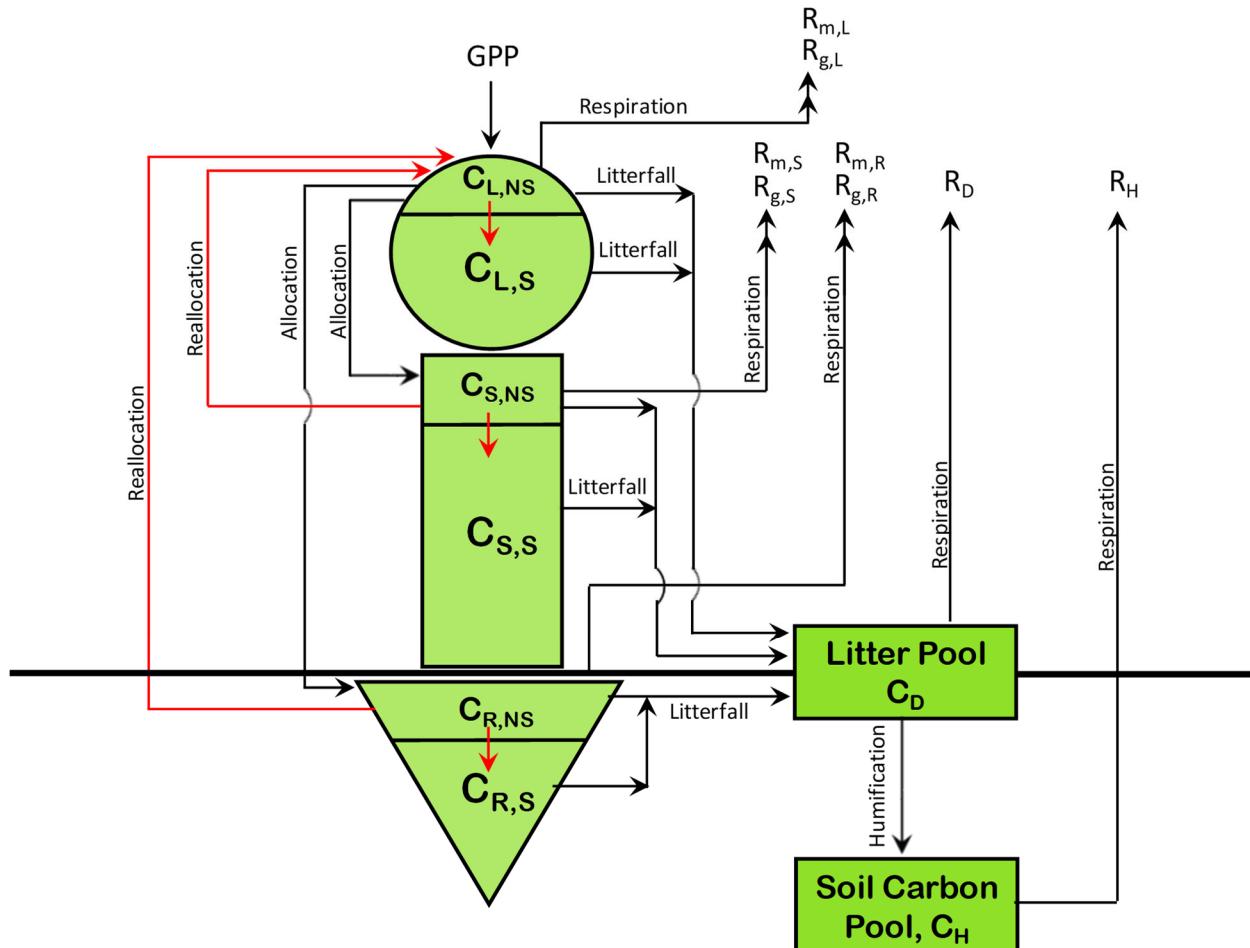
1320

1321

1322   Figure A1: The structure of CLASSIC model used in this study, upon which the N cycle is
1323   implemented, with its carbon pools and fluxes. The fluxes of non-structural carbon are shown in
1324   red colour.

1325

1326

1327

1328

1329

1330
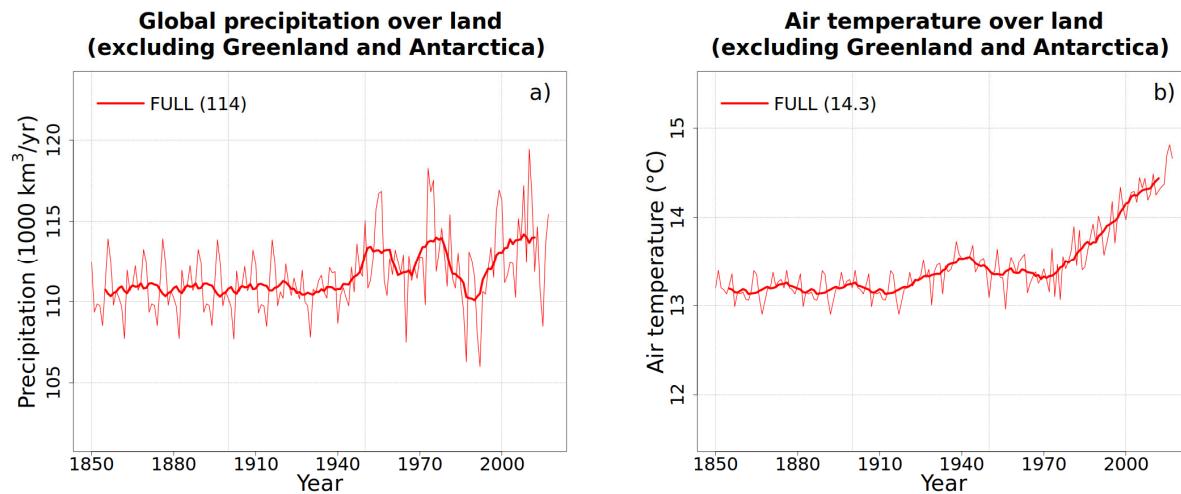
1331

1332

1333   Figure A2: Annual values of global precipitation (a) and air temperature (b) over land in the
1334   CRU-JRA reanalysis data that are used to drive the model. The data are available for the period
1335   1901-2017. In the absence of meteorological data for the period 1851-1900, data from the
1336   period 1901-1925 are used twice. The thin lines are the annual values and the thick line their 10
1337   year running mean. The values in the brackets in the legend show average values over the last
1338   20 years.

1339

1340 **Table A1**: Model parameters for various model parameterizations. Corresponding equation in which the
1341 parameter appears in the main text is also noted. Model parameters may be scalar or an array (if they
1342 are PFT dependent) in which case they are written according to the following structure in the table
1343 below.

Needleleaf evergreen	Needleleaf deciduous	
Broadleaf evergreen	Broadleaf deciduous cold	Broadleaf deciduous drought
C_3 crop	C_4 crop	
C_3 grass	C_4 grass	

1344 .

Model parameter	Eqn	Description	Units	Value(s)		
Biological N fixation						
α_c	3	BNF rate for crop PFTs	gN m^{-2} day^{-1}	0.00217		
α_n	3	BNF rate for natural PFTs	gN m^{-2} day^{-1}	0.00037		
Plant N demand						
$C{:}N_{L,min}$	4	Minimum C:N ratio for leaves	dimensionless	25 20 16 13	22 18 20 18	18
$C{:}N_{S,min}$	4	Minimum C:N ratio for stem	dimensionless	450 430 285 –	450 430 285 –	430
$C{:}N_{R,min}$	4	Minimum C:N ratio for root	dimensionless	45 35 30 30	45 35 35 35	35
Plant uptake						
β	6	Mineral N distribution coefficient	dimensionless	0.5		
ε	8	Fine root efficiency	gN gC^{-1} day^{-1}	4.92E-5		
$k_{p,\frac{1}{2}}$	8	Half saturation constant	gN m^{-3}	3		
Litterfall						
r_L	11	Leaf resorption coefficient	dimensionless	0.54		
Nitrification						
η	19	Nitrification coefficient	day^{-1}	7.33E-4		

Symbol	Eq.	Description	Units	Value
η_{NO}	23	Fraction of nitrification flux emitted as NO	dimensionless	7.03E-5
η_{N2O}	23	Fraction of nitrification flux emitted as N_2O	dimensionless	2.57E-5
Denitrification				
μ_{NO}	24	Fraction of denitrification flux emitted as NO	day^{-1}	3.872E-4
μ_{N2O}	24	Fraction of denitrification flux emitted as N_2O	day^{-1}	1.408E-4
μ_{N2}	24	Fraction of denitrification flux emitted as N_2	day^{-1}	3.872E-3
w_d	24	Soil wetness threshold below which very little denitrification occurs	dimensionless	0.3
Leaching				
φ	26	Leaching coefficient	$m^2 \, Kg^{-1}$	1.15E-3
NH₃ volatilization				
ϑ	27	NH₃ volatilization coefficient	dimensionless	0.54
Coupling of C and N cycles				
Γ_1	31	Parameter for calculating V_{cmax} from leaf N amount	$\mu mol \, CO_2 \, gN^{-1} \, s^{-1}$	39 (all PFTs except broadleaf evergreen tree) 15.3 (for broadleaf evergreen tree)
Γ_2	31	Parameter for calculating V_{cmax} from leaf N amount	$\mu mol \, CO_2 \, m^{-2} \, s^{-1}$	8.5
k_Λ	32	Parameter for constraining V_{cmax} increase when C:N ratios exceed their maximum limit	dimensionless	0.05
$C:N_{L,max}$	33	Maximum C:N ratio for leaves	dimensionless	60 50 55 40 40 40 50 35 50
$C:N_{S,max}$	33	Maximum C:N ratio for stem	dimensionless	800 800 670 670 670 500 500

				–	–		
$C{:}N_{R,max}$	33	Maximum C:N ratio for root	dimensionless	90 70 60 60	90 70 70 70	70	

1345

1346

1347 **Table 1**: Historical simulations performed over the period 1851-2017 to evaluate the model's
1348 response to various forcings. All forcings are time varying. All forcings are also spatially explicit
1349 except atmospheric CO_2 for which a globally constant value is specified.

1350

Simulation name	Forcing that varies over the historical period	N cycle
Primary simulations performed to evaluate N cycle response to various forcings		
1. CO2-only	Atmospheric CO_2 concentration	Runs with N cycle
2. CLIM-only	1901-1925 meteorological data are used twice over the 1850-1900 period. For the 1901-2017 period, meteorological data for the correct year is used.	
3. LUC+FERT-only	Land cover with increasing crop area, and fertilizer application rates over the crop area	
4. N-DEP-only	N deposition of ammonia and nitrate	
5. FULL	All forcings	
6. FULL-no-LUC	All forcings except increasing crop area	

Other simulations		
7. ORIGINAL	All forcings	Runs without N cycle using the original model configuration.
8. ORIG-UNCONST	All forcings but with downregulation turned off	
9. FULL-no-implicit-P-limitation	All forcings but using same Γ_1 and Γ_2 globally	Run with N cycle

1351

1352

1353

1354   **Table 2**: Comparison of simulated global N pools and fluxes, from the FULL simulation, with other
1355   modelling and quasi observation-based studies (references for which are noted as superscripts
1356   and listed below the table). The time-periods to which the other modelling and quasi
1357   observation-based estimates correspond are also noted, where available. The estimates are for
1358   land. Simulated fluxes and pool corresponds to the period 1997-2018.

1359

N pool and fluxes	This study (1998-2017)	Other model and quasi observation-based estimates	
N inputs (Tg N yr^{-1})			
BNF	119	118	Fowler et al. (2013)
		99 (2001-2010)	Zaehle (2013)
		138.5 (early 1990s)	Galloway et al. (2004)
		128.9 (2000-2009)	von Bloh et al. (2018)
		104-118	Galloway et al. (2013)
		92 (year 2000)	Bouwman et al. (2013)
Natural BNF	59	58	Fowler et al. (2013)
		107 (early 1990s)	Galloway et al. (2004)
		30-130	Galloway et al. (2013)
		39 (year 2000)	Bouwman et al. (2013)
Anthropogenic BNF	60	60	Fowler et al. (2013)
		31.5 (early 1990s)	Galloway et al. (2004)
		14-89	Galloway et al. (2013)
		53 (year 2000)	Bouwman et al. (2013)
Fertilizer input	91 (based on the TRENDY protocol)	100	Fowler et al. (2013)
		100 (2001-2010)	Zaehle (2013)
		100 (early 1990s)	Galloway et al. (2004)
		83 (year 2000)	Bouwman et al. (2013)
N deposition	66 (based on the TRENDY protocol)	70	Fowler et al. (2013)
		56-62	Zaehle (2013)
		63.5 (early 1990s)	Galloway et al. (2004)
		69 (year 2000)	Bouwman et al. (2013)
N pools (Tg N yr^{-1})			
Vegetation	3034	1,780 (2000s)	von Bloh et al. (2018)
		3,800 (1990s)	Zaehle et al. (2010)
		5,300	Xu-Ri and Prentice (2008)
		2,940 (1990s)	Wania et al. (2012)
Litter and soil	77161	106,000 (2000s)	von Bloh et al. (2018)
		100,000 (1990s)	Zaehle et al. (2010)
		56,800	Xu-Ri and Prentice (2008)
		113,000 (1990s)	Wania et al. (2012)
Ammonia	1924	163.7 (2000s)	von Bloh et al. (2018)
		361	Xu-Ri and Prentice (2008)
		1200 (1990s)	Wania et al. (2012)
Nitrate	2974	2,778 (2000s)	von Bloh et al. (2018)
		580	Xu-Ri and Prentice (2008)
		14,800 (1990s)	Wania et al. (2012)

N fluxes related to N cycling (Tg N yr^{-1})				
Plant uptake	940		618 (2000s)	von Bloh et al. (2018)
			1,127 (1990s)	Zaehle et al. (2010)
			1,084	Xu-Ri and Prentice (2008)
			873 (1990s)	Wania et al. (2012)
Net mineralization	947			
Mineralization	2045		1,678 (2000s)	von Bloh et al. (2018)
Immobilization	1097		1,177 (2000s)	von Bloh et al. (2018)
Nitrification	239			
N losses (Tg N yr^{-1})				
NO$_3$- Leaching	53.5		97.1 (2001-2010)	Zaehle (2013)
			62.8 (2000s)	von Bloh et al. (2018)
			77.0 (1990s)	Zaehle et al. (2010)
NH$_3$ Volatilization	53.9		124.9 (2001-2010)	Zaehle (2013)
			52.6 (early 1990s)	Galloway et al. (2004)
			20.4 (2000s)	von Bloh et al. (2018)
N$_2$ from denitrification	114.2		105.8 (2001-2010)	Zaehle (2013)
			68 (year 2000)	Bouwman et al. (2013)
N$_2$O from denitrification	4.2	12.6	8.7 (2001-2010)	Zaehle (2013)
N$_2$O from nitrification	8.4		10.9 (early 1990s)	Galloway et al. (2004)
			13.0	Fowler et al. (2013)
NO from denitrification	11.4	34.3	24.8 (early 1990s)	Galloway et al. (2004)
NO from nitrification	22.9		26.8 (1990s)	Zaehle et al. (2010)

1360

1361

1362

1363
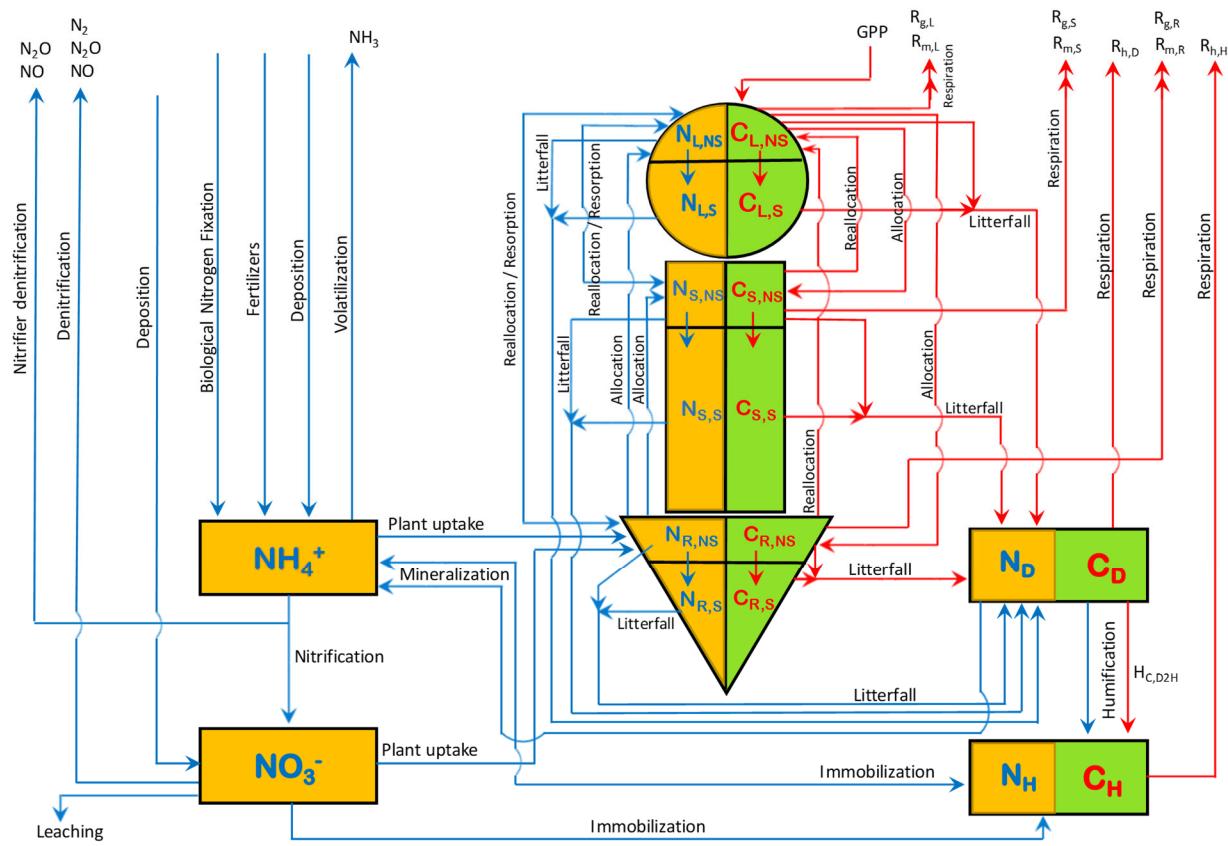
1364

Figure 1: The structure of CLASSIC model used in this study. The eight prognostic carbon pools
are shown in green colour and carbon fluxes in red colour. The ten prognostic nitrogen pools are
shown in orange colour and nitrogen fluxes are shown in blue colour.

1368

1369
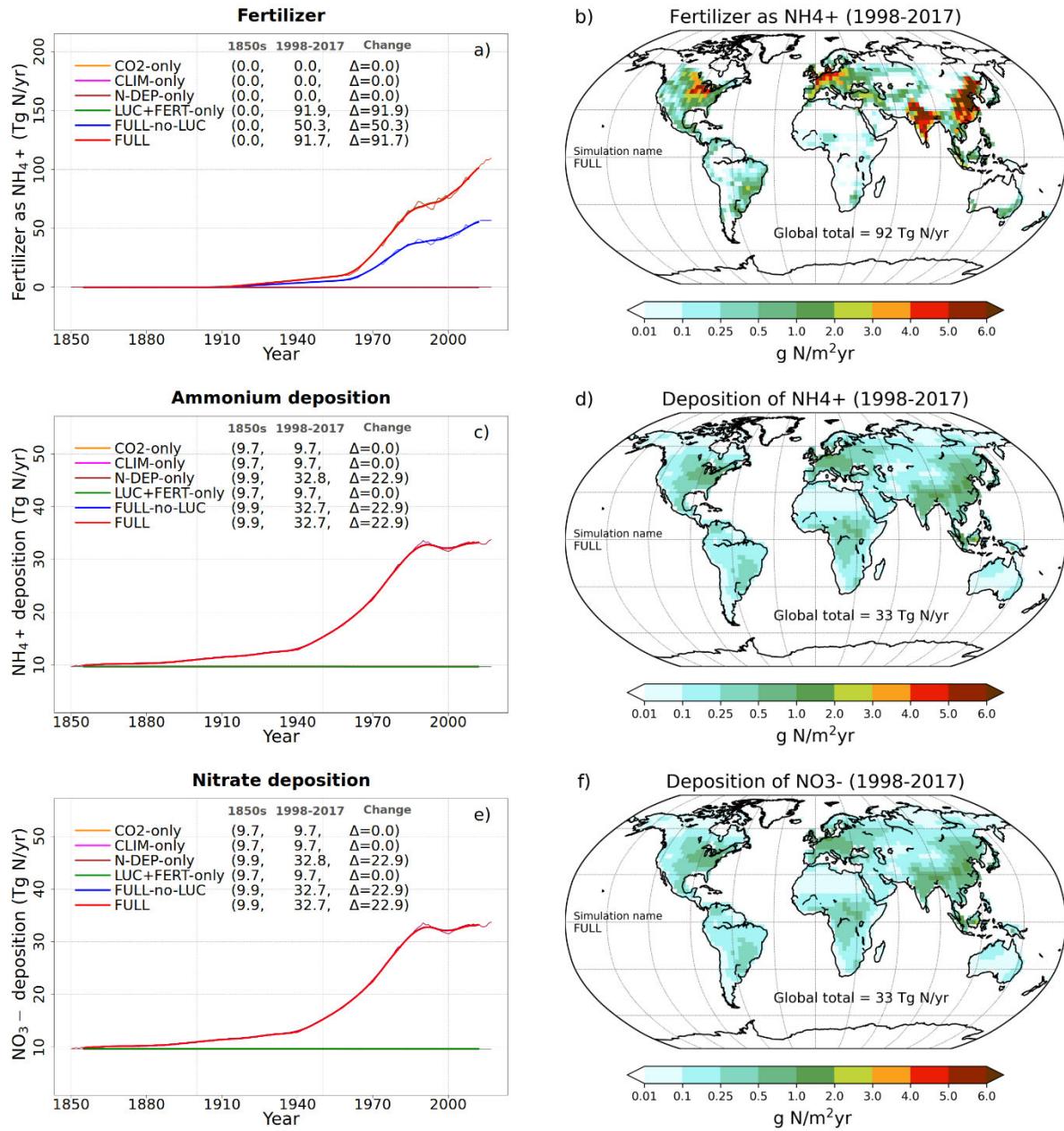
Figure 2: Time series and geographical distribution of global annual values of externally specified N inputs. Fertilizer input (a, b), atmospheric deposition of ammonium (c, d) and atmospheric deposition of nitrate (e, f). The values in the parenthesis for legend entries in the time series plots show averages for the 1850s, the 1998-2017 period, and the change between these two periods. The thin lines in the time series plots show the annual values and the thick lines their 10-year moving average. The geographical plots show the average values over the last 20-years of the FULL simulation corresponding to the 1998-2017 period. Note that in the time series plots lines from some simulations are hidden behind lines from other simulations and this can be inferred from the legend entries which shows averages for the 1850s, the 1998-2017 period.
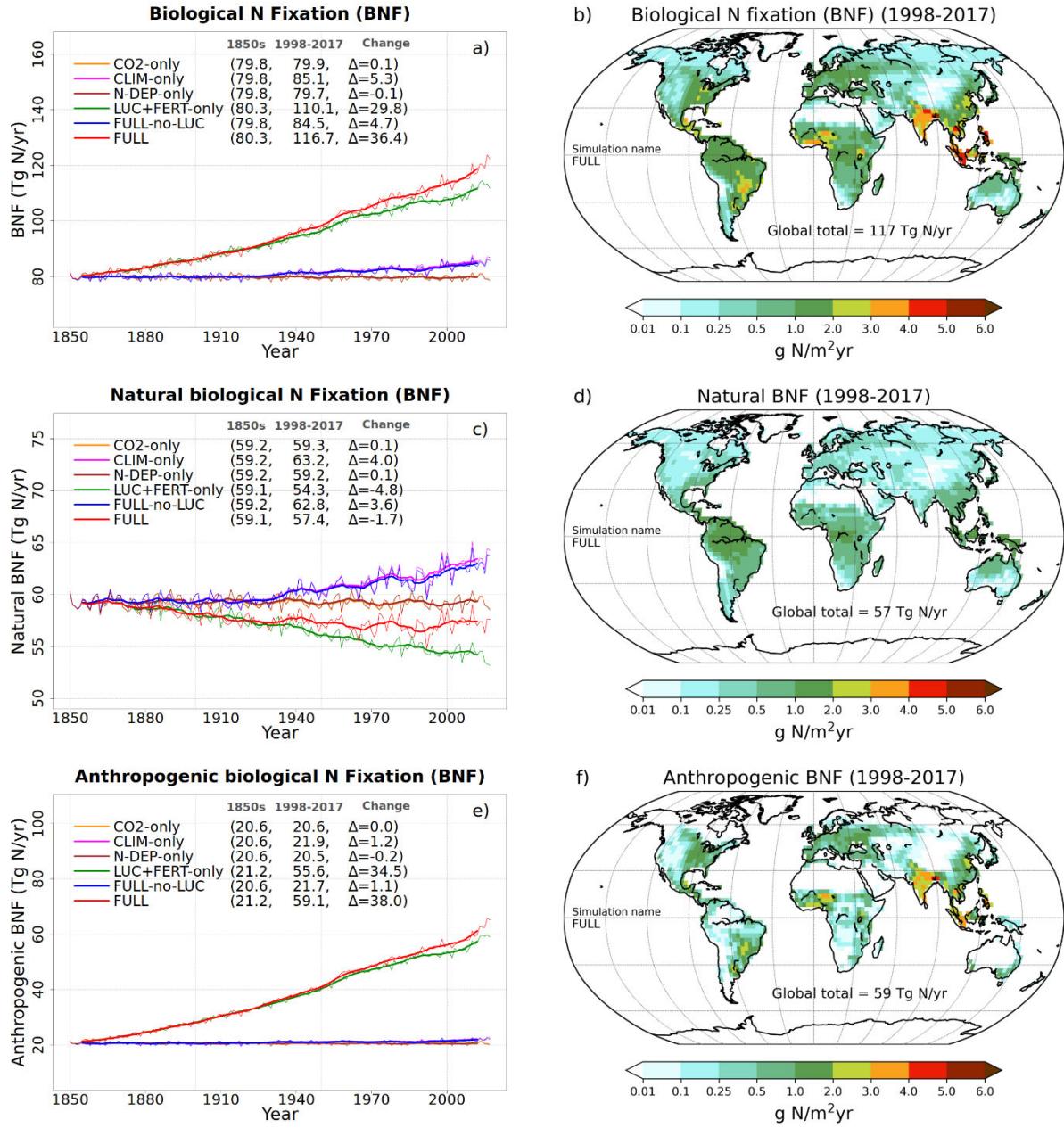
1379

1380 Figure 3: Time series and geographical distribution of annual values biological N fixation (BNF)
1381 (a,b) and its natural (c, d) and anthropogenic (e, f) components. The values in the parenthesis for
1382 legend entries in the time series plots show averages for the 1850s, the 1998-2017 period, and
1383 the change between these two periods. The thin lines in the time series plots show the annual
1384 values and the thick lines their 10-year moving average. The geographical plots show the average
1385 values over the last 20-years of the FULL simulation corresponding to the 1998-2017 period. Note
1386 that in the time series plots lines from some simulations are hidden behind lines from other
1387 simulations and this can be inferred from the legend entries which shows averages for the 1850s,
1388 the 1998-2017 period.

1389

1390
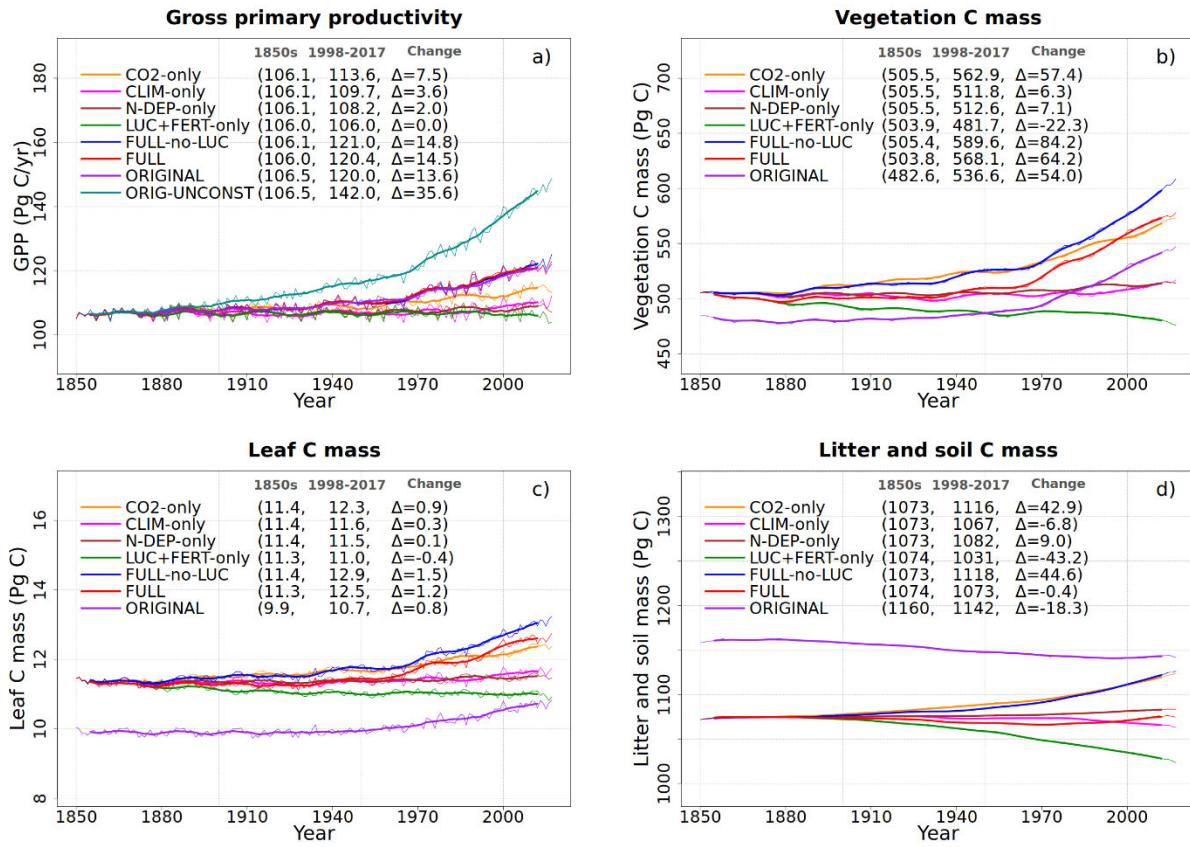
1391   Figure 4: Global annual values of gross primary productivity (a), vegetation carbon (b), leaf
1392   carbon (c), and litter and soil carbon (d) for the primary simulations performed. The values in
1393   the parenthesis for legend entries show averages for the 1850s, the 1998-2017 period, and the
1394   change between 1850s and 1998-2017 periods. The thin lines show the annual values and the
1395   thick lines their 10-year moving average.

1396
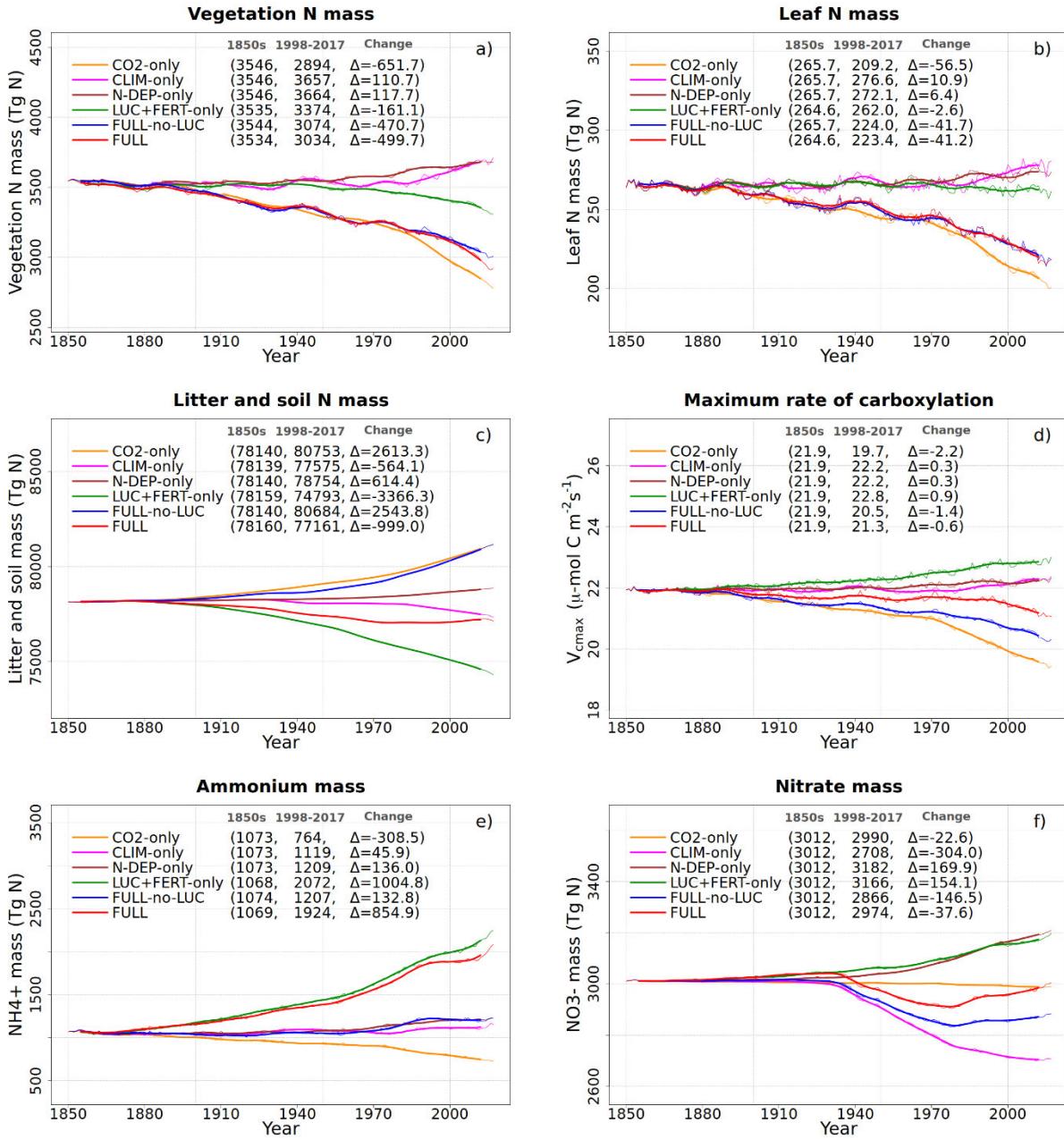
1397

Figure 5: Global annual values of N in vegetation (a), leaves (b), litter and soil organic matter (c)
pools, V_{cmax} (d), and ammonium (e), and nitrate (f) pools for the primary simulations performed.
The values in the parenthesis for legend entries show averages for the 1850s, the 1998-2017
period, and the change between 1850s and 1998-2017 periods. The thin lines show the annual
values and the thick lines their 10-year moving average.

1403
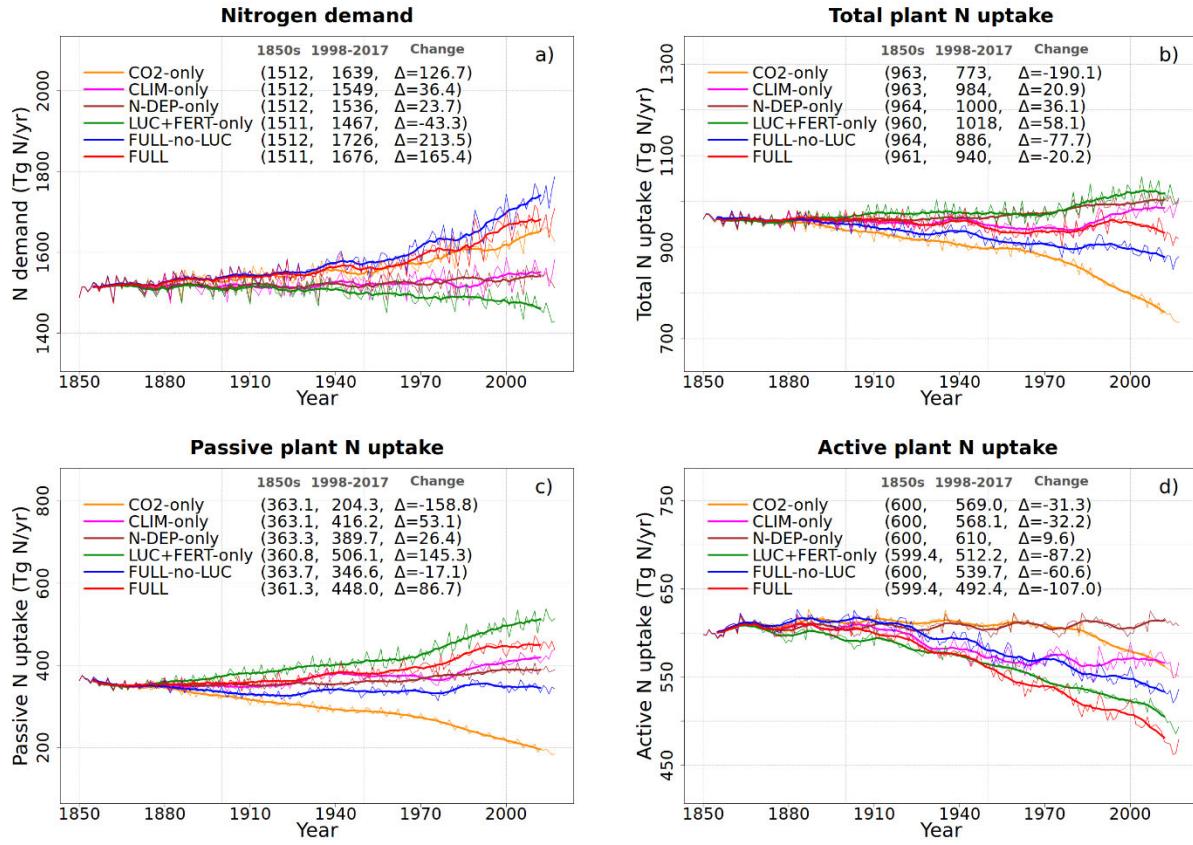
1404

1405

1406 Figure 6: Global annual values of N demand (a), total plant N uptake (b) and its split into passive
1407 (c) and active (d) components for the primary simulations performed. The values in the
1408 parenthesis for legend entries show averages for the 1850s, the 1998-2017 period, and the
1409 change between 1850s and 1998-2017 periods. The thin lines show the annual values and the
1410 thick lines their 10-year moving average.

1411

1412

1413

1414
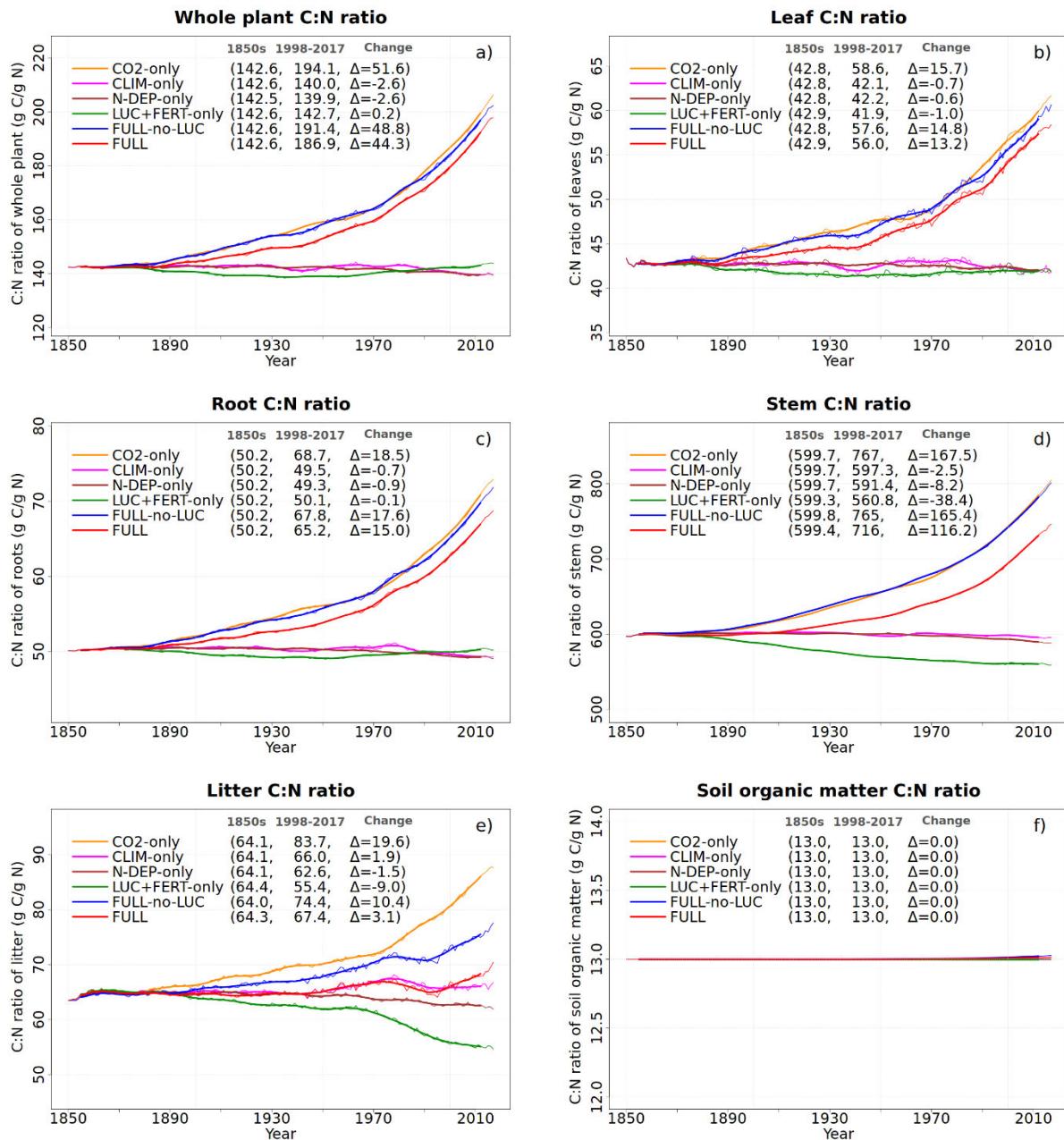
Figure 7: Global annual values of C:N ratios for whole plant (a), leaves (b) , root (c), stem (d), litter (e) and soil organic matter (f) pools from the primary six simulations. The values in the parenthesis for legend entries show averages for the 1850s, the 1998-2017 period, and the change between 1850s and 1998-2017 periods. The thin lines show the annual values and the thick lines their 10-year moving average.

1415
1416
1417
1418
1419

1420

1421

1422
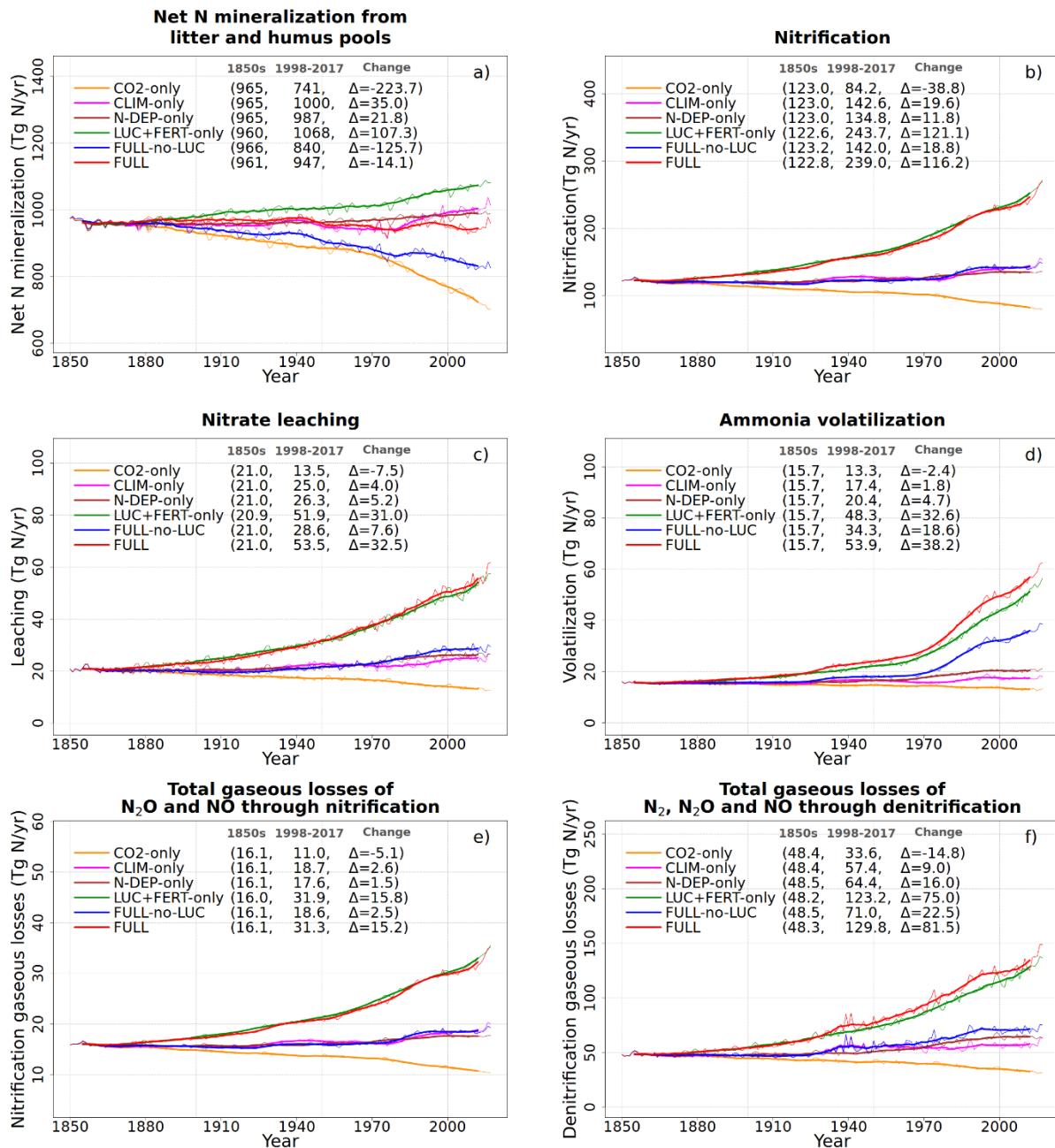
1423 Figure 8: Global annual values of net mineralization (a), nitrification (b), NO_3- leaching (c), NH_3
1424 volatilization (d), and gaseous losses associated with nitrification (e) and denitrification (f) from
1425 the primary six simulations. The values in the parenthesis for legend entries show averages for
1426 the 1850s, the 1998-2017 period, and the change between 1850s and 1998-2017 periods. The
1427 thin lines show the annual values and the thick lines their 10-year moving average.

1428
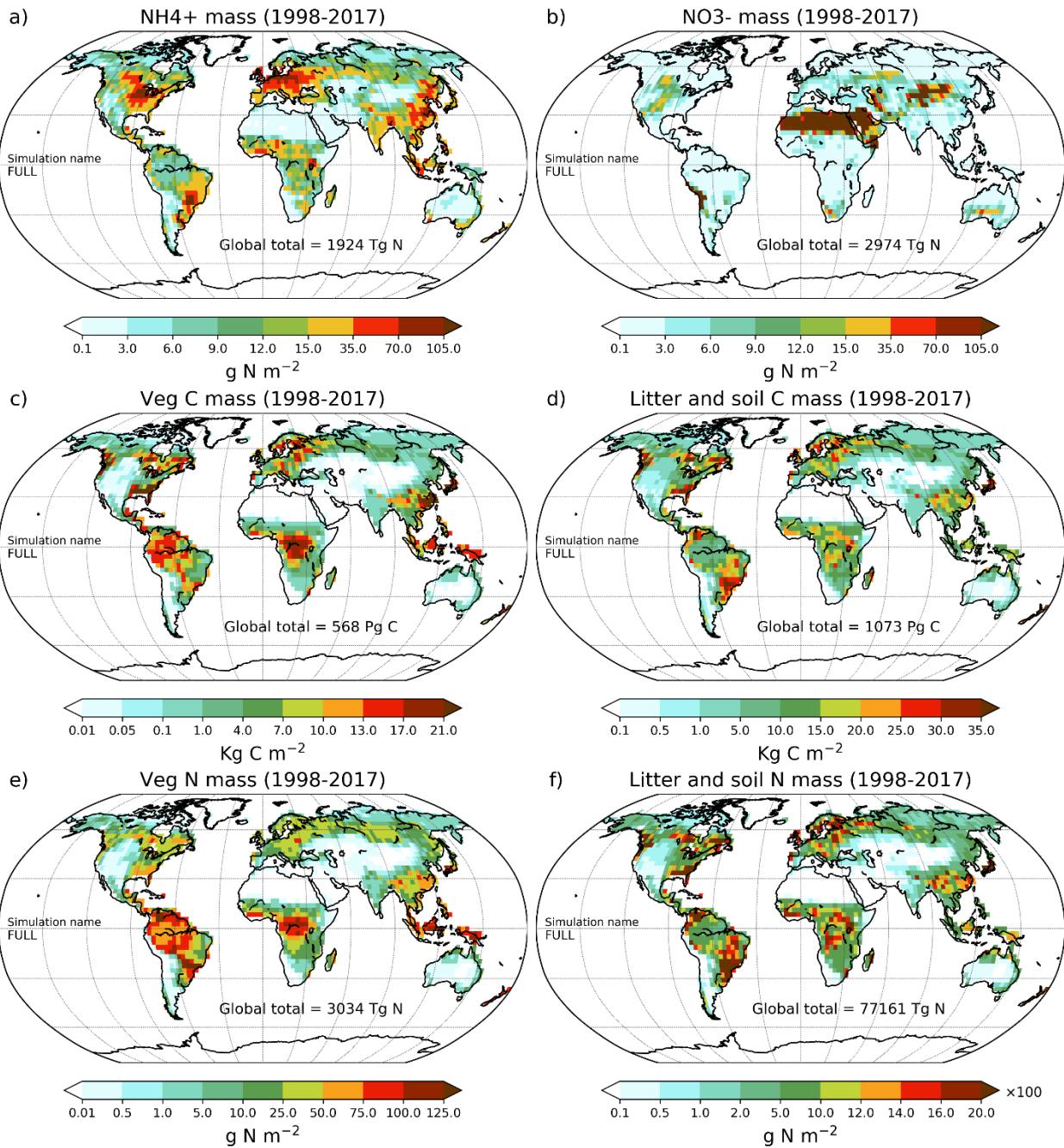
1429

1430   Figure 9: Geographical distribution of primary C and N pools. Ammonium (a), nitrate (b),

1431   vegetation C mass (c), litter and soil C mass (d), vegetation N mass (e), and litter and soil N mass

1432   (f). The global total values shown are averaged over the 1998-2017 period.

1433

1434
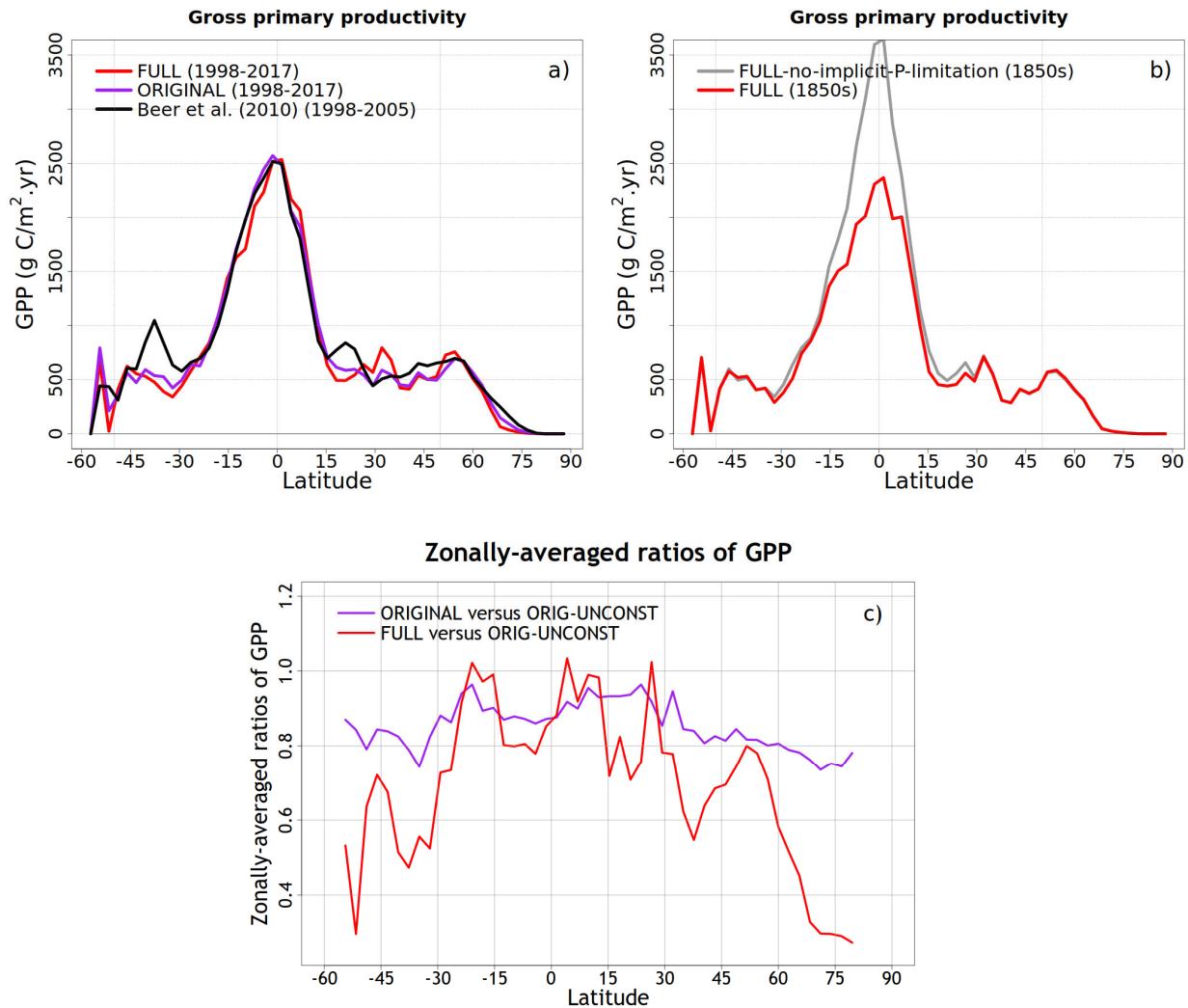
1435

1436 Figure 10: Comparison of zonal distribution of gross primary productivity (GPP) and the effect of
1437 GPP downregulation compared to the ORIG-UNCONST simulation. Panel (a) compares zonal
1438 distribution of GPP from FULL and ORIGINAL simulations with observation-based estimate from
1439 Beer at al. (2010) for the present day. Panel (b) compares the zonal distribution of GPP from the
1440 pre-industrial simulation, corresponding to 1850 conditions, from the FULL and FULL-no-
1441 implicit-P-limitation simulations to illustrate the effect of not reducing the Γ_1 parameter for
1442 calculating V_{cmax} for the broadleaf evergreen tree PFT that implicitly accounts for phosphorus
1443 limitation. Panel (c) shows the zonally-averaged ratios of GPP from the ORIGINAL and FULL
1444 simulations versus those from the ORIG-UNCONST simulations to illustrate how downregulation
1445 acts in the ORIGINAL and FULL simulations.

1446

1447

1448
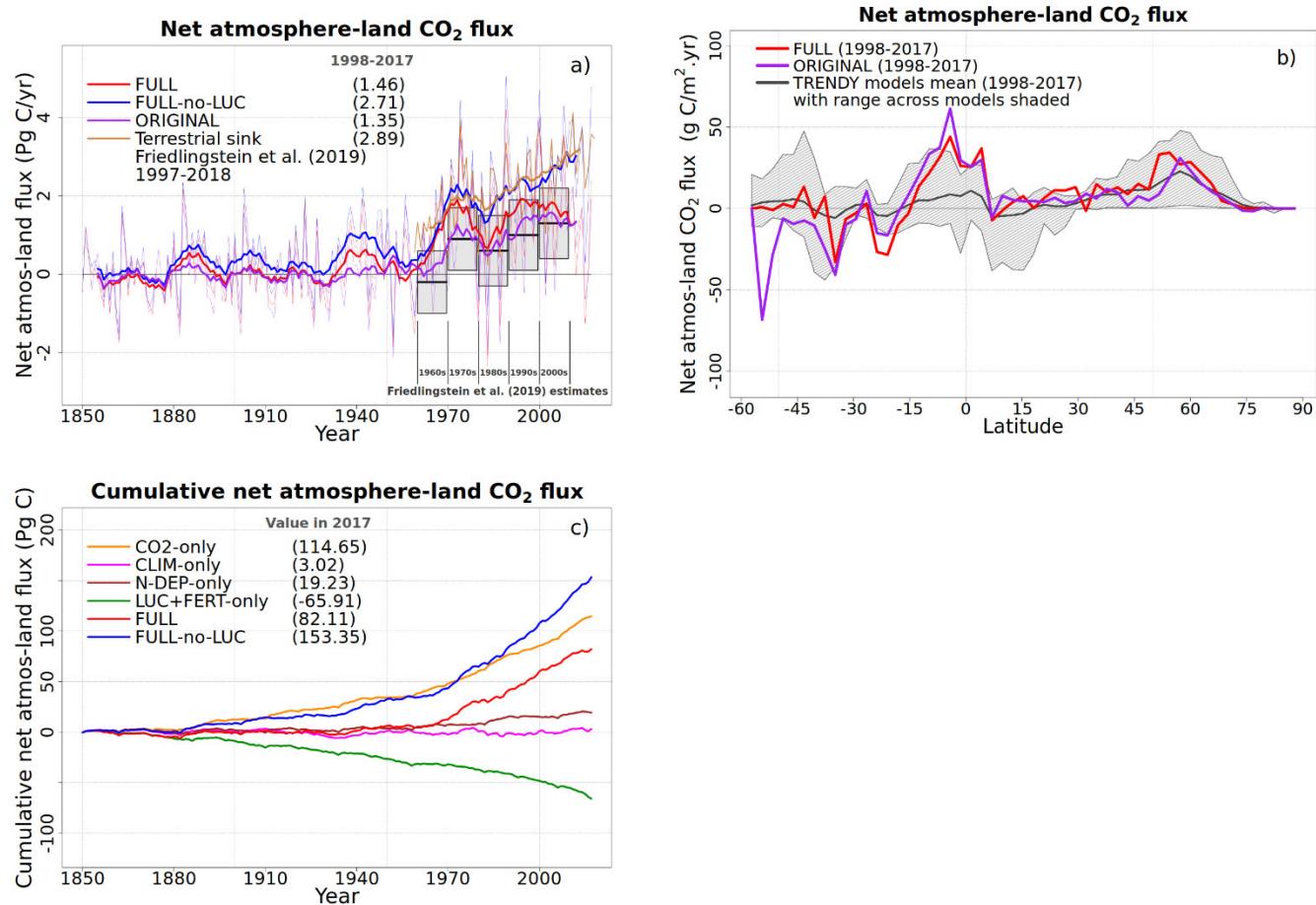
1449 Figure 11: Comparison of simulated net atmosphere-land CO_2 flux from various simulations.
1450 Panel (a) compares globally-summed values of net atmosphere-land CO_2 flux from FULL, FULL-
1451 no-LUC simulation, and ORIGINAL simulations with estimate of terrestrial sink (dark yellow line)
1452 and net atmosphere-land CO2 flux (grey bars) from Friedlingstein et al. (2019). The thin lines
1453 show the annual values and the thick lines their 10-year moving average. Panel (b) compares
1454 zonal distribution of net atmosphere-land CO_2 flux from FULL and ORIGINAL simulations with
1455 the range from TRENDY models that contributed to the Friedlingstein et al. (2019) study. Panel
1456 (c) shows cumulative values of net atmosphere-land CO_2 flux from the six primary simulations
1457 to investigate the contribution of each forcing to the cumulative land carbon sink over the
1458 historical period.

1459

References

1460 **References**

1461 Alexandrov, G. and Oikawa, T.: TsuBiMo: a biosphere model of the CO2-fertilization effect, Clim. Res.,
1462 19(3), 265–270, 2002.

1463 Aragão, L. E. O. C., Malhi, Y., Metcalfe, D. B., Silva-Espejo, J. E., Jiménez, E., Navarrete, D., Almeida, S.,
1464 Costa, A. C. L., Salinas, N., Phillips, O. L., Anderson, L. O., Alvarez, E., Baker, T. R., Goncalvez, P. H.,
1465 Huamán-Ovalle, J., Mamani-Solórzano, M., Meir, P., Monteagudo, A., Patiño, S., Peñuela, M. C., Prieto,
1466 A., Quesada, C. A., Rozas-Dávila, A., Rudas, A., Silva Jr., J. A. and Vásquez, R.: Above- and below-ground
1467 net primary productivity across ten Amazonian forests on contrasting soils, Biogeosciences, 6(12), 2759–
1468 2778, doi:10.5194/bg-6-2759-2009, 2009.

1469 Arneth, A., Harrison, S. P., Zaehle, S., Tsigaridis, K., Menon, S., Bartlein, P. J., Feichter, J., Korhola, A.,
1470 Kulmala, M., O'Donnell, D., Schurgers, G., Sorvari, S. and Vesala, T.: Terrestrial biogeochemical feedbacks
1471 in the climate system, Nat. Geosci., 3(8), 525–532, doi:10.1038/ngeo905, 2010.

1472 Arora, V. K.: Simulating energy and carbon fluxes over winter wheat using coupled land surface and
1473 terrestrial ecosystem models, Agric. For. Meteorol., 118(1), 21–47, doi:https://doi.org/10.1016/S0168-
1474 1923(03)00073-X, 2003.

1475 Arora, V. K. and Boer, G. J.: A Representation of Variable Root Distribution in Dynamic Vegetation
1476 Models, Earth Interact., 7(6), 1–19, doi:10.1175/1087-3562(2003)007<0001:AROVRD>2.0.CO;2, 2003.

1477 Arora, V. K. and Boer, G. J.: A parameterization of leaf phenology for the terrestrial ecosystem
1478 component of climate models, Glob. Change Biol., 11(1), 39–59, doi:10.1111/j.1365-2486.2004.00890.x,
1479 2005.

1480 Arora, V. K. and Boer, G. J.: Uncertainties in the 20th century carbon budget associated with land use
1481 change, Glob. Change Biol., 16(12), 3327–3348, doi:10.1111/j.1365-2486.2010.02202.x, 2010.

1482 Arora, V. K. and Melton, J. R.: Reduction in global area burned and wildfire emissions since 1930s
1483 enhances carbon uptake by land, Nat. Commun., 9(1), 1326, doi:10.1038/s41467-018-03838-0, 2018.

1484 Arora, V. K., Boer, G. J., Christian, J. R., Curry, C. L., Denman, K. L., Zahariev, K., Flato, G. M., Scinocca, J.
1485 F., Merryfield, W. J. and Lee, W. G.: The Effect of Terrestrial Photosynthesis Down Regulation on the
1486 Twentieth-Century Carbon Budget Simulated with the CCCma Earth System Model, J. Clim., 22(22),
1487 6066–6088, doi:10.1175/2009JCLI3037.1, 2009.

1488 Arora, V. K., Scinocca, J. F., Boer, G. J., Christian, J. R., Denman, K. L., Flato, G. M., Kharin, V. V., Lee, W. G.
1489 and Merryfield, W. J.: Carbon emission limits required to satisfy future representative concentration
1490 pathways of greenhouse gases, Geophys. Res. Lett., 38(5), doi:10.1029/2010GL046270, 2011.

1491 Arora, V. K., Boer, G. J., Friedlingstein, P., Eby, M., Jones, C. D., Christian, J. R., Bonan, G., Bopp, L.,
1492 Brovkin, V., Cadule, P., Hajima, T., Ilyina, T., Lindsay, K., Tjiputra, J. F. and Wu, T.: Carbon–Concentration
1493 and Carbon–Climate Feedbacks in CMIP5 Earth System Models, J. Clim., 26(15), 5289–5314,
1494 doi:10.1175/JCLI-D-12-00494.1, 2013.

1495 Arora, V. K., Katavouta, A., Williams, R. G., Jones, C. D., Brovkin, V., Friedlingstein, P., Schwinger, J., Bopp,
1496 L., Boucher, O., Cadule, P., Chamberlain, M. A., Christian, J. R., Delire, C., Fisher, R. A., Hajima, T., Ilyina,

1497   T., Joetzjer, E., Kawamiya, M., Koven, C. D., Krasting, J. P., Law, R. M., Lawrence, D. M., Lenton, A.,
1498   Lindsay, K., Pongratz, J., Raddatz, T., Séférian, R., Tachiiri, K., Tjiputra, J. F., Wiltshire, A., Wu, T. and
1499   Ziehn, T.: Carbon–concentration and carbon–climate feedbacks in CMIP6 models and their comparison
1500   to CMIP5 models, Biogeosciences, 17(16), 4173–4222, doi:10.5194/bg-17-4173-2020, 2020.

1501   Asaadi, A., Arora, V. K., Melton, J. R. and Bartlett, P.: An improved parameterization of leaf area index
1502   (LAI) seasonality in the Canadian Land Surface Scheme (CLASS) and Canadian Terrestrial Ecosystem
1503   Model (CTEM) modelling framework, Biogeosciences, 15(22), 6885–6907, doi:10.5194/bg-15-6885-2018,
1504   2018.

1505   Bauerle, W. L., Oren, R., Way, D. A., Qian, S. S., Stoy, P. C., Thornton, P. E., Bowden, J. D., Hoffman, F. M.
1506   and Reynolds, R. F.: Photoperiodic regulation of the seasonal pattern of photosynthetic capacity and the
1507   implications for carbon cycling, Proc. Natl. Acad. Sci., 109(22), 8612–8617,
1508   doi:10.1073/pnas.1119131109, 2012.

1509   Beer, C., Reichstein, M., Tomelleri, E., Ciais, P., Jung, M., Carvalhais, N., Rödenbeck, C., Arain, M. A.,
1510   Baldocchi, D., Bonan, G. B., Bondeau, A., Cescatti, A., Lasslop, G., Lindroth, A., Lomas, M., Luyssaert, S.,
1511   Margolis, H., Oleson, K. W., Roupsard, O., Veenendaal, E., Viovy, N., Williams, C., Woodward, F. I. and
1512   Papale, D.: Terrestrial Gross Carbon Dioxide Uptake: Global Distribution and Covariation with Climate,
1513   Science, 329(5993), 834–838, 2010.

1514   von Bloh, W., Schaphoff, S., Müller, C., Rolinski, S., Waha, K. and Zaehle, S.: Implementing the nitrogen
1515   cycle into the dynamic global vegetation, hydrology, and crop growth model LPJmL (version 5.0), Geosci.
1516   Model Dev., 11(7), 2789–2812, doi:10.5194/gmd-11-2789-2018, 2018.

1517   Bouwman, A. F., Beusen, A. H. W., Griffioen, J., Van Groenigen, J. W., Hefting, M. M., Oenema, O., Van
1518   Puijenbroek, P. J. T. M., Seitzinger, S., Slomp, C. P. and Stehfest, E.: Global trends and uncertainties in
1519   terrestrial denitrification and N2O emissions, Philos. Trans. R. Soc. B Biol. Sci., 368(1621), 20130112,
1520   doi:10.1098/rstb.2013.0112, 2013.

1521   Cao, M., Zhang, Q. and Shugart, H. H.: Dynamic responses of African ecosystem carbon cycling to climate
1522   change, Clim. Res., 17(2), 183–193, 2001.

1523   Clapp, R. B. and Hornberger, G. M.: Empirical equations for some soil hydraulic properties, Water
1524   Resour. Res., 14(4), 601–604, doi:10.1029/WR014i004p00601, 1978.

1525   Cleveland, C. C., Townsend, A. R., Schimel, D. S., Fisher, H., Howarth, R. W., Hedin, L. O., Perakis, S. S.,
1526   Latty, E. F., Von Fischer, J. C., Elseroad, A. and Wasson, M. F.: Global patterns of terrestrial biological
1527   nitrogen (N2) fixation in natural ecosystems, Glob. Biogeochem. Cycles, 13(2), 623–645,
1528   doi:10.1029/1999GB900014, 1999.

1529   Collatz, G., Ribas-Carbo, M. and Berry, J.: Coupled Photosynthesis-Stomatal Conductance Model for
1530   Leaves of C4 Plants, Funct. Plant Biol., 19(5), 519–538, 1992.

1531   Cotrufo, M. F., Ineson, P. and Scott, AndY.: Elevated CO2 reduces the nitrogen concentration of plant
1532   tissues, Glob. Change Biol., 4(1), 43–54, doi:10.1046/j.1365-2486.1998.00101.x, 1998.

1533   Croft, H., Chen, J. M., Luo, X., Bartlett, P., Chen, B. and Staebler, R. M.: Leaf chlorophyll content as a
1534   proxy for leaf photosynthetic capacity, Glob. Change Biol., 23(9), 3513–3524, doi:10.1111/gcb.13599,
1535   2017.

1536   Du, E., Terrer, C., Pellegrini, A. F. A., Ahlström, A., van Lissa, C. J., Zhao, X., Xia, N., Wu, X. and Jackson, R.
1537   B.: Global patterns of terrestrial nitrogen and phosphorus limitation, Nat. Geosci., 13(3), 221–226,
1538   doi:10.1038/s41561-019-0530-4, 2020.

1539   Evans, J. R.: Photosynthesis and nitrogen relationships in leaves of C3 plants, Oecologia, 78(1), 9–19,
1540   doi:10.1007/BF00377192, 1989.

1541   Eyring, V., Bony, S., Meehl, G. A., Senior, C. A., Stevens, B., Stouffer, R. J. and Taylor, K. E.: Overview of
1542   the Coupled Model Intercomparison Project Phase 6 (CMIP6) experimental design and organization,
1543   Geosci. Model Dev., 9(5), 1937–1958, doi:10.5194/gmd-9-1937-2016, 2016.

1544   Faria, T., Wilkins, D., Besford, R. T., Vaz, M., Pereira, J. S. and Chaves, M. M.: Growth at elevated CO2
1545   leads to down-regulation of photosynthesis and altered response to high temperature in Quercus suber
1546   L. seedlings, J. Exp. Bot., 47(11), 1755–1761, doi:10.1093/jxb/47.11.1755, 1996.

1547   Farquhar, G. D., von Caemmerer, S. and Berry, J. A.: A biochemical model of photosynthetic CO2
1548   assimilation in leaves of C3 species, Planta, 149(1), 78–90, doi:10.1007/BF00386231, 1980.

1549   Field, C. and Mooney, H.: The Photosynthesis-Nitrogen Relationship in Wild Plants, Biol. Int., 13, 25–56,
1550   1986.

1551   Fisher, J. B., Sitch, S., Malhi, Y., Fisher, R. A., Huntingford, C. and Tan, S.-Y.: Carbon cost of plant nitrogen
1552   acquisition: A mechanistic, globally applicable model of plant nitrogen uptake, retranslocation, and
1553   fixation: CARBON COST OF PLANT N ACQUISITION, Glob. Biogeochem. Cycles, 24(1), n/a-n/a,
1554   doi:10.1029/2009GB003621, 2010.

1555   Fowler, D., Coyle, M., Skiba, U., Sutton, M. A., Cape, J. N., Reis, S., Sheppard, L. J., Jenkins, A., Grizzetti,
1556   B., Galloway, J. N., Vitousek, P., Leach, A., Bouwman, A. F., Butterbach-Bahl, K., Dentener, F., Stevenson,
1557   D., Amann, M. and Voss, M.: The global nitrogen cycle in the twenty-first century, Philos. Trans. R. Soc. B
1558   Biol. Sci., 368(1621), 20130164, doi:10.1098/rstb.2013.0164, 2013.

1559   Friedlingstein, P., Cox, P., Betts, R., Bopp, L., von Bloh, W., Brovkin, V., Cadule, P., Doney, S., Eby, M.,
1560   Fung, I., Bala, G., John, J., Jones, C., Joos, F., Kato, T., Kawamiya, M., Knorr, W., Lindsay, K., Matthews, H.
1561   D., Raddatz, T., Rayner, P., Reick, C., Roeckner, E., Schnitzler, K.-G., Schnur, R., Strassmann, K., Weaver,
1562   A. J., Yoshikawa, C. and Zeng, N.: Climate–Carbon Cycle Feedback Analysis: Results from the C4MIP
1563   Model Intercomparison, J. Clim., 19(14), 3337–3353, doi:10.1175/JCLI3800.1, 2006.

1564   Friedlingstein, P., Jones, M. W., O'Sullivan, M., Andrew, R. M., Hauck, J., Peters, G. P., Peters, W.,
1565   Pongratz, J., Sitch, S., Le Quéré, C., Bakker, D. C. E., Canadell, J. G., Ciais, P., Jackson, R. B., Anthoni, P.,
1566   Barbero, L., Bastos, A., Bastrikov, V., Becker, M., Bopp, L., Buitenhuis, E., Chandra, N., Chevallier, F.,
1567   Chini, L. P., Currie, K. I., Feely, R. A., Gehlen, M., Gilfillan, D., Gkritzalis, T., Goll, D. S., Gruber, N.,
1568   Gutekunst, S., Harris, I., Haverd, V., Houghton, R. A., Hurtt, G., Ilyina, T., Jain, A. K., Joetzjer, E., Kaplan, J.
1569   O., Kato, E., Klein Goldewijk, K., Korsbakken, J. I., Landschützer, P., Lauvset, S. K., Lefèvre, N., Lenton, A.,
1570   Lienert, S., Lombardozzi, D., Marland, G., McGuire, P. C., Melton, J. R., Metzl, N., Munro, D. R., Nabel, J.
1571   E. M. S., Nakaoka, S.-I., Neill, C., Omar, A. M., Ono, T., Peregon, A., Pierrot, D., Poulter, B., Rehder, G.,

1572 Resplandy, L., Robertson, E., Rödenbeck, C., Séférian, R., Schwinger, J., Smith, N., Tans, P. P., Tian, H.,
1573 Tilbrook, B., Tubiello, F. N., van der Werf, G. R., Wiltshire, A. J. and Zaehle, S.: Global Carbon Budget
1574 2019, Earth Syst. Sci. Data, 11(4), 1783–1838, doi:10.5194/essd-11-1783-2019, 2019.

1575 Galloway, J. N., Dentener, F. J., Capone, D. G., Boyer, E. W., Howarth, R. W., Seitzinger, S. P., Asner, G. P.,
1576 Cleveland, C. C., Green, P. A., Holland, E. A., Karl, D. M., Michaels, A. F., Porter, J. H., Townsend, A. R. and
1577 Vöosmarty, C. J.: Nitrogen Cycles: Past, Present, and Future, Biogeochemistry, 70(2), 153–226,
1578 doi:10.1007/s10533-004-0370-0, 2004.

1579 Galloway, J. N., Leach, A. M., Bleeker, A. and Erisman, J. W.: A chronology of human understanding of
1580 the nitrogen cycle†, Philos. Trans. R. Soc. B Biol. Sci., 368(1621), 20130120,
1581 doi:10.1098/rstb.2013.0120, 2013.

1582 Garnier, E., Salager, J.-L., Laurent, G. and Sonie, L.: Relationships between photosynthesis, nitrogen and
1583 leaf structure in 14 grass species and their dependence on the basis of expression, New Phytol., 143(1),
1584 119–129, doi:10.1046/j.1469-8137.1999.00426.x, 1999.

1585 Gerber, S., Hedin, L. O., Oppenheimer, M., Pacala, S. W. and Shevliakova, E.: Nitrogen cycling and
1586 feedbacks in a global dynamic land model, Glob. Biogeochem. Cycles, 24(1),
1587 doi:10.1029/2008GB003336, 2010.

1588 Goll, D. S., Brovkin, V., Parida, B. R., Reick, C. H., Kattge, J., Reich, P. B., van Bodegom, P. M. and
1589 Niinemets, Ü.: Nutrient limitation reduces land carbon uptake in simulations with a model of combined
1590 carbon, nitrogen and phosphorus cycling, Biogeosciences, 9(9), 3547–3569, doi:10.5194/bg-9-3547-
1591 2012, 2012.

1592 Goyal, S. S. and Huffaker, R. C.: Nitrogen toxicity in plants, in Nitrogen in Crop Production, pp. 97–118,
1593 American Society of Agronomy, Madison, WI., 1984.

1594 Hungate, B. A., Dukes, J. S., Shaw, M. R., Luo, Y. and Field, C. B.: Nitrogen and Climate Change, Science,
1595 302(5650), 1512–1513, doi:10.1126/science.1091390, 2003.

1596 Hurtt, G. C., Chini, L., Sahajpal, R., Frolking, S., Bodirsky, B. L., Calvin, K., Doelman, J. C., Fisk, J., Fujimori,
1597 S., Klein Goldewijk, K., Hasegawa, T., Havlik, P., Heinimann, A., Humpenöder, F., Jungclaus, J., Kaplan, J.
1598 O., Kennedy, J., Krisztin, T., Lawrence, D., Lawrence, P., Ma, L., Mertz, O., Pongratz, J., Popp, A., Poulter,
1599 B., Riahi, K., Shevliakova, E., Stehfest, E., Thornton, P., Tubiello, F. N., van Vuuren, D. P. and Zhang, X.:
1600 Harmonization of global land use change and management for the period 850–2100 (LUH2) for CMIP6,
1601 Geosci. Model Dev., 13(11), 5425–5464, doi:10.5194/gmd-13-5425-2020, 2020.

1602 Jiang, M., Zaehle, S., De Kauwe, M. G., Walker, A. P., Caldararu, S., Ellsworth, D. S. and Medlyn, B. E.: The
1603 quasi-equilibrium framework revisited: analyzing long-term CO2 enrichment responses in plant–soil
1604 models, Geosci. Model Dev., 12(5), 2069–2089, doi:10.5194/gmd-12-2069-2019, 2019.

1605 Jones, A. G., Scullion, J., Ostle, N., Levy, P. E. and Gwynn-Jones, D.: Completing the FACE of elevated CO2
1606 research, Environ. Int., 73, 252–258, doi:https://doi.org/10.1016/j.envint.2014.07.021, 2014.

1607 Jones, C. D., Arora, V., Friedlingstein, P., Bopp, L., Brovkin, V., Dunne, J., Graven, H., Hoffman, F., Ilyina,
1608 T., John, J. G., Jung, M., Kawamiya, M., Koven, C., Pongratz, J., Raddatz, T., Randerson, J. T. and Zaehle,

1609   S.: C4MIP – The Coupled Climate–Carbon Cycle Model Intercomparison Project: experimental protocol
1610   for CMIP6, Geosci. Model Dev., 9(8), 2853–2880, doi:10.5194/gmd-9-2853-2016, 2016.

1611   Kattge, J., Knorr, W., Raddatz, T. and Wirth, C.: Quantifying photosynthetic capacity and its relationship
1612   to leaf nitrogen content for global-scale terrestrial biosphere models, Glob. Change Biol., 15(4), 976–
1613   991, doi:10.1111/j.1365-2486.2008.01744.x, 2009.

1614   Klein Goldewijk, K., Beusen, A., Doelman, J. and Stehfest, E.: Anthropogenic land use estimates for the
1615   Holocene – HYDE 3.2, Earth Syst. Sci. Data, 9(2), 927–953, doi:10.5194/essd-9-927-2017, 2017.

1616   Köchy, M., Hiederer, R. and Freibauer, A.: Global distribution of soil organic carbon – Part 1: Masses and
1617   frequency distributions of SOC stocks for the tropics, permafrost regions, wetlands, and the world, SOIL,
1618   1(1), 351–365, doi:10.5194/soil-1-351-2015, 2015.

1619   Kurz, W. A., Beukema, S. J. and Apps, M. J.: Estimation of root biomass and dynamics for the carbon
1620   budget model of the Canadian forest sector, Can. J. For. Res., 26(11), 1973–1979, doi:10.1139/x26-223,
1621   1996.

1622   Le Quéré, C., Andrew, R. M., Friedlingstein, P., Sitch, S., Hauck, J., Pongratz, J., Pickers, P. A., Korsbakken,
1623   J. I., Peters, G. P., Canadell, J. G., Arneth, A., Arora, V. K., Barbero, L., Bastos, A., Bopp, L., Chevallier, F.,
1624   Chini, L. P., Ciais, P., Doney, S. C., Gkritzalis, T., Goll, D. S., Harris, I., Haverd, V., Hoffman, F. M.,
1625   Hoppema, M., Houghton, R. A., Hurtt, G., Ilyina, T., Jain, A. K., Johannessen, T., Jones, C. D., Kato, E.,
1626   Keeling, R. F., Goldewijk, K. K., Landschützer, P., Lefèvre, N., Lienert, S., Liu, Z., Lombardozzi, D., Metzl,
1627   N., Munro, D. R., Nabel, J. E. M. S., Nakaoka, S., Neill, C., Olsen, A., Ono, T., Patra, P., Peregon, A., Peters,
1628   W., Peylin, P., Pfeil, B., Pierrot, D., Poulter, B., Rehder, G., Resplandy, L., Robertson, E., Rocher, M.,
1629   Rödenbeck, C., Schuster, U., Schwinger, J., Séférian, R., Skjelvan, I., Steinhoff, T., Sutton, A., Tans, P. P.,
1630   Tian, H., Tilbrook, B., Tubiello, F. N., van der Laan-Luijkx, I. T., van der Werf, G. R., Viovy, N., Walker, A.
1631   P., Wiltshire, A. J., Wright, R., Zaehle, S. and Zheng, B.: Global Carbon Budget 2018, Earth Syst. Sci. Data,
1632   10(4), 2141–2194, doi:10.5194/essd-10-2141-2018, 2018.

1633   Leith, H.: Modeling the primary productivity of the world, in Primary Productivity of the Biosphere (H.
1634   Leith and R. H. Whittaker, Eds.), pp. 237–263, Springer-Verlag, Berlin and New York., 1975.

1635   Li, D., Wang, X., Zheng, H., Zhou, K., Yao, X., Tian, Y., Zhu, Y., Cao, W. and Cheng, T.: Estimation of area-
1636   and mass-based leaf nitrogen contents of wheat and rice crops from water-removed spectra using
1637   continuous wavelet analysis, Plant Methods, 14(1), 76, doi:10.1186/s13007-018-0344-1, 2018.

1638   Li, H., Crabbe, M., Xu, F., Wang, W., Niu, R., Gao, X., Zhang, P. and Chen, H.: Seasonal Variations in
1639   Carbon, Nitrogen and Phosphorus Concentrations and C:N:P Stoichiometry in the Leaves of Differently
1640   Aged Larix principis-rupprechtii Mayr. Plantations, Forests, 8(10), 373, doi:10.3390/f8100373, 2017.

1641   Liang, J., Qi, X., Souza, L. and Luo, Y.: Processes regulating progressive nitrogen limitation under elevated
1642   carbon dioxide: a meta-analysis, Biogeosciences, 13(9), 2689–2699, doi:10.5194/bg-13-2689-2016, 2016.

1643   Lin, B.-L., Sakoda, A., Shibasaki, R., Goto, N. and Suzuki, M.: Modelling a global biogeochemical nitrogen
1644   cycle in terrestrial ecosystems, Ecol. Model., 135(1), 89–110, doi:https://doi.org/10.1016/S0304-
1645   3800(00)00372-0, 2000.

1646   Loomis, R. S.: On the utility of nitrogen in leaves, Proc. Natl. Acad. Sci., 94(25), 13378–13379,
1647   doi:10.1073/pnas.94.25.13378, 1997.

1648   Manzoni, S., Jackson, R. B., Trofymow, J. A. and Porporato, A.: The Global Stoichiometry of Litter
1649   Nitrogen Mineralization, Science, 321(5889), 684–686, doi:10.1126/science.1159792, 2008.

1650   McGuire, A. D., Melillo, J. M. and Joyce, L. A.: The role of nitrogen in the response of forests net primary
1651   production to elevated atmospheric carbon dioxide, Annu. Rev. Ecol. Syst., 26(1), 473–503,
1652   doi:10.1146/annurev.es.26.110195.002353, 1995.

1653   Melton, J. R. and Arora, V. K.: Competition between plant functional types in the Canadian Terrestrial
1654   Ecosystem Model (CTEM) v. 2.0, Geosci Model Dev, 9(1), 323–361, doi:10.5194/gmd-9-323-2016, 2016.

1655   Melton, J. R., Shrestha, R. K. and Arora, V. K.: The influence of soils on heterotrophic respiration exerts a
1656   strong control on net ecosystem productivity in seasonally dry Amazonian forests, Biogeosciences, 12(4),
1657   1151–1168, doi:10.5194/bg-12-1151-2015, 2015.

1658   Melton, J. R., Arora, V. K., Wisernig-Cojoc, E., Seiler, C., Fortier, M., Chan, E. and Teckentrup, L.: CLASSIC
1659   v1.0: the open-source community successor to the Canadian Land Surface Scheme (CLASS) and the
1660   Canadian Terrestrial Ecosystem Model (CTEM) – Part 1: Model framework and site-level performance,
1661   Geosci. Model Dev. Discuss., 2019, 1–40, doi:10.5194/gmd-2019-329, 2019.

1662   Meyerholt, J., Zaehle, S. and Smith, M. J.: Variability of projected terrestrial biosphere responses to
1663   elevated levels of atmospheric CO2 due to uncertainty in biological nitrogen fixation, Biogeosciences,
1664   13(5), 1491–1518, doi:10.5194/bg-13-1491-2016, 2016.

1665   Ochoa-Hueso, R., Maestre, F. T., Ríos, A. [de los, Valea, S., Theobald, M. R., Vivanco, M. G., Manrique, E.
1666   and Bowker, M. A.: Nitrogen deposition alters nitrogen cycling and reduces soil carbon content in low-
1667   productivity semiarid Mediterranean ecosystems, Environ. Pollut., 179, 185–193,
1668   doi:https://doi.org/10.1016/j.envpol.2013.03.060, 2013.

1669   O'Hara, G. W.: The Role of Nitrogen Fixation in Crop Production, J. Crop Prod., 1(2), 115–138,
1670   doi:10.1300/J144v01n02_05, 1998.

1671   Porporato, A., D'Odorico, P., Laio, F. and Rodriguez-Iturbe, I.: Hydrologic controls on soil carbon and
1672   nitrogen cycles. I. Modeling scheme, Adv. Water Resour., 26(1), 45–58,
1673   doi:https://doi.org/10.1016/S0309-1708(02)00094-5, 2003.

1674   Rastetter, E. B., Vitousek, P. M., Field, C., Shaver, G. R., Herbert, D. and gren, G. I.: Resource Optimization
1675   and Symbiotic Nitrogen Fixation, Ecosystems, 4(4), 369–388, doi:10.1007/s10021-001-0018-z, 2001.

1676   Reich, P. B., Hungate, B. A. and Luo, Y.: Carbon-Nitrogen Interactions in Terrestrial Ecosystems in
1677   Response to Rising Atmospheric Carbon Dioxide, Annu. Rev. Ecol. Evol. Syst., 37(1), 611–636,
1678   doi:10.1146/annurev.ecolsys.37.091305.110039, 2006a.

1679   Reich, P. B., Hobbie, S. E., Lee, T., Ellsworth, D. S., West, J. B., Tilman, D., Knops, J. M. H., Naeem, S. and
1680   Trost, J.: Nitrogen limitation constrains sustainability of ecosystem response to CO2, Nature, 440(7086),
1681   922–925, doi:10.1038/nature04486, 2006b.

1682   Riddick, S., Ward, D., Hess, P., Mahowald, N., Massad, R. and Holland, E.: Estimate of changes in
1683   agricultural terrestrial nitrogen pathways and ammonia emissions from 1850 to present in
1684   the\hack\newline Community Earth System Model, Biogeosciences, 13(11), 3397–3426, doi:10.5194/bg-
1685   13-3397-2016, 2016.

1686   Salvagiotti, F., Cassman, K. G., Specht, J. E., Walters, D. T., Weiss, A. and Dobermann, A.: Nitrogen
1687   uptake, fixation and response to fertilizer N in soybeans: A review, Field Crops Res., 108(1), 1–13,
1688   doi:https://doi.org/10.1016/j.fcr.2008.03.001, 2008.

1689   Sanz-Sáez, Á., Erice, G., Aranjuelo, I., Nogués, S., Irigoyen, J. J. and Sánchez-Díaz, M.: Photosynthetic
1690   down-regulation under elevated CO2 exposure can be prevented by nitrogen supply in nodulated alfalfa,
1691   J. Plant Physiol., 167(18), 1558–1565, doi:https://doi.org/10.1016/j.jplph.2010.06.015, 2010.

1692   Still, C. J., Berry, J. A., Collatz, G. J. and DeFries, R. S.: Global distribution of C3 and C4 vegetation: Carbon
1693   cycle implications, Glob. Biogeochem. Cycles, 17(1), 6–1, doi:10.1029/2001GB001807, 2003.

1694   Swart, N. C., Cole, J. N. S., Kharin, V. V., Lazare, M., Scinocca, J. F., Gillett, N. P., Anstey, J., Arora, V.,
1695   Christian, J. R., Hanna, S., Jiao, Y., Lee, W. G., Majaess, F., Saenko, O. A., Seiler, C., Seinen, C., Shao, A.,
1696   Sigmond, M., Solheim, L., von Salzen, K., Yang, D. and Winter, B.: The Canadian Earth System Model
1697   version 5 (CanESM5.0.3), Geosci. Model Dev., 12(11), 4823–4873, doi:10.5194/gmd-12-4823-2019,
1698   2019.

1699   Thom, A. S.: Momentum, mass and heat exchange of plant communities, in Vegetation and the
1700   atmosphere, Vol. 1, Principles, edited by Monteith, J. L., Academic Press, London., 1975.

1701   Thornton, P. E., Lamarque, J.-F., Rosenbloom, N. A. and Mahowald, N. M.: Influence of carbon-nitrogen
1702   cycle coupling on land model response to CO2 fertilization and climate variability, Glob. Biogeochem.
1703   Cycles, 21(4), doi:10.1029/2006GB002868, 2007.

1704   Tian, H., Yang, J., Lu, C., Xu, R., Canadell, J. G., Jackson, R. B., Arneth, A., Chang, J., Chen, G., Ciais, P.,
1705   Gerber, S., Ito, A., Huang, Y., Joos, F., Lienert, S., Messina, P., Olin, S., Pan, S., Peng, C., Saikawa, E.,
1706   Thompson, R. L., Vuichard, N., Winiwarter, W., Zaehle, S., Zhang, B., Zhang, K. and Zhu, Q.: The Global
1707   N2O Model Intercomparison Project, Bull. Am. Meteorol. Soc., 99(6), 1231–1251, doi:10.1175/BAMS-D-
1708   17-0212.1, 2018.

1709   Tipping, E., Somerville, C. J. and Luster, J.: The C:N:P:S stoichiometry of soil organic matter,
1710   Biogeochemistry, 130(1), 117–131, doi:10.1007/s10533-016-0247-z, 2016.

1711   Tomasek, A., Kozarek, J. L., Hondzo, M., Lurndahl, N., Sadowsky, M. J., Wang, P. and Staley, C.:
1712   Environmental drivers of denitrification rates and denitrifying gene abundances in channels and riparian
1713   areas, Water Resour. Res., 53(8), 6523–6538, doi:10.1002/2016WR019566, 2017.

1714   Verseghy, D. L.: Class—A Canadian land surface scheme for GCMS. I. Soil model, Int. J. Climatol., 11(2),
1715   111–133, doi:10.1002/joc.3370110202, 1991.

1716   Verseghy, D. L., McFarlane, N. A. and Lazare, M.: Class—A Canadian land surface scheme for GCMS, II.
1717   Vegetation model and coupled runs, Int. J. Climatol., 13(4), 347–370, doi:10.1002/joc.3370130402,
1718   1993.

1719 Vitousek, P. M.: Litterfall, Nutrient Cycling, and Nutrient Limitation in Tropical Forests, Ecology, 65(1),
1720 285–298, doi:10.2307/1939481, 1984.

1721 Vitousek, P. M.: Beyond Global Warming: Ecology and Global Change, Ecology, 75(7), 1861–1876,
1722 doi:10.2307/1941591, 1994.

1723 Vitousek, P. M. and Howarth, R. W.: Nitrogen limitation on land and in the sea: How can it occur?,
1724 Biogeochemistry, 13(2), 87–115, doi:10.1007/BF00002772, 1991.

1725 Vitousek, P. M., Porder, S., Houlton, B. Z. and Chadwick, O. A.: Terrestrial phosphorus limitation:
1726 mechanisms, implications, and nitrogen–phosphorus interactions, Ecol. Appl., 20(1), 5–15,
1727 doi:10.1890/08-0127.1, 2010.

1728 Vitousek, P. M., Menge, D. N. L., Reed, S. C. and Cleveland, C. C.: Biological nitrogen fixation: rates,
1729 patterns and ecological controls in terrestrial ecosystems, Philos. Trans. R. Soc. B Biol. Sci., 368(1621),
1730 20130119, doi:10.1098/rstb.2013.0119, 2013.

1731 Wang, J., Liu, X., Zhang, X., Li, L., Lam, S. K. and Pan, G.: Changes in plant C, N and P ratios under elevated
1732 [CO2] and canopy warming in a rice-winter wheat rotation system, Sci. Rep., 9(1), 5424,
1733 doi:10.1038/s41598-019-41944-1, 2019.

1734 Wania, R., Meissner, K. J., Eby, M., Arora, V. K., Ross, I. and Weaver, A. J.: Carbon-nitrogen feedbacks in
1735 the UVic ESCM, Geosci. Model Dev., 5(5), 1137–1160, doi:10.5194/gmd-5-1137-2012, 2012.

1736 Wei, X., Shao, M., Gale, W. and Li, L.: Global pattern of soil carbon losses due to the conversion of
1737 forests to agricultural land, Sci. Rep., 4, 4062, 2014.

1738 Wiltshire, A. J., Burke, E. J., Chadburn, S. E., Jones, C. D., Cox, P. M., Davies-Barnard, T., Friedlingstein, P.,
1739 Harper, A. B., Liddicoat, S., Sitch, S. A. and Zaehle, S.: JULES-CN: a coupled terrestrial Carbon-Nitrogen
1740 Scheme (JULES vn5.1), Geosci. Model Dev. Discuss., 2020, 1–40, doi:10.5194/gmd-2020-205, 2020.

1741 Xu-Ri and Prentice, I. C.: Terrestrial nitrogen cycle simulation with a dynamic global vegetation model,
1742 Glob. Change Biol., 14(8), 1745–1764, doi:10.1111/j.1365-2486.2008.01625.x, 2008.

1743 Zaehle, S.: Terrestrial nitrogen and carbon cycle interactions at the global scale, Philos. Trans. R. Soc. B
1744 Biol. Sci., 368(1621), 20130125, doi:10.1098/rstb.2013.0125, 2013.

1745 Zaehle, S. and Friend, A. D.: Carbon and nitrogen cycle dynamics in the O-CN land surface model: 1.
1746 Model description, site-scale evaluation, and sensitivity to parameter estimates: SITE-SCALE
1747 EVALUATION OF A C-N MODEL, Glob. Biogeochem. Cycles, 24(1), n/a-n/a, doi:10.1029/2009GB003521,
1748 2010.

1749 Zaehle, S., Friend, A. D., Friedlingstein, P., Dentener, F., Peylin, P. and Schulz, M.: Carbon and nitrogen
1750 cycle dynamics in the O-CN land surface model: 2. Role of the nitrogen cycle in the historical terrestrial
1751 carbon balance: NITROGEN EFFECTS ON GLOBAL C CYCLING, Glob. Biogeochem. Cycles, 24(1), n/a-n/a,
1752 doi:10.1029/2009GB003522, 2010.

1753 Zeng, H., Jia, G. and Epstein, H.: Recent changes in phenology over the northern high latitudes detected
1754 from multi-satellite data, Environ. Res. Lett., 6(4), 045508, 2011.

1755   Zhang, H., Goll, D. S., Manzoni, S., Ciais, P., Guenet, B. and Huang, Y.: Modeling the effects of litter
1756   stoichiometry and soil mineral N availability on soil organic matter formation using CENTURY-CUE (v1.0),
1757   Geosci. Model Dev., 11(12), 4779–4796, doi:10.5194/gmd-11-4779-2018, 2018.

1758   Zhao, X., Yang, Y., Shen, H., Geng, X. and Fang, J.: Global soil–climate–biome diagram: linking surface soil
1759   properties to climate and biota, Biogeosciences, 16(14), 2857–2871, doi:10.5194/bg-16-2857-2019,
1760   2019.

1761   Zhu, Z., Piao, S., Myneni, R. B., Huang, M., Zeng, Z., Canadell, J. G., Ciais, P., Sitch, S., Friedlingstein, P.,
1762   Arneth, A., Cao, C., Cheng, L., Kato, E., Koven, C., Li, Y., Lian, X., Liu, Y., Liu, R., Mao, J., Pan, Y., Peng, S.,
1763   Penuelas, J., Poulter, B., Pugh, T. A. M., Stocker, B. D., Viovy, N., Wang, X., Wang, Y., Xiao, Z., Yang, H.,
1764   Zaehle, S. and Zeng, N.: Greening of the Earth and its drivers, Nat. Clim Change, 6(8), 791–795, 2016.

1765   Zinke, P. J., Stangenberger, A. G., Post, W. M., Emanuel, W. R. and Olson, J. S.: Global Organic Soil
1766   Carbon and Nitrogen, Tech. Rep. ORNL/TM-8857, Oak Ridge National Laboratory, Oak Ridge, Tennessee,
1767   USA. [online] Available from: https://doi.org/10.3334/ORNLDAAC/221, 1998.

1768

1769

1770